Copyright
by
James Louis Hanssen
2004

The Dissertation Committee for James Louis Hanssen
certifies that this is the approved version of the following dissertation:

Controlling Atomic Motion: From Single Particle Classical Mechanics to Many Body Quantum Dynamics

Committee:

Mark Raizen, Supervisor

Manfred Fink

Roger Bengtson

Todd Ditmire

Irene Gamba

Controlling Atomic Motion: From Single Particle Classical Mechanics to Many Body Quantum Dynamics

by

James Louis Hanssen, B.A.

DISSERTATION

Presented to the Faculty of the Graduate School of

The University of Texas at Austin

in Partial Fulfillment

of the Requirements

for the Degree of

DOCTOR OF PHILOSOPHY

THE UNIVERSITY OF TEXAS AT AUSTIN

August 2004

Dedicated to my wife Laura and my parents. Without their help, none of this would have been possible.

Acknowledgments

First and foremost, I would like to thank my advisor, Mark Raizen. I was so fortunate that he took a chance on a kid with no experience with atomic physics experiments. He let me into the lab, showed me the exciting world of atomic physics, and taught me how to be an experimental physicist. He has always found the interesting topics to study and has creative ideas to tackle any problem that comes along. I am grateful for my time in the lab, and I look forward to the new results that will come from the experiments.

Next I would like to thank my co-workers: Todd Meyrath, Florian Schreck and Chih-Sung Chuu. For the past several years we have worked side by side on a variety of projects most of which are described in the last chapter. Todd is a very talented man who I have had the pleasure to know since beginning graduate school. He is the one who got me interested in cold atom experiments and recruited me for the lab. I am eternally grateful for that. I am also thankful for the many outings to the Salt Lick as well as the occasional movie quote. Florian is the new rising star in the ultra-cold atom physics world. He is a great experimentalist and has an unending drive. Hopefully he remembers to leave the lab and enjoy the mountains when he moves to Innsbruck. Chih-Sung is the not-so-new guy on the experiment. He may be quite, but he handles the experiment well. I know that the experiment

will be well taken care of after I leave.

Dan Steck and Windell Oskay deserve a special thanks for showing me how to work on an experiment. They were the senior students on the experiment when I joined the lab. Through their example I learned the ropes of working in the lab. There are many other people in the lab, past and present who have also helped me. It's been great fun working next to the guys on the "other" experiment: Martin Fisher, Braulio Guttierez, Kevin Henderson, and Hrishikesh Kelkar. They have been a great resource for information, man power, and the occasional mirror mount. Also, the friendly "Race to BEC" helped keep everyone motivated. Artem Dudarev and Chuanwei Zhang have provided theoretical help on many of our problems. They have also been great to hang out with at Todd's movie nights. All of these people have made working in the lab an enjoyable and rewarding experience.

In order to build and perform the experiments, a huge support staff is necessary. Allan Schroeder in the main machine shop made all my wildest dreams come true. If I could draw it, he made it happen, and he even put it on high priority. Jack Clifford in the student shop helped me with all the small projects and the quick fixes I needed on a regular basis. Both Lanny Sandefur and Ed Baez have been invaluable in the Cryo Shop. They have helped leak test all the vacuum pieces and helped create the coatings for the phase plates used in the experiments. Olga Vera, Rosie Tovar, and Elena Simmons are the administrative support staff of the CNLD. They made sure I was paid, the paperwork got done, and provided the occasional piece of candy. This support

staff made my life easier and the experiments possible.

There are many people who deserve thanks for helping with the writing and preparation of this dissertation. Laura Chap, Todd Meyrath, and Todd Tinsley read every chapter and found every mistake I made. An additional thanks is due to Todd Meyrath who helped with the writing of several sections describing the experimental systems he designed, built, and tested.

Last, but most definitely not least, I would like too thank the people to whom this dissertation is dedicated: my parents and my wife. My parents started me on my journey to becoming a physicist. The have always encouraged me and supported me in my scientific curiosity from taking apart my toys to pursuing my interest in physics in college and graduate school. My wife Laura has been by my side through the majority of my graduate school career. She helped me during the tough times and celebrated during the good. Without them, I would have never gotten as far as I did.

Controlling Atomic Motion: From Single Particle Classical Mechanics to Many Body Quantum Dynamics

Publication No. _____

James Louis Hanssen, Ph.D.
The University of Texas at Austin, 2004

Supervisor: Mark Raizen

This dissertation covers a series of experiments designed to control atomic motion. The experiments progress from being completely classical in nature to being described by many-body quantum mechanical models. The first experiment involves an experimental realization of a billiard using cold atoms and dipole potentials. The experiment was performed in a regime where the dynamics of the system were completely classical in nature. By adjustments of the shape of the billiard, it was demonstrated that the atomic motion within the billiard could be made stable and predictable or chaotic thereby allowing ergodic mixing. The subsequent experiment demonstrated the ability to control the center of mass motion of a collection of atoms without any *a priori* knowledge of the system. A minimally nondestructive method based on the quantum interaction of the atoms with a light field was used to measure the collective speed of the atoms. This information was utilized as a feedback signal to load the atoms into a co-moving trap that was subsequently brought

to rest in the laboratory frame. Finally, Bose-Einstein condensation in one and two dimensions has been performed. This will allow for the experimental realization of the quantum tweezer for atoms. In this system, a Bose-Einstein condensate is used as a reservoir to extract single atoms. Taking advantage of the coherence properties of the condensate as well as the mean field interaction of atoms within the tweezer, single atoms can be extracted with unit probability into the ground state of a dipole trap.

Table of Contents

Acknowledgments **v**

Abstract **viii**

List of Tables **xiii**

List of Figures **xiv**

Chapter 1. Introduction **1**
1.1 Overview of Research 1
1.2 Atom Optics 4

Chapter 2. Experimental Set Up **9**
2.1 Overview 9
2.2 Vacuum Chamber 10
2.2.1 Upper Vacuum Chamber 11
2.2.2 Middle Vacuum Chamber 16
2.2.3 Lower Vacuum Chamber 18
2.3 Lasers 20
2.3.1 Near Resonant Lasers 20
2.3.1.1 MOT Master Laser 22
2.3.1.2 Slave Lasers 33
2.3.1.3 Repump Master Laser 44
2.3.1.4 Laser Diode Control Electronics 47
2.3.2 Interaction Lasers 50
2.4 Magnetic Trap 51
2.4.1 Quadrupole Ioffe Configuration 51
2.4.2 Coil Structure and Construction 55
2.4.3 Current Driver Electronics 62

2.5 Control Electronics 66
2.6 The Sequence 69
2.6.1 Upper MOT 70
2.6.2 Transfer 73
2.6.3 Lower MOT 74
2.6.4 Optical Pumping and Transfer to the Magnetic Trap . . 77
2.6.5 Forced RF Evaporative Cooling 84
2.6.6 Detection and Condensation 90

Chapter 3. Atomic Billiards **99**
3.1 Overview 99
3.2 The Wedge Billiard 100
3.3 Experimental Techniques 106
3.4 Results 117
3.5 Conclusion 120

Chapter 4. Feedback Control **123**
4.1 Overview 123
4.2 Recoil Induced Resonances 125
4.2.1 Frequency Modulated RIR 130
4.3 Experimental Techniques 133
4.4 Results 141
4.5 Conclusions 145

Chapter 5. The Quantum Tweezer for Atoms **146**
5.1 Overview 146
5.2 Quantum Tweezer Theory 148
5.3 Experimental Techniques 157
5.3.1 Optical Traps 157
5.3.2 Magnetic Trap Decompression 166
5.3.3 BEC in an Optical Trap 169
5.3.4 High Frequency Optical Traps 171
5.3.5 Single Atom Detection 176
5.4 Future Outlook 184

Appendices **187**

Appendix A. Optical Dipole Traps **188**
A.1 Overview 188
A.2 The Dipole Potential 188
A.3 Gaussian Beams 192
A.3.1 Gaussian Traps 193
A.3.2 Sheet Traps 197
A.3.2.1 Red Sheets 197
A.3.2.2 Blue Sheets 197
A.3.3 Standing Wave Optical Traps 202
A.3.4 TEM01 Mode Traps 205
A.4 Spontaneous Emission 208

Appendix B. Bose-Einstein Condensates **210**
B.1 Overview 210
B.2 Three Dimensional Bose-Einstein Condensates 210
B.2.1 Thomas-Fermi Approximation 212
B.3 Two-Dimensional Condensates 215
B.4 One-Dimensional Condensates 217

Bibliography **220**

Vita **234**

List of Tables

1.1 Some useful atomic properties of cesium and rubidium. 8

2.1 Characteristics of the lasers diodes used in the experiment. . . 22

A.1 Typical values for a gaussian beam trap. 196
A.2 Typical values for a gravity-optical trap. 199
A.3 Typical compressed sheets trap values. 202
A.4 Typical values for a standing wave trap. 204
A.5 Typical values for a TEM_{01} mode trap. 208

List of Figures

2.1 The main optical table. 10
2.2 The shared optical table. 12
2.3 The upper chamber. 13
2.4 The differential pumping tube. 15
2.5 The UHV middle chamber. 17
2.6 The lower chamber. 19
2.7 The multitude of laser frequencies used in the experiment. . . 21
2.8 The master laser. 24
2.9 The MOT master laser locking setup. 27
2.10 The MOT saturated absorption spectroscopy dispersive signal. 30
2.11 MOT master laser distribution scheme. 32
2.12 Pictures of the slave lasers. 34
2.13 Beam distribution for the Upper MOT Horizontal slave laser. . 37
2.14 Picture of the homebuilt shutters used in the experiment. . . . 38
2.15 Beam distribution for the upper MOT diagonal beam slave laser. 41
2.16 Beam distribution for the lower MOT beam slave laser. 43
2.17 Repump saturated absorption profile. 45
2.18 The distribution network for the repump grating stabilized laser. 47
2.19 A simplified schematic for the laser diode current controller circuit. 48
2.20 The laser diode protection circuitry. 49
2.21 Top view of the QUIC trap. 52
2.22 Calculated field for our QUIC trap. 53
2.23 Vector field plot for the compressed QUIC trap. 54
2.24 The three primary coils of the QUIC trap. 57
2.25 A photograph showing the coils of the QUIC trap. 61
2.26 A schematic of the main power circuit that runs the magnetic trap coils. 63

2.27 A CCD image of the upper MOT. 71
2.28 The optics layout for the upper MOT. 72
2.29 The optical setup for the lower MOT. 75
2.30 An absorption image of the lower MOT. 76
2.31 An absorption image of the lower MOT after polarization gradient cooling. 77
2.32 Diagram of the optical pumping scheme. 79
2.33 Plots showing the currents in the coils as a function of time. . 82
2.34 Images of atoms within different configurations of the magnetic trap. 83
2.35 Plots showing the motion of the atomic cloud in the magnetic trap. 84
2.36 A schematic of how RF evaporation works. 86
2.37 Plots of the change in phase space density, ρ, as a function of the change in atom number and the change in temperature of the cloud during evaporation. 88
2.38 Images of the atomic cloud at various points during the evaporation sequence. 89
2.39 The bimodal distribution of a condensate. 96
2.40 A Bose-Einstein condensate of ^{87}Rb. 98

3.1 The gravitational wedge billiard. 101
3.2 Partitions of the wedge map. 104
3.3 A surface of section for a $2\theta = 53^{\circ}$ wedge. 105
3.4 Phase space portraits for different wedge angles. 106
3.5 Two AODs mounted orthogonally to each other. 109
3.6 Examples of different shapes achievable using the scanning AOD method. 110
3.7 Layout of the optical setup for the billiards experiment. 112
3.8 Two CCD images of a circular billiard. 114
3.9 The effect of soft walls on the wedge billiard. 116
3.10 A CCD image of the actual wedge used in experiment. 117
3.11 Survival probability as a function of the wedge angle. 118
3.12 A comparison of experimental and numerical results for the wedge billiard. 120

4.1 Stimulated Raman transitions between different motional states within a cloud of cold atoms. 126
4.2 Beam orientation for RIR. 127
4.3 A schematic of frequency modulated recoil induced resonances. 131
4.4 Experimental setup 135
4.5 A typical RIR signal. 138
4.6 Timing diagram of voltage signals involved in the feedback scheme. 140
4.7 Center of mass position of a cloud of atomic cesium falling with and without correction. 142
4.8 Temperature measurement of the cloud after stopping. 143

5.1 A diagram of how the tweezer works. 149
5.2 A continuation of the pictorial description of the quantum tweezer. 151
5.3 Energy diagrams for the tweezer system. 153
5.4 The probability of finding n atoms within the tweezer after extraction as a function of the extraction rate. 156
5.5 The layout of the optics on the Verdi table used to create the three separate repulsive traps. 159
5.6 Layout of the horizontal optical traps. 161
5.7 Layout of the vertical optical trap beams. 163
5.8 A CCD image of the tweezer beams. 165
5.9 Calculated field for the uncompressed QUIC trap. 167
5.10 An absorption image of the condensate created in the optical trap. 170
5.11 Intensity plots of the vertical sheet beam with and without a phase plate. 172
5.12 Simulations of the effect of the phase plate on a gaussian beam. 174
5.13 A plot of the half waist, $W/2$, of the the condensate as a function of time after release. 175
5.14 Single atom detection "super lens". 177
5.15 Photon count rates taken during the operation of a weak MOT. 181
5.16 A histogram of the counts shown in Fig. 5.15. 182
5.17 A plot of the reliability of the single atom detection system. . 183

A.1 The intensity distribution of a gaussian beam. 195

A.2 One dimensional potential profile for a gravity-optical sheet trap. 198
A.3 A two dimensional plot of the intensity distribution of two compressed sheets. 200
A.4 One dimensional intensity profile plots of two compressed sheets. 201
A.5 The intensity distribution of a standing wave trap. 203
A.6 The intensity distribution of a TEM_{01} mode beam. 207

Chapter 1

Introduction

1.1 Overview of Research

In the last decade, the contributions from ultra-cold atom research have received broad recognition. The 1997 Nobel Prize in physics was awarded to Steven Chu, Claude Cohen-Tannoudji, and William D. Phillips "for development of methods to cool and trap atoms with laser light"[1]. The award was more recently given in 2001 to Eric A. Cornell, Wolfgang Ketterle, Carl E. Wieman "for the achievement of Bose-Einstein condensation in dilute gases of alkali atoms, and for early fundamental studies of the properties of the condensates"[2]. The first major advance came in 1987 the first demonstration of a magneto-optical trap (MOT) by Steve Chu and co-workers[3]. At that point, atoms could be trapped and cooled down to extremes never before possible. This allowed for the study of a variety of processes: cold collisions[4], atom lithography[5], atom interferometry[6], atomic clocks[7, 8], Bose-Einstein condensation[9–11], and quantum chaos[12, 13]. The last two processes are especially relevant to the research performed in our laboratory. This dissertation covers several experiments that contributed to this growing field.

Atomic Billiards Some of the first quantum chaos experiments took place within the context of optical lattices. These experiments were one-dimensional, time-dependent quantum systems where the dynamics are chaotic in the classical limit. As those experiments come to a close, a new type of trap is needed in which to study atomic motion. This led to the development of the atomic billiard trap. Described in Chapter 3, these atomic billiards provide new opportunities to study quantum chaos and quantum-classical correspondence. These traps are very versatile; not only are they able to have arbitrary shapes, but those shapes can vary in time. This allows for studies of quantum chaos in static two-dimensional systems as well as time dependent two-dimensional systems.

Feedback Control Since the first MOT was built to trap and cool atoms, scientists have dreamed of laser cooling a wide range of atoms and molecules. Presently, laser cooling is limited to a handful of elements, largely the alkali metals. These atoms possess a closed atomic cycling transition. The cycling transition allows for energy dissipation through spontaneous emission which can be exploited to cool the atoms.

In 1998, Mark Raizen et. al. proposed an idea that would allow other elements and molecules to be "laser cooled"[14]. This idea is an extension of the stochastic cooling used to increase the flux of anti-proton beams, for which won Simon van der Meer the Nobel prize in 1984[15]. Through a series of measurements and feedback, the momentum fluctuations in an ensemble

of particles can be damped out, thereby cooling the sample. Chapter 4 gives details about the proof-of-principle demonstration we performed of the idea using cesium atoms. The measurement and feedback technique, which relied on far off resonant lasers, does not depend on an atomic transition. Therefore, this could lead to the future "laser cooling" of non-alkali atoms or molecules. This would lead to a host of interesting physics as well as new technologies.

The Quantum Tweezer Since the dawn of quantum mechanics, people have been trying to find new ways to see and exploit quantum effects. The most recent and interesting route has been quantum state engineering. Engineering a well-defined quantum state may lead to exotic applications such as quantum teleportation, quantum cryptography, and quantum computation[16].

Many different avenues are being pursued to achieve this. In atom optics, various research groups are striving to isolate single atoms and force them into a specific quantum state. In 2002, an idea was put forth to use a condensate as an atom reservoir and to extract a single atom in the ground state of a dipole trap; thus producing an individual atom in a well-defined quantum state [17]. Progress towards the experimental realization of this idea is presented in Chapter 5. Along the way, a variety of new techniques and novel optical dipole traps were developed.

1.2 Atom Optics

This section describes some of the basic atomic properties of the elements used for the research described in this dissertation. Some of the basic terminology used in the field will be presented. Also provided is a brief discussion of the behavior of neutral atoms in the presence of magnetic fields and electric fields.

For a long time, atoms were perceived to behave as particles. With the advent of quantum mechanics, the consensus changed with the realization that all objects behave as both waves and particles. The study of these wave-like properties of atoms make up the field of atom optics. Atom optics can be seen as the matter analog of traditional light optics. Electric fields and magnetic fields are used to reflect and manipulate atoms in much the same way mirrors and lenses reflect and focus the electric and magnetic fields of light.

Atoms are made of protons, neutrons, and electrons, all of which have a spin. The nucleons together give the atom its nuclear spin, I. In the case of rubidium $I = 3/2$ and $I = 5/2$, for the isotopes ^{87}Rb and ^{85}Rb, respectively.

Before the total spin of the atom, F, can be calculated, the spin of the electron has to be considered. The total angular momentum of the electron

$$\mathbf{J} = \mathbf{S} + \mathbf{L} \tag{1.1}$$

is a combination of the spin of the electron, $\mathbf{S}$, and the orbital angular momentum of the electron, $\mathbf{L}$. In the ground state, $L = 0$, therefore $J = \pm 1/2$.

The total atomic angular momentum

$$\mathbf{F} = \mathbf{I} + \mathbf{J} \tag{1.2}$$

is the sum of the nuclear spin, $\mathbf{I}$, and the total electronic angular momentum, $\mathbf{J}$. This coupling gives rise to the hyperfine structure of the atom. Since $J = \pm 1/2$ and $I = 3/2$, the two ground states of Rb^{87} are $F = 1$ and $F = 2$ and are separated by roughly 6.83GHz.

There are $2F+1$ degenerate magnetic sublevels for each hyperfine level. When placed within a magnetic field, $\hat{\mathbf{B}}$, this degeneracy is lifted. The Hamiltonian describing the interaction of the atoms with the magnetic field is [18]

$$H_B = \frac{\mu_B}{\hbar}(g_S\mathbf{S} + g_L\mathbf{L} + g_I\mathbf{I}) \cdot \mathbf{B}\,, \tag{1.3}$$

where μ_B is the Bohr magneton and g_S, g_L, and g_I are the appropriate nuclear "g-factors". In the case where the magnetic field is weak and the energy shift is small compared to the hyperfine splitting, this reduces to

$$H_B = \mu_B g_F F_z B_z\,, \tag{1.4}$$

where we have taken the magnetic field to be along the z direction. This leads to an energy shift of

$$\Delta E = g_F m_F \mu_B B_z\,, \tag{1.5}$$

where g_F is the Landé g-factor and $m_F \in (-2F, \ldots, 2F)$ is the quantum number for the projection of the magnetic moment along the direction of the magnetic field. This energy shift is known as the Zeeman effect.

In addition to being subject to the effects of magnetic fields, neutral atoms are also sensitive to electric fields, in particular the oscillating electric field present in a laser beam. While atoms are sensitive to light fields, their interaction with them is more involved. The atom interacts with the light field by scattering photons. The scattering is either coherent or incoherent, resulting in two different effects.

The coherent interaction is also known as stimulated emission. The atom scatters the photon by absorbing it. The presence of the light field induces the atom to emit the photon in phase with the field, creating the dipole force. A more intuitive semiclassical picture of this is given in Appendix A.

Spontaneous emission is the incoherent process. Again, the atom absorbs a photon, but this time, the atom emits the photon randomly without any reference to the light field. This leads to a dissipative force acting on the atom, which can be used to cool an ensemble of similar atoms. A more detailed description of spontaneous emission can be found in Appendix A.

The relative strengths of the two forces is important to note. The conservative dipole force is inversely proportional to the detuning, Δ, from atomic resonance and directly proportional to the gradient of the intensity, I,

$$F_{dip} \propto \frac{\nabla I}{\Delta}\,, \tag{1.6}$$

while the force due to spontaneous emission is inversely proportional to the detuning squared

$$F_{scat} \propto \frac{I}{\Delta^2}\,. \tag{1.7}$$

A comparison of these two relationships shows that with enough laser power and far enough detuning from resonance, the dipole force can be made quite substantial while rendering the spontaneous emission force negligible. This situation yields a conservative optical trap.

A variety of terms have evolved to describe the behavior of ultra-cold neutral atoms. These terms provide units which are better adapted to describing the atomic system than standard units. When an atom absorbs a photon, it receives a momentum kick. The resulting change in velocity is referred to as the recoil velocity

$$v_{rec} = \frac{\hbar k_A}{m}\,, \tag{1.8}$$

where k_A is the wave number for resonant light and is an appropriate unit of speed for cold atoms. Similarly, the recoil energy

$$E_{rec} = \frac{\hbar^2 k_A^2}{2m} = \hbar\omega_{recoil} \tag{1.9}$$

which is just the energy of an atom moving at the recoil velocity, is an appropriate energy scale for cold atoms. Here, the recoil frequency, ω_{rec}, is also defined. Converting E_{rec} into a temperature provides the recoil temperature

$$T_{rec} = \frac{\hbar^2 k_A^2}{m k_B}\,. \tag{1.10}$$

The experiments described within this dissertation cover a wide period of time over which the experimental apparatus evolved dramatically. During this evolution, the alkali atom used for laser cooling and trapping changed from cesium 133 to rubidium 87. Since both elements will be discussed throughout

this thesis, it is useful to have some of the basic atomic properties of both elements readily available. Table 1.1 lists some of the more useful atomic constants for cesium and rubidium.

Atomic Properties of ^{133}Cs and ^{87}Rb			
parameter	symbol	cesium	rubidium
mass	m	133amu	87amu
nuclear spin	I	7/2	3/2
D2 transition wavelength	λ	852.35nm	780.25nm
lifetime	τ	30.5ns	26.2ns
decay rate	Γ	$2\pi \cdot 5.22$MHz	$2\pi \cdot 6.07$MHz
recoil velocity	v_{rec}	3mm/s	6mm/s
recoil energy	$\hbar\omega_{rec}$	$\hbar \cdot 2\pi \cdot 2.07$kHz	$\hbar \cdot 2\pi \cdot 3.77$kHz
recoil temperature	T_{rec}	198nK	362nK
saturation intensity	I_{sat}	2.70mW/cm^2	3.58mW/cm^2
hyperfine splitting	ν_{hf}	9.28 GHz	6.83GHz

Table 1.1: Some useful atomic properties of cesium and rubidium. These values were provided by Daniel Steck[19, 20].

Chapter 2

Experimental Set Up

The experiments described in this dissertation were conducted over a period of five years. During that time, the experimental apparatus evolved from a machine to trap and cool cesium atoms in a MOT to a rubidium Bose-Einstein condensation machine. Details on the cesium experiment can be found elsewhere [18, 21, 22] and only the rubidium experiment will be discussed here.

2.1 Overview

The system used to create the rubidium condensate is quite extensive. The bulk of the optical equipment used in the experiment resides on two optical tables. One 12'x5' optical table holding literally thousands of optical components, six lasers, a variety of electronic and mechanical hardware, and the vacuum chamber is dedicated solely to the rubidium experiment and is shown in Fig. 2.1. A second 8'x4' optical table, shown in Fig. 2.2, is shared between the rubidium and sodium experiments [23]. It holds the shared laser and the necessary optics and modulators to shape the beam and send it to the main optical table.

Despite the complexity of the experiment, at the heart of the apparatus

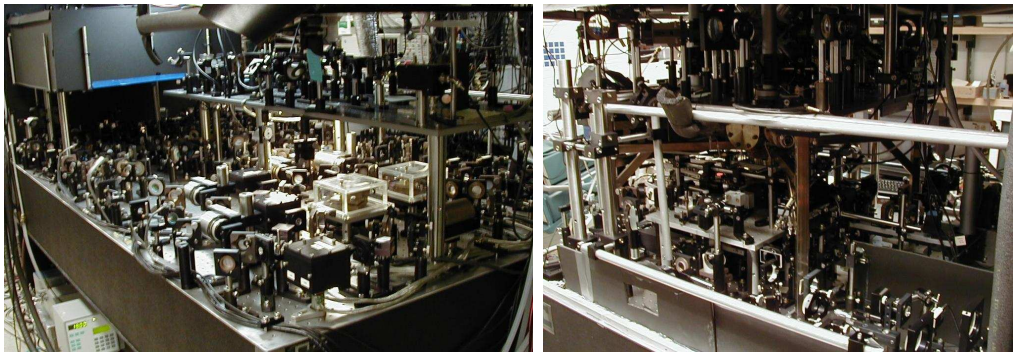

Figure 2.1: The main optical table. The table is divided into two section. The image on the left shows the section of table devoted to the lasers. The image on the right shows the section for the vacuum chamber.

there are four main systems: the vacuum chamber, the lasers, the magnetic trap, and the computer control system. Without these ingredients, the experiment will never operate. All the additional components are used to improve efficiency and reproducibility. These main systems will be discussed first.

2.2 Vacuum Chamber

The experimental system was designed to be a double MOT setup similar to that of Ref. [24]. In order to accomplish this, the vacuum chamber has three distinct parts: an upper chamber where a vapor cell MOT resides, a lower chamber where a charged MOT lives in an ultra-high vacuum environment, and a middle section connecting the two that provides the necessary pumping to achieve the ultra-high vacuum pressures needed in the lower chamber.

2.2.1 Upper Vacuum Chamber

The upper chamber (Fig. 2.3) was constructed from a modified six way, 304 stainless steel cross with a 1.5" tube diameter. Each of the tubes has a fixed 2.75" flange welded to the end. This chamber was originally used in a previous sodium experiment; a more detailed description of the chamber can be found in Ref. [25]. Attached to each flange is an uncoated 2.75" zero length window obtained from Larson Electronic Glass. It should be noted that zero length windows may not be the ideal choice for vacuum chambers with moderately high pressures ($\approx 10^{-7}$ Torr) of alkali metal vapor. On several occasions, it has been observed that the glass-to-metal seal degrades leading to a catastrophic failure of the window. The glass-to-metal seal is made out of Kovar which is highly reactive. Possibly, the alkali metal vapor reacts strongly with the Kovar in the seal, and at the pressures used in the upper chamber, this leads to failures. Future versions of the upper chamber should avoid the use of zero length windows. Possible solutions include using non-zero length windows made from stainless steel or moving over to an upper chamber made completely from glass.

The cross had five tubes welded to it to provide additional access. Two of the tubes provide additional optical access. These tubes are 0.75" in diameter and end in 1.33" flanges with 1.33" uncoated zero length windows attached. One serves as a survey port to observe the state of the upper MOT. The other serves as an entrance port for the push beam which will be discussed later.

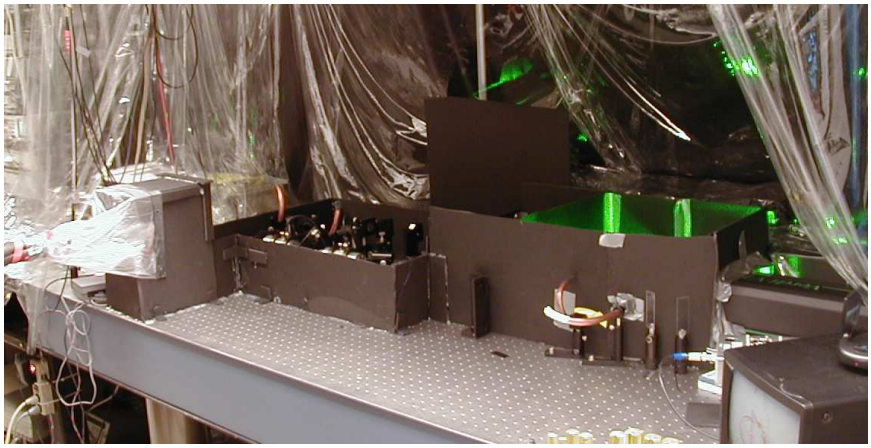

Figure 2.2: The shared optical table. It holds the Verdi laser as well as some of the beam control optics for that laser. A fortress of black foam board surrounds some of the optics to protect the beam from air currents.

Of the three remaining tubes, one is used for the shutter. This tube is 0.5" in diameter and has a 0.75" steel bellows welded to it. At the end of the tube is a 2.75" rotatable flange. The entire length of this tube makes a 20° angle to the horizontal 1.5" tube above it. An all-metal linear actuator, MDC model HTBLM-275-1, with a travel of one inch is attached to the end of this tube. At the end of the actuator, a small metal flag has been welded on to act as a shutter to separate the UHV region from the HV region. A stepper motor can be attached through a universal joint to drive the shutter so that the during the transfer of atoms, a free path exists between the two vacuum regions, and at other times the path is closed. This option has not been implemented as it has subsequently appeared to be unnecessary. One of the main features of the experimental apparatus is the ability to detect single

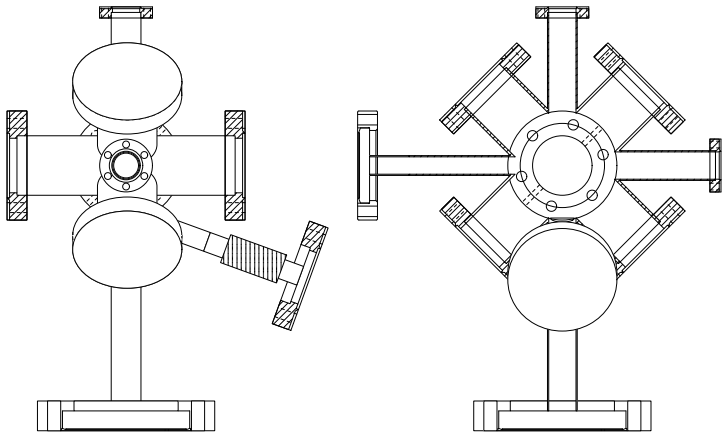

Figure 2.3: The upper chamber. The image on the right is a 90 degree rotation of the one on the left.

atoms (see Chap. 5) and it was feared that without the shutter, the upper chamber would act as a source of atoms and limit the capabilities of the single atom detection system. Tests have shown that is not the case.

A 0.75" steel tube is welded to the bottom of the chamber providing a connection port to the rest of the vacuum system. On the end of this tube is a rotatable 4.5" flange.

The last additional tube is used to house an exchangeable rubidium supply. The 0.5" steel tube ends with a 2.75" steel flange connected to a 1.5" all-metal valve. Connected to this valve is a 1.33" steel tee connected to a 0.75" all-metal valve and a pinch-off tube containing a one third gram ampoule of rubidium. The two valves act as an interchangeable rubidium reservoir. The 0.75" valve seals the system from the outside world and the 1.5" valve, which

is open when the system is in use, can seal the reservoir tube from the vacuum system. If the rubidium needs to be changed, the large valve is sealed and the reservoir removed. The ampoule is replaced, the reservoir pumped down, the ampoule cracked, and finally, rubidium reintroduced to the entire vacuum system.

Attached to the chamber, along one of the 1.5" horizontal arms, is a Bayard-Alpert type ion gauge from HPS, along with a 20 $\frac{l}{s}$ ion pump from Varian, Inc., model VacIon Plus 20. The ion gauge exists as a check for the vapor pressure of rubidium in the upper chamber. Should the pressure be too large, the pump serves as a means to reduce the pressure. A valve separates the pump from the chamber, effectively making the pumping speed variable from 20 $\frac{l}{s}$ to 0 $\frac{l}{s}$. In practice, neither the ion gauge nor the pump is used often. The ion gauge was never completely degassed and, in an effort to not pollute the system, has rarely been used. High vapor pressures are ideal for quickly loading a large number of atoms into the upper MOT. Therefore, the pump is rarely used.

In order for there to be effective loading of the upper MOT while at the same time ultra high vacuum (UHV) in the region where the condensate resides to provide long lifetimes, an extreme difference in pressure between the two regions must exist. For quick loading of the upper MOT, that region needs to have a pressure, dominated by rubidium vapor, on the order of 10^{-7}Torr $\sim$ 10^{-8} Torr. On the other hand, for the long magnetic trap lifetimes of several minutes needed for evaporative cooling, pressures on the order of 10^{-11} Torr

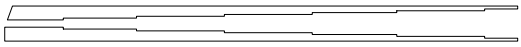

Figure 2.4: The differential pumping tube.

or better are required. The three orders of magnitude difference in pressure are provided by the differential pumping tube that connects the upper MOT chamber to the middle UHV chamber.

The differential pumping tube (see Fig. 2.4) consists of an eight and three quarter inch long 304 stainless steel tube with an outer diameter of approximately half an inch. The inner diameter of the tube increases in successive steps from an eighth of an inch at the top to one half of an inch at the bottom (by that point the outer diameter has increased to 0.600 inches). At the top of the tube, a small 20^o wedge has been lopped off to allow a shutter blade to slide over the top. The tube is welded into a double-sided 4.5" flange that is used to connect the upper and lower chambers.

The stepping of the inner diameter was chosen to have an angle of $\approx 2^o$. This maximizes the solid capture angle defined by the position of the upper MOT, lower MOT, and the physical dimensions of the lower cell. In addition, the stepping allowed for a lower conductance which increased to pressure difference between the two chamber regions. The tube has a calculated conductance of $\approx 0.091 \frac{l}{s}$ for air at room temperature and more importantly $\approx 0.051 \frac{l}{s}$ for rubidium at room temperature [26]. This leads to approximately three orders of magnitude difference between the pressure of the upper and

lower chambers.

2.2.2 Middle Vacuum Chamber

The middle chamber, located directly below the upper chamber, serves as a docking port for a series of pumps and vacuum measurement devices. The chamber is a modified six-way cross with 4.5" flanges. Four 1.5" tubes with nonrotatable 2.75" flanges are welded between the 4.5" ports in one plane around the middle chamber. As this chamber was also previously used in an experiment, a more detailed description can be found elsewhere [18, 21, 22].

Attached to the chamber are two pumps. One is a 75 $\frac{l}{s}$ ion pump. It was originally purchased from Varian, Inc. and later refurbished by Duniway Stockroom. The other is a titanium sublimation pump (TSP). This was purchased from Duniway Stockroom, model number TSP-275-003. The pumping speed of the TSP depends on a variety of factors including the cleanliness of the layer of deposited titanium, the area of the deposited titanium, and the background pressure in the chamber. The filament needs to be run from time to time in order to keep the titanium surface clean so that it may pump. Under normal operating parameters, the pump is specified to have a pumping speed of $\approx 300\,\frac{l}{s}$.

In addition to the pumps on the middle chamber, situated within one of the 2.75" ports, there is a Bayard-Alpert type ion gauge from HPS. This gauge is used for measuring the pressure of the UHV region. It can not be left on during the experiment, therefore, it is simply a diagnostic tool used

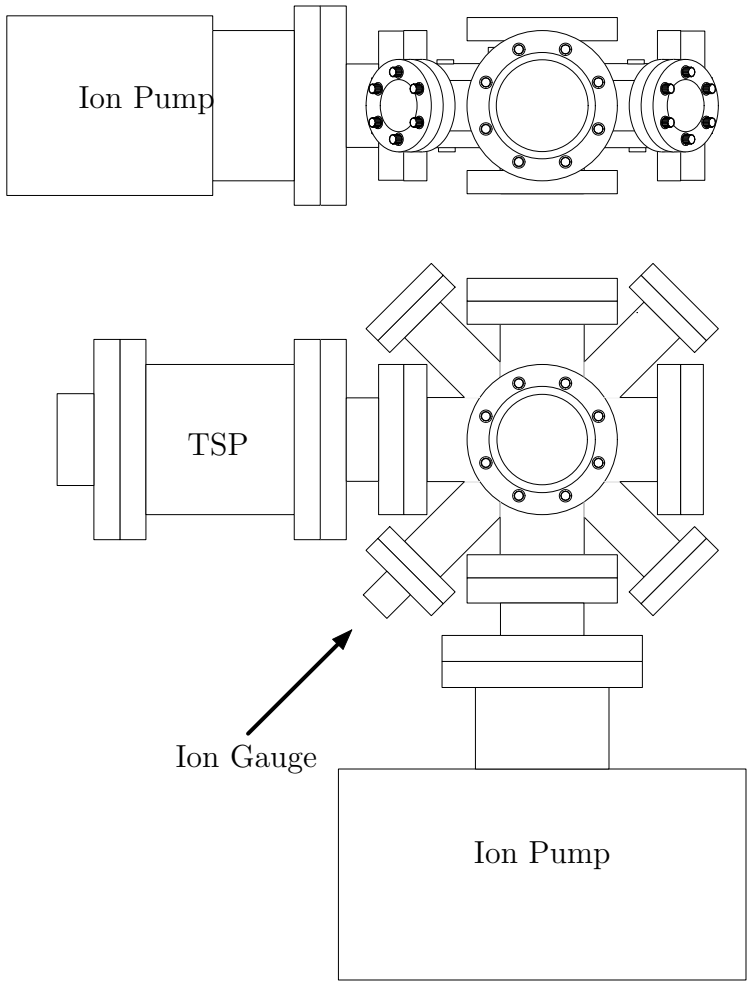

Figure 2.5: The UHV middle chamber. Attached to the main vacuum chamber are two pumps and an ion gauge.

occasionally. The usefulness of the gauge is limited in that it appears that the gauge has bottomed out at a reading of 5×10^{-10} Torr which is significantly higher than our goal of 10^{-11} Torr. Ultimately, the only true way to determine whether the vacuum is good enough is through lifetime measurements of atoms within the magnetic trap. That said, the gauge still serves the purpose of reassuring us that vacuum has not been lost.

2.2.3 Lower Vacuum Chamber

The lower chamber was designed to be an ultra high vacuum chamber with as much optical access as possible. This was done using an all glass cell attached to a large steel chamber that acts as a docking station for several pumps and vacuum measurement devices. The glass cell gives great optical access, while the steel chamber supports enough pumping power to provide the appropriate UHV environment.

The cell is based off a design by the group of Ted Hänsch [27]. The glass cell was purchased from Hellma Cells, Incorporated. It was made out of Spectrosil, which is an optical quality, synthetic fused silica. The cell is rectangular in shape with outer dimensions of 30 mm by 30 mm by 115 mm. The walls of the cell are 5 mm thick. It was formed by optically contacting the individual walls together then raising the temperature of the cell until the pieces fuse together eliminating the need for any cement material. At the top of the cell, a large Spectrosil flange was fused on. The flange measures 75 mm in diameter by 17 mm thick with a 20 mm hole in the center to allow access

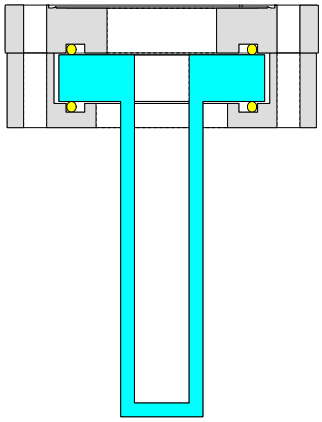

Figure 2.6: The lower chamber. The glass cell is where the experiments take place. The metal adaptor and the gold colored helicoflex seals connect the glass cell to the middle chamber.

to the cell. This flanged provided the means to attach the cell to the steel chamber. In our case, the flange is smooth. Others have used a frosted flange along with Vac-Seal, a UHV compatible sealant [28]. While this approach was not taken, acceptable results were achieved.

The glass cell is attached, via Helicoflex seals, to the steel middle chamber. The Helicoflex seals, Garlock-Helicoflex part number H-307330 REV NC, are all metal seals with a design such that they can form glass-to-metal seals. They consist of a helical spring enveloped in two metal linings. In addition, there are two delta shaped ridges along the top and bottom of the seal. As the seal is compressed, the ridges bite into the compressing surfaces, forming the seal. Unlike a sealing torque, which is given for copper gaskets between flanges of in an all metal valve, a sealing compression is given for the Helicoflex seals.

Therefore, the connecting flange that brought the glass cell, the seals, and the metal chamber together were specially designed to provided the appropriate compression.

2.3 Lasers

There are seven main lasers producing nearly as many different frequencies used to make the experiment run (see Fig. 2.7). These lasers can be grouped into two different categories. The first consists of lasers that produce near resonant light used for trapping and cooling of the atoms as well as optical pumping and imaging. The second group is made up of far off resonant lasers, either blue or red of resonance, that are used solely for trapping.

2.3.1 Near Resonant Lasers

A correctly operating magneto-optic trap relies on near resonant lasers. In fact, two distinct frequencies are necessary. As will be discussed later in this chapter, light that is tuned red of the $F = 2 \rightarrow F' = 3$ cycling transition is needed. This light, in conjunction with an appropriate magnetic field, is used to trap and cool atoms from a background vapor. In addition to this light, a second frequency called the repump light is needed. Due to the extensive level structure of rubidium, the cycling transition is not a closed transition and occasionally atoms will be excited to the wrong state, decay to the $F = 1$ ground state, and be removed from the MOT. To circumvent this, the repump light is on the $F = 1 \rightarrow F' = 2$ transition to put the stray atoms back into

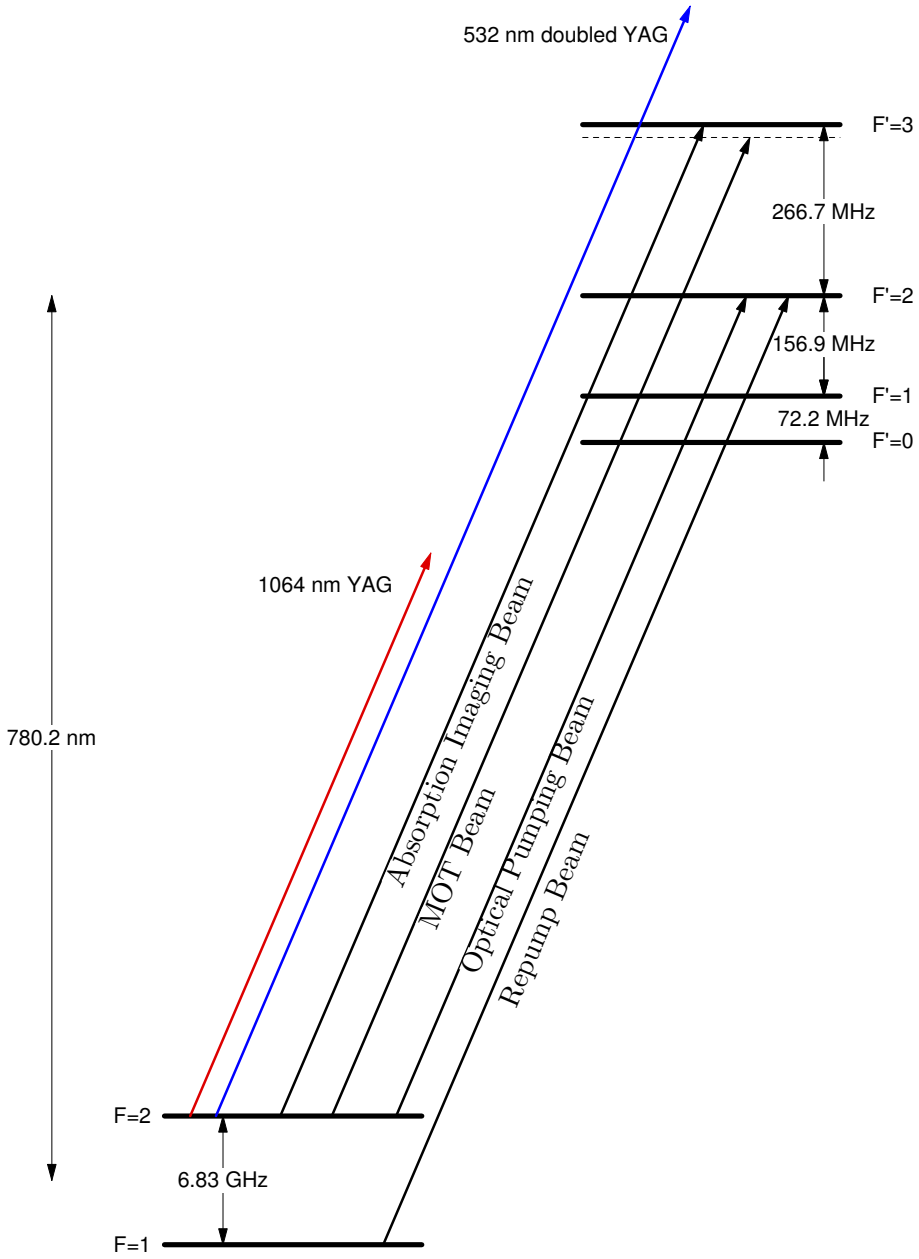

Figure 2.7: The multitude of laser frequencies used in the experiment.

Laser Diodes		
property	MLD780-100S5P	GH0781JA2C
distributor	Intelite, Inc.	Digi-Key
nominal wavelength	780 nm	784 nm
maximum output power	100mW	120mW
threshold current	30mA	30mA
operating current	120mA	140mA
maximum operating current	140mA	167mA
maximum reverse voltage	2V	2V
manufacturer	unknown	Sharp

Table 2.1: Characteristics of the lasers diodes used in the experiment.

the cooling cycle.

In addition to cooling and trapping the atoms, near resonant light is needed to move the atoms around, put them into specific internal states, and image them. The light used to perform these acts is generated by laser diodes. Due to the variety of frequencies required as well as the amount of light power necessary, this is accomplished with five diode lasers. Two of the diodes are master lasers that produce "seed light" at the two main frequencies necessary. To get the range of desired frequencies as well as increased power, the "seed light" is used to force three other diodes to have the same frequency as the master lasers, but with full power [29]. The specific frequencies are then realized through the use of acousto-optic devices.

2.3.1.1 MOT Master Laser

The MOT master laser produces the "seed light" on the $F = 2 \rightarrow F' = 3$ transition. The diode used for this is a MLD780-100S5P laser diode

procured from the online distributor Intelite, Inc. The diode is specified to have an output power of 100 mW with an injection current of 120 mA. The the output is single longitudinal mode with a nominal lasing wavelength of 780 nm (see Table 2.1).

Precise control of the laser frequency is necessary as well as a linewidth that is less than the natural linewidth of the atomic transition. This feat is accomplished by placing the diode within a Littrow configuration, grating-stabilized housing [30, 31]. The laser housing was slightly modified from the original design of Bruce Klappauf and Dan Steck in that the angle of the grating was adjusted to work at 780 nm. Aside from the angle modification, the original housing, the specifications of which can be found in Bruce's and Dan's dissertations, was unchanged [18, 21].

The basic idea behind the design is that the laser diode is part of an extended cavity formed by the reflective back surface of the diode and a grating used as a frequency sensitive output coupler. The grating is mounted at the Littrow angle (see Eq. 2.1) with respect to the diode so that the first order, which is frequency dependant, reflects back into the cavity. Diodes are extremely sensitive to feedback due to their wide gain bandwidth, so the back reflected beam injection locks the diode [29]. The zeroth order reflection from the grating forms the output beam. In practice, the output power from the MOT master laser system is ≈ 30 mW.

A slight modification was made to the original MOT master laser housing. In order for the first order reflection to be at the appropriate wavelength,

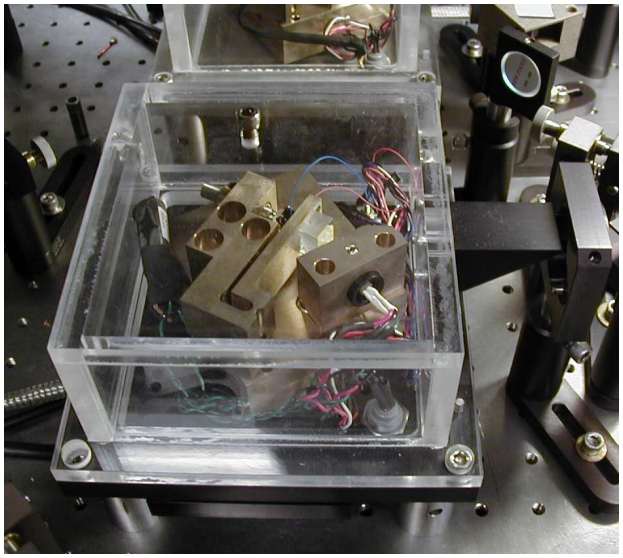

Figure 2.8: The master laser. This photograph shows the MOT master laser in its grating stabilized housing. The Plexiglass cover is used to provide thermal isolation from the environment.

the incident angle between the grating and the laser beam had to satisfy the Littrow condition

$$m\lambda = 2d \sin \alpha \tag{2.1}$$

where m is the order, d is the grating spacing, and α is the grating angle [32]. The grating has a ruling of 1200 grooves/mm or a spacing of $d = 0.833\,\mu$m. Therefore the angle was adjusted from 30.7°, which was used for 852 nm light, to 27.9°, which is appropriate for 780 nm light.

The master laser has superb spectral qualities. The laser is single mode in frequency with a measured linewidth of 1.5 MHz. This is actually an upper bound for that value. The linewidth was measured using a Fabry-Perot cavity

with a free spectral range of 300 MHz. The estimated finesse of the cavity based on the characteristics of the mirrors involved is about 200 giving a resolution of 1.5 MHz.

Despite the simple construction of the grating stabilized system, they are notoriously difficult set up for single mode operation on one of the ^{87}Rb absorption lines. Therefore, a quick explanation of the technique used to properly align the laser is in order. The diode is housed in a Thorlabs collimation tube, model LT230P-B. After adjusting the collimation tube lens to ensure the beam is well collimated, the free running diode is made to lase on one of the rubidium transition lines. This is accomplished by shining the laser through an absorption cell and adjusting the current until fluorescence is seen. At this point, the temperature of the diode is adjusted to optimize the operating current. If the current is too low or too high, the temperature is either lowered or raised, respectively, to remedy that. The temperature should be set so that the operating current is as close as possible to the nominal operating current listed on the data sheet while producing light at the transition wavelength.

At this point, the grating is added and adjusted so that the laser is self-injected. First, the diode injection current is lowered to just below the threshold level. There are now two approaches to determine if the grating is appropriately aligned for self-injection. If the current can be modulated, the current is scanned over the threshold current level and the power output of the diode is observed on an oscilloscope. The oscilloscope trace shows a very shallow slope until the threshold current is reached at which point the

curve makes a very sharp increase in slope. By adjusting the vertical angle of the grating, this curve will change shape. When the grating is appropriately aligned, the threshold current value will drop resulting in the turning point on the curve moving to a lower value, and in addition, the curve will become sharper at the turning point.

Since it is not possible for us to modulate the current with the existing current drivers, the grating was aligned by observing the shift in the threshold current by eye. Again, the injection current is reduced to just below the threshold level. At this point, the laser diode barely emits any light. The minute amount of light emitted by the diode is viewed with an infrared viewer while the vertical angle of the grating is adjusted. When the grating is aligned, the threshold current level will lower and the dim spot will become bright. The grating is aligned by setting the grating angle to maximize the brightness.

The grating stabilized laser will not necessarily be on one of the ^{87}Rb lines yet. To get the laser on one of the lines, the beam is put through an absorption cell and into a Fabry-Perot cavity. By adjusting the horizontal angle of the grating which adjusts the incident angle in this configuration, the frequency of the laser is swept. The system is appropriately aligned when the absorption cell fluoresces and the spectrum of the laser, obtained from the Fabry-Perot cavity, is single mode. It is possible that the cell will fluoresce but the laser will be multi-mode, therefore an iterative process of slightly changing the current (a few milli-amps) and readjusting the grating is performed to remedy this. The entire sequence is a bit time consuming, but once completed

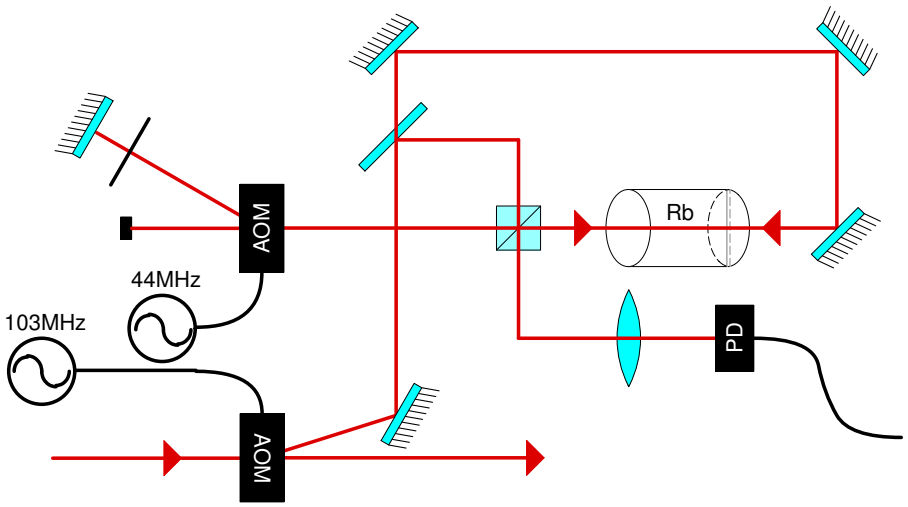

Figure 2.9: The MOT master laser locking setup. A small portion of the MOT master beam is sent through the depicted saturation absorption spectroscopy setup.

it does not have to be done again until the diode is replaced. The exact determination of which rubidium line the laser is operating on requires the use of a saturated absorption spectroscopy setup to see the hyperfine splitting which uniquely determines the line.

In order to determine if the laser is on the appropriate rubidium line as well as providing a means to lock the laser on that line, a portion of the MOT master laser is used used to perform saturated absorption spectroscopy [30, 32, 33]. This provides a Doppler-free background in order to see each of the $F = 2 \rightarrow F' = 1, 2, 3$ transitions as well as the cross-over transitions. From this, one can determine if the lasers are locked to the appropriate line.

Around 780nm, there are 4 Doppler broadened rubidium absorption lines, two outer lines for ^{87}Rb and two inner lines for ^{85}Rb. The standard means for determining the correct line is to measure the frequency splitting between the two outermost Doppler-free absorption peaks using a Fabry-Perot cavity. The ^{85}Rb peaks are very close together and are easily distinguished from the ^{87}Rb lines which are over 200 MHz apart. By closely inspecting the two ^{87}Rb lines, the $F = 2 \rightarrow F'$ line containing the MOT transition has a width of ≈ 425 MHz whereas the $F = 1 \rightarrow F'$ line containing the repump transition has a width of ≈ 230 MHz which is easily distinguished on our Fabry-Perot cavity.

A layout of the saturated absorption spectroscopy setup is shown in Fig. 2.9. A small portion of the MOT master laser is picked off with the use of a 103 MHz AOM. Roughly 1 mW of power is in the first order of this AOM, which is sent to the spectroscopy setup located on a separate table. Once there the beam is split into two with a 50% plate beam splitter. One half of the beam is sent through a polarizing beam splitting cube (PBSC) which directs the beam to an AOM. The AOM is driven by a frequency modulated signal with a center frequency of 44 MHz that oscillates from 40 MHz to 48 MHz at a frequency of 50kHz. The first order of the AOM goes through a $\lambda/4$ waveplate before being retro-reflected on a mirror with a 40 cm radius of curvature. The beam follows the first order back to the AOM where it is again diffracted. This allows the exiting beam not to move while the driving frequency of the AOM is modulated. The first order goes back to the PBSC where it passes through this time due to the orthogonal polarization. Upon passing through the cube,

the beam passes through a rubidium absorption cell.

The other beam created by the beam splitter travels around the absorption cell unaltered. On the opposite side, the beam enters the cell. The beam is aligned to overlap the double passed beam from the AOM which is 88 MHz higher in frequency. In the cell, the two beams interact with a velocity class of atoms corresponding to a frequency shift of 44 MHz. After passing through the cell, the beam is reflected by the polarizing beam splitting cube. The beam is focused with a 36 mm focal length lens onto a fast photodetector.

The signal generated by the photodetector is the doppler broadened absorption peak with dips at each of the $F = 2 \rightarrow F'$ transitions and crossover transitions. The signal is sent to an SRS lock-in amplifier, model number SR510. The lock-in amplifier receives the same signal used to modulate the frequency of the double passed AOM. The amplifier therefore generates a signal that is proportional to the derivative of the absorption dips on the photodetector signal minus the broad Doppler background. The dispersive signal at each transition provides a means to lock on to that particular transition.

The laser is locked onto the $F = 2 \rightarrow F' = 2/3$ crossover transition because of the fact that it is the strongest line in the dispersive profile. The pick-off AOM shifts the beam up by 103 MHz and the double passed AOM in the spectroscopy system shifts the velocity class up by another 44 MHz, therefore the output beam of the laser is 147 MHz red of the transition to which it is locked. Since the laser is locked to the $F = 2 \rightarrow F' = 2/3$ crossover transition which is 133 MHz red of the $F = 2 \rightarrow F' = 3$ cycling transition, the

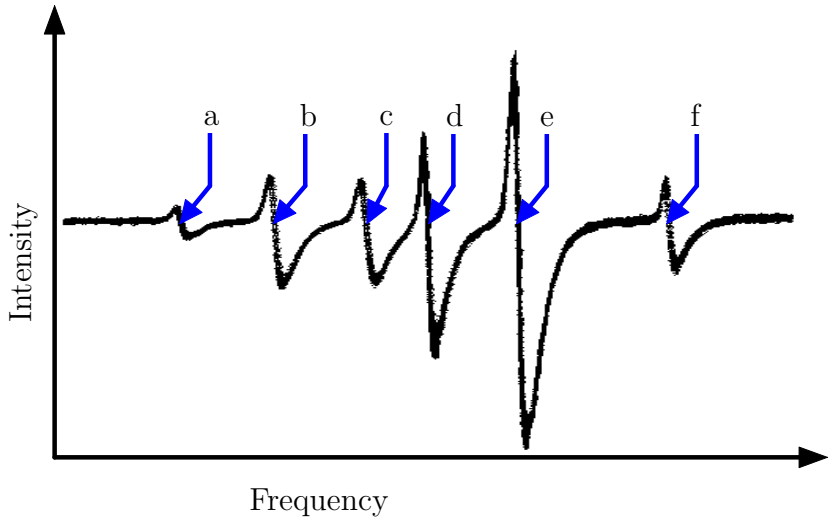

Figure 2.10: The MOT saturated absorption spectroscopy dispersive signal. The different dispersive lineshapes refer to the following transitions: a)$F = 2 \rightarrow F' = 1$, b)$F = 2 \rightarrow F' = 1/2$, c)$F = 2 \rightarrow F' = 2$, d)$F = 2 \rightarrow F' = 1/3$, e)$F = 2 \rightarrow F' = 2/3$, f)$F = 2 \rightarrow F' = 3$.

MOT master laser is 280 MHz red of the cycling transition.

This 280 MHz detuning from the cycling transition was deliberately planned. The reason for this is clarified in Fig. 2.11 which shows the distribution of the MOT master beam. After exiting the laser housing, the beam passes through an anamorphic prism pair to remove the 3:1 aspect ratio. It then passes through a ConOptics optical isolator, model 713, to protect it from stray back reflections. Immediately after the isolator is the 103 MHz AOM used to pick off a portion of the light for the saturated absorption lock. The zeroth order of the AOM continues on to a double passed acousto-optic deflector (AOD). This deflector has a central frequency of 80 MHz and a 3 dB bandwidth of 40 MHz. By using the first order in the double pass, the frequency of the MOT master beam is raised anywhere from 120 MHz to 200 MHz. This gives the MOT master laser a detuning of 80 MHz to 160 MHz red of the cycling transition. By using an 80 MHz AOM as a fast shutter, the MOT master beam will have a detuning of somewhere between on resonance and 80MHz red. This is the needed range of detunings for the successful operation of the experiment. It allows for processes such as absorption imaging which needs light exactly on resonance, to MOT loading which needs light approximately 3γ, or 18 MHz, red of resonance, to polarization gradient cooling which requires detunings up to 60 MHz red of the cycling transition.

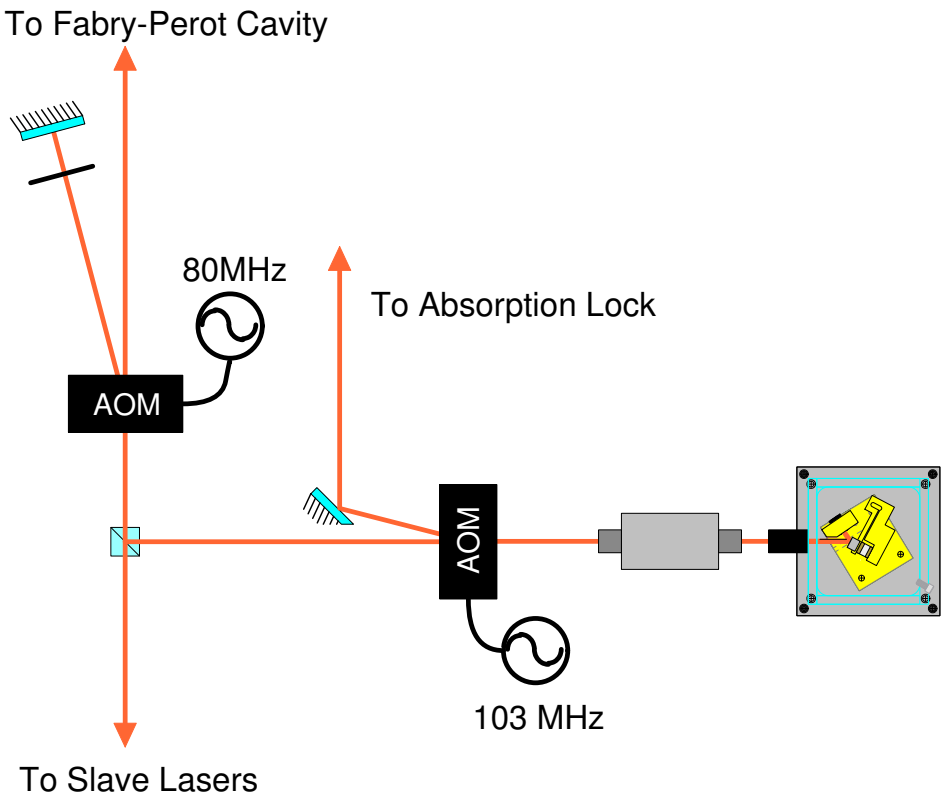

Figure 2.11: MOT master laser distribution scheme. The light from the MOT master laser goes through different frequency shifting devices in order to correctly set the frequency of the light before it is used to injection lock the slave lasers.

2.3.1.2 Slave Lasers

Unfortunately the master laser alone does not produce enough power to create beams for the upper and lower MOTs as well as the auxiliary beams used for imaging and optical pumping. Therefore, additional lasers, known as "slave" lasers, are used to meet the power requirements of the experiment. In order to guarantee that the slave lasers are identical to the MOT master, they are injection locked to the MOT master [29]. This gives us the full power of three free-running laser diodes with the same spectral qualities as that of the MOT master laser.

Each slave laser on its own is simply a free running laser diode. The Digikey laser diodes (see Table 2.1 for specifications) are used for the slave lasers. The diodes reside in a Thorlabs collimation tube, model LT230P-B, with 4.5 mm focal length collimation lens and numerical aperture of 0.55. The tube sits within a 2"x1.5"x0.65" block of bronzed aluminum atop a Melcor thermoelectric cooler (TEC), model CP 1.0-63-08L. A 50 kΩ thermistor is used with the TEC to regulate the temperature of the diode. The Wavelength Electronics WTC3243 provide the control electronics for the temperature regulation. The hot side of the TEC rests on the anodized aluminum housing that surrounds the diode. There are two electrical connectors for the temperature controller and the current controller. There is also an output window made from a microscope slide fixed at the brewster angle.

To ensure that the slaves have the appropriate spectral output, they are injection locked [29, 31]. This is accomplished by directing a small amount

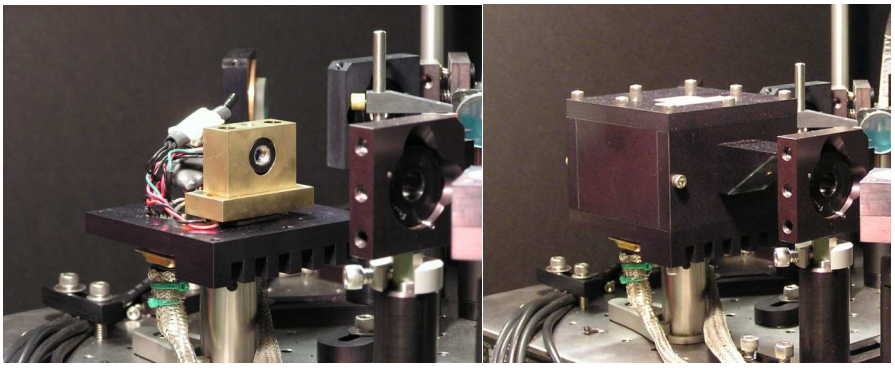

Figure 2.12: Pictures of the slave lasers. The image on the right shows the slave laser housing complete with the outer covering. The image on the left shows the housing minus the cover allowing one to see the laser diode holder as well as the electrical connections.

of light from the masters into the diode. If the spatial profile is well matched, the slave will have identical spectral properties as the master with all the power of a free running diode. The unique properties of the optical isolator which is located after each slave allows for injection. Appropriately polarized light is introduced into the rejection port of the optical isolator. Since the crystal in the isolator rotates the polarization the same direction regardless of propagation direction, the injected beam exits the optical isolator with the same polarization as the laser diode. It is then aligned to be co-linear with the output beam of the laser diode. Figs. 2.15, 2.13, and 2.16 illustrate how the injection beam enters the laser diode.

In practice we use approximately 2 mW of power to injection lock the slave lasers. Little effort was made to better match the spatial profile of the injection beam to that of the slave laser output. By doing so, it would be

possible for the injection power to be lowered to something on the order of several hundred microwatts as some other groups have used [34].

As with the master lasers, there are special techniques involved with aligning the diodes for injection locking. Like before, the current and temperature of the free running diode are adjusted so that the output beam fluoresces in the rubidium absorption cell. At this point the injection beam is aligned to be counter propagating with the diode output beam. The diode output beam needs to be analyzed on a Fabry-Perot cavity now. While sweeping the frequency of the injection beam, the spectrum of the slave laser is observed. If the above procedure was done correctly, there should be a peak corresponding to the free running laser and a small peak that sweeps in frequency corresponding to the injection locked portion of the slave. Now several things can be optimized. First, the operating current of the slave is adjusted to maximize the injected peak. Then the alignment of the injected beam is adjusted to increase the injection locked portion of the slave laser. Finally, when those two are optimized, the injection beam power is adjusted. The minimum power required is ideal. This process can be iterated to make the locking more efficient by lowering the injection beam power so that the slave is not completely injected. The current and alignment are then optimized to relock the slave. This procedure is iterated until satisfied.

A vast distribution networks exist to take the beams from the laser diodes to the vacuum chamber where they interact with the atoms. The beams need to be precisely shaped and have specific frequencies in order to be useful

for trapping, cooling, and imaging the atoms. As the beams make their long journey (approximately 5 meters) to the chamber, they are shaped into their useful form.

The three slave lasers are labelled according to their primary function. Two slaves create the upper MOT beams and are labelled Upper MOT Horizontal and Upper MOT Diagonal. The other slave is simply named Lower MOT. In addition to serving in their primary capacity, they also perform auxiliary jobs according to how much power they have to spare.

Upper MOT Horizontal Slave Laser Fig. 2.13 shows the distribution of the Upper MOT Horizontal slave laser. Upon exiting the slave laser housing, the beam is sent through an anamorphic prism pair (not shown in Fig. 2.13) to give the beam an aspect ratio of unity. From there the beam passes through a ConOptics optical isolator, model 712B. Due to the extremely broad gain profile of diode lasers, they are extremely sensitive to back reflections. The optical isolator supplies approximately 36 dB attenuation of any back reflected beam alleviating this problem.

The optical isolator serves another purpose. It provides the optical port to inject the slave laser with a portion of the MOT master beam. The exit port of the optical isolator is a PBSC. By sending in a beam in the side port orthogonal to the exiting beam, the input beam is appropriately rotated in the Faraday rotator to exit the PBSC that is at the entrance of the optical isolator. The injection beam has the same polarization as that of the slave

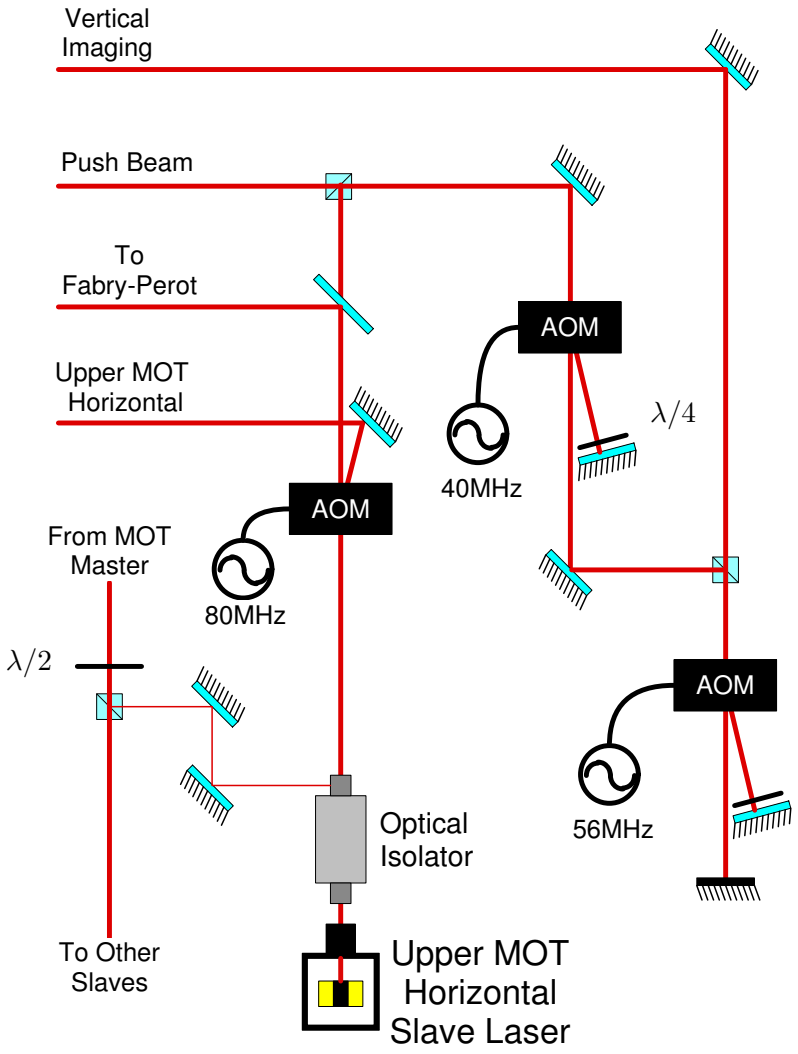

Figure 2.13: Beam distribution for the Upper MOT Horizontal slave laser.

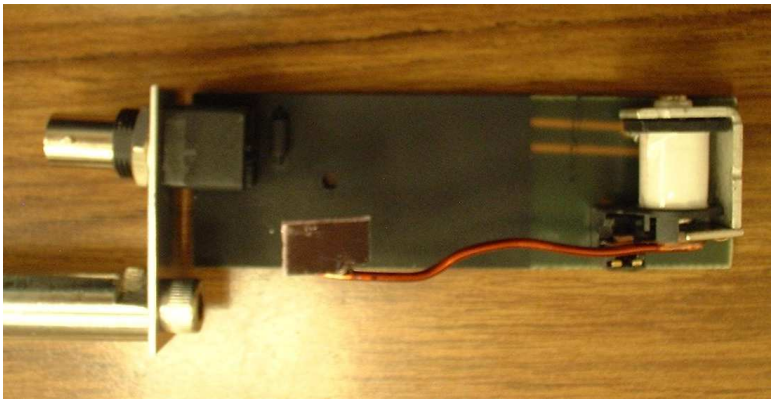

Figure 2.14: Picture of the homebuilt shutters used in the experiment.

laser beam and, by using the two mirrors prior to the isolator, can be made co-linear with the slave beam.

After the beam leaves the optical isolator, it passes through an 80 MHz AOM. This AOM serves two purposes. First, it shifts the frequency of the beam up by 80 MHz. By using the first order of this AOM, the MOT beam can be tuned from 80 MHz red of resonance to exactly on resonance. In addition to shifting the frequency, the AOM provides intensity control by adjusting the amount of power in the first order. To ensure good turn off of the first order, a digitally controlled RF switch is between the signal source and the RF amplifier that drives the AOM.

The first order beam from the AOM is shaped and sent to the upper chamber to create the upper horizontal MOT beam. As a separate measure to guarantee that there is no leakage light in this beam, a homemade mechanical shutter is placed in the beam path (see Fig. 2.14) [35]. The shutter is nothing

more than a relay with an extended arm on it. On the end of the arm is a flag made from a razor blade. By driving current through the relay coil, the arm can be moved and the flag made to block the beam. The mechanical shutter takes on the order of several milliseconds to close. This is too slow for us, therefore the AOM is used as a fast, imperfect shutter and the mechanical shutter is used as a slow shutter with total extinction.

The zeroth order beam of the first AOM is used for additional purposes. In the beam path an optical flat uncoated on one side is used to pick off a small fraction of the beam. This is sent to a Fabry-Perot cavity to monitor the slave laser. After passing through the optical flat, the beam continues to the first of two double passed AOMs. The first double passed AOM is used to create the push beam. Since the upper MOT horizontal beam does not need the full power of the slave laser, this is the ideal means by which to create the push beam which necessarily must be on at the same time as the upper and lower MOTs. The first order of the AOM passes through a $\lambda/4$ waveplate and is retro-reflected back through the AOM. It traces the input beam back to a PBSC where it is ejected due to the orthogonal polarization. The beam was created using a double pass to allow the detuning of the beam to be changed while preserving the beam alignment. In practice, the detuning has never been adjusted. Upon ejection from the polarizing beam splitting cube, the beam is spatially filtered and sent to the upper MOT chamber.

The second double pass is built around the zeroth order of the first double pass and is used to generate the vertical imaging beam. The first order

of this AOM is again sent through a $\lambda/4$ waveplate before being retro-reflected. The beam is extracted with a PBSC and then spatially filtered. At this point the beam is sent to the upper MOT chamber. The double pass is not chosen for freedom of tuning but rather for the larger frequency shift achievable.

Upper MOT Diagonal Slave Laser Fig. 2.15 shows the optical distribution network for the Upper MOT Diagonal slave laser. As the name suggests, this laser is used to create the upper MOT diagonal beams. The beginning of the distribution scheme is identical to that of the Upper MOT Horizontal slave. The beam emerges from the slave laser housing and is made circular with an anamorphic prism pair. The beam then passes through an optical isolator to protect the slave laser from unwanted back reflections as well as provided an injection beam port for injection locking.

After leaving the optical isolator, the beam is sent through an 80 MHz AOM that serves as both a frequency shifter and power control. The first order is shaped and sent to the upper chamber to become the upper MOT diagonal beams. Within the optical path of the shaping optics a home built shutter is situated to guarantee that there is no leakage light.

The zeroth order from this AOM is used to create two different beams. The beam is first double passed through a 56 MHz AOM. The first order of the AOM is used in the double pass thereby raising the frequency of the beam by 112 MHz. This beam will become the horizontal absorption imaging beam. After the double pass, the beam is separated with a PBSC. At this point the

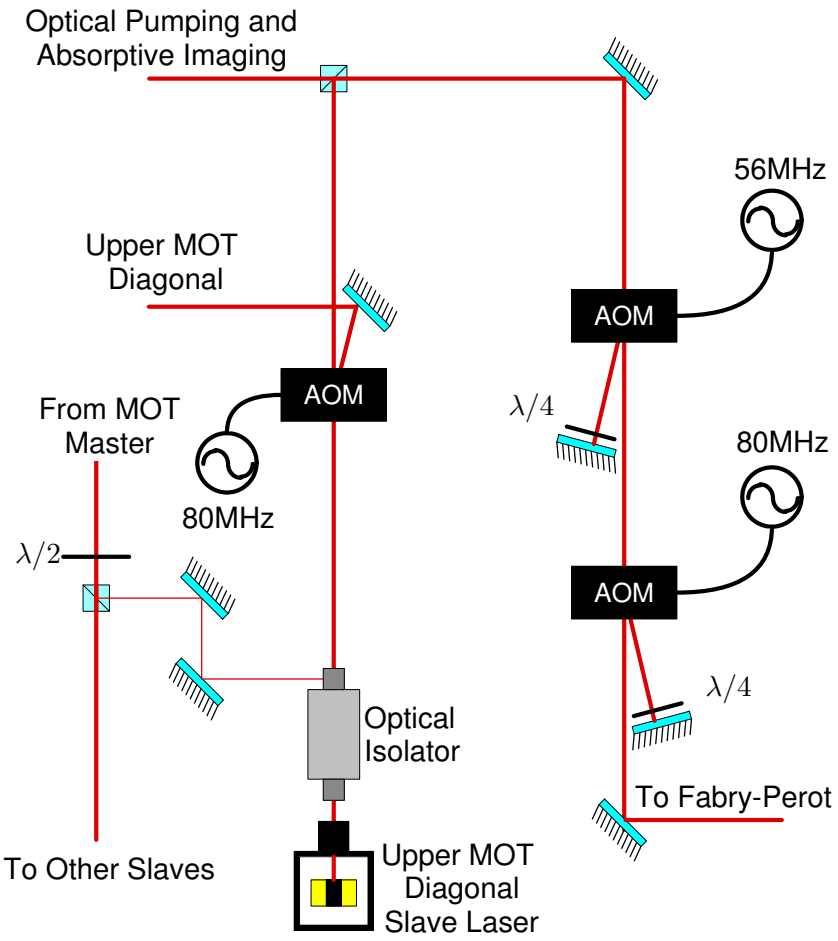

Figure 2.15: Beam distribution for the upper MOT diagonal beam slave laser.

beam is spatially filtered and expanded to a waist of approximately 15 mm. The beam is then sent to the chamber to be used for absorption imaging.

The zeroth order of the first double pass is used to create the optical pumping beam. This beam is double passed through an 80 MHz AOM. In this case though, the minus one order is used thereby lowering the frequency of the beam by 160 MHz. By tuning the MOT master appropriately, this puts the frequency of this beam on resonance with the $F = 2 \rightarrow F' = 2$ transition. After the double pass, the beam is separated from the input beam with the same PBSC used for the absorption imaging beam. The waist is roughly the same as the absorption imaging beam, 15 mm, and the optical pumping beam follows the same path to the lower chamber where it enters at the same place as the absorption beam.

Lower MOT Slave Laser The lower MOT light is generated by the Lower MOT slave laser. The distribution network for this laser can be seen in Fig. 2.16. This slave laser is used for only one purpose, which is to create the lower MOT beams. That being said, there are two different types of MOT beams. The regular MOT beams are the standard MOT beams that are used for loading the atoms as they are transferred to the lower chamber. The tiny MOT beams are used for a more specialized set of circumstances, that of detecting single atoms at the center of the lower chamber. More will be discussed about single atom detection later (see Chapter 5). For now, the creation of both beams will be discussed.

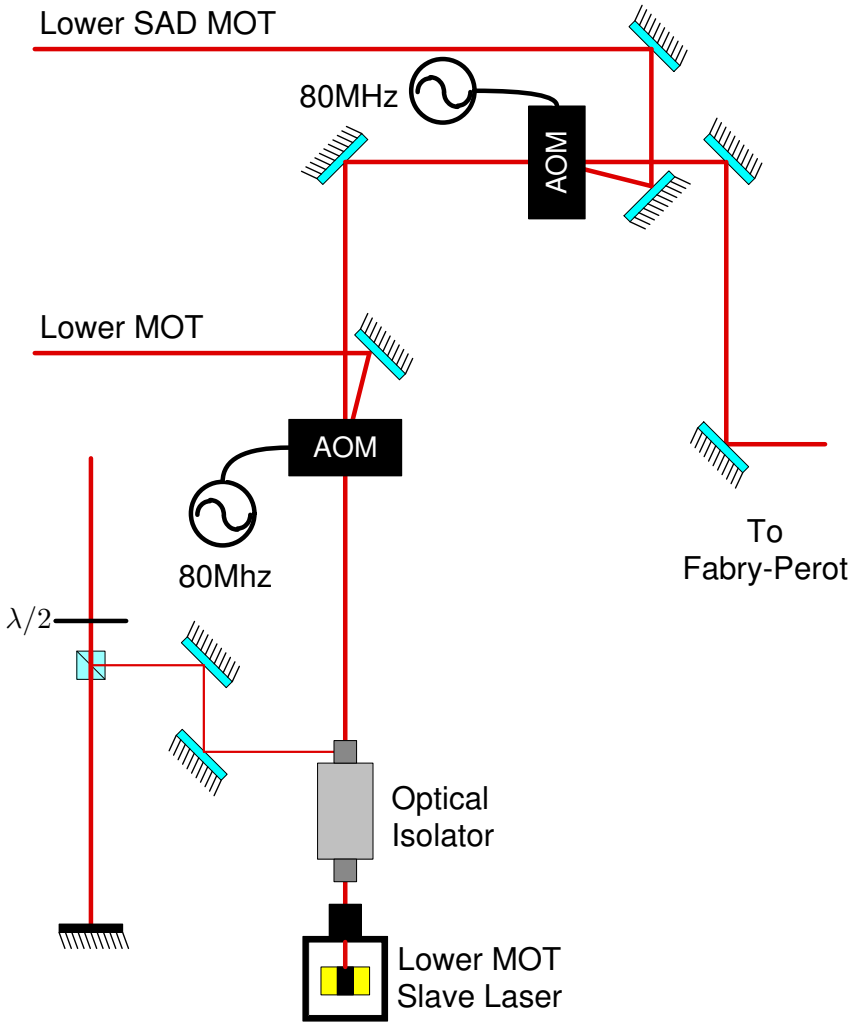

Figure 2.16: Beam distribution for the lower MOT beam slave laser.

As with the other two slave lasers, the output of the laser is sent through an anamorphic prism pair to make the beam circular. Following the prism pair, the beam passes through an optical isolator for protection from back reflections and to provide a means for injection locking. From there the beam is sent to an 80 MHz AOM.

The first AOM is used to shift the frequency and provide intensity control. The first order from this AOM passes through a mechanical shutter to ensure that the lower MOT light is completely extinguished when required. After passing through the shutter, the beam is shaped and spatially filtered. From there, the beam is sent to the lower MOT chamber.

The zeroth order beam from the first AOM is used to created the single atom detection (SAD) MOT beams. This beam is again sent to an 80 MHz AOM that serves the same purpose as the first AOM. In fact, the entire optical path of the SAD MOT beams is identical to that of the regular MOT beams. The only difference occurs when the beam is shaped before entering the chamber. The size of the SAD MOT beams is much smaller than that of the regular MOT beams. The reasons for this will be addressed later (see Chapter 5).

2.3.1.3 Repump Master Laser

The other frequency necessary to create a MOT is provided by the repump beam. As mentioned earlier, light on the $F = 1 \rightarrow F' = 2$ transition is needed to return atoms to the cycling transition which may have decayed into

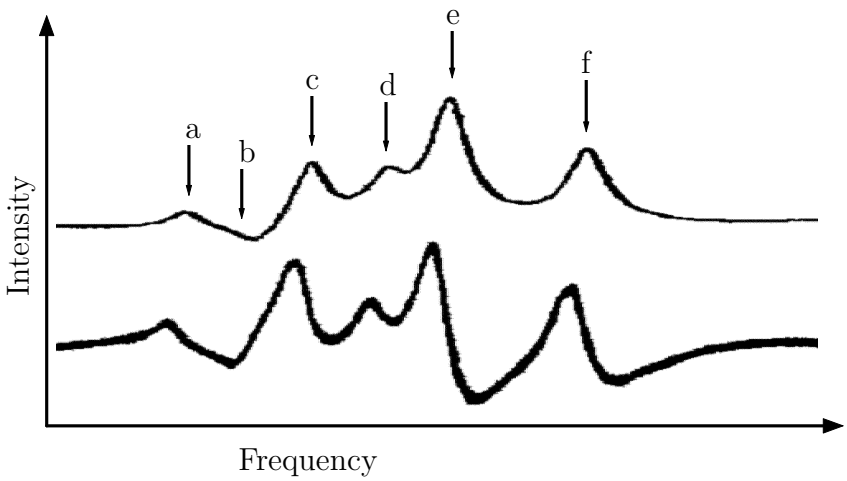

Figure 2.17: Repump saturated absorption profile. The different dispersive lineshapes refer to the following transitions: a)$F = 1 \rightarrow F' = 0$, b)$F = 1 \rightarrow F' = 0/1$, c)$F = 1 \rightarrow F' = 1$, d)$F = 1 \rightarrow F' = 0/2$, e)$F = 1 \rightarrow F' = 1/2$, f)$F = 1 \rightarrow F' = 2$.

the $F = 1$ ground state. To create this light, another Littrow configuration, grating-stabilized laser housing containing a MLD780-100S5P laser diode was constructed. This laser is identical to the MOT master laser in every way except that it is locked to the repump transition 6.83 GHz higher in frequency. All the relevant information for the repump master laser housing can be found in the previous section.

As was the case with the MOT master, the repump master is locked to the repump transition through the use of absorption spectroscopy. A small portion of the light from the repump master is picked off from the beam using a waveplate and a polarizing beam splitting cube and used to lock the laser to the $F = 1 \rightarrow F' = 1/2$ crossover. The setup to lock the repump laser is

identical to the way it was for the previous cesium experiment and is described elsewhere [18, 21, 22]. Fig. 2.17 shows the saturated absorption profile for the repump transition line along with the dispersive signal corresponding to the derivative of the absorption signal. The laser is locked on to the strongest dispersive line which is the $F = 1 \rightarrow F' = 1/2$ crossover transition. Therefore, the output of the repump laser is 78.5 MHz red of the repump $F = 1 \rightarrow F' = 2$ transition.

It is necessary to distribute the repump laser to both the upper and lower MOTs. Fig. 2.18 gives a schematic of how the repump is split between the two systems. As with all of the diode lasers, the output of the repump is made circular with an anamorphic prism pair before passing through a ConOptics optical isolator, model 713, for protection against back reflections. From here the repump beam is sent through an 80 MHz AOM which serves the dual purpose of shifting the frequency of the repump beam up 80 MHz and therefore nearly on resonance with the repump transition, but it also acts as a fast shutter for the repump beam. The 80 MHz AOM leaves the repump beam detuned 1.5 MHz red of the $F = 1 \rightarrow F' = 2$ transition, but this does not appear to affect the operation of the MOT. As an added guarantee for complete extinction of the repump, an additional home-built shutter is placed within the distribution scheme.

Since very little power is needed in the repump beam, only the repump master laser is necessary. After passing beyond the protection shutter, the beam passes through a $\lambda/2$ waveplate and a polarizing beam splitting cube to

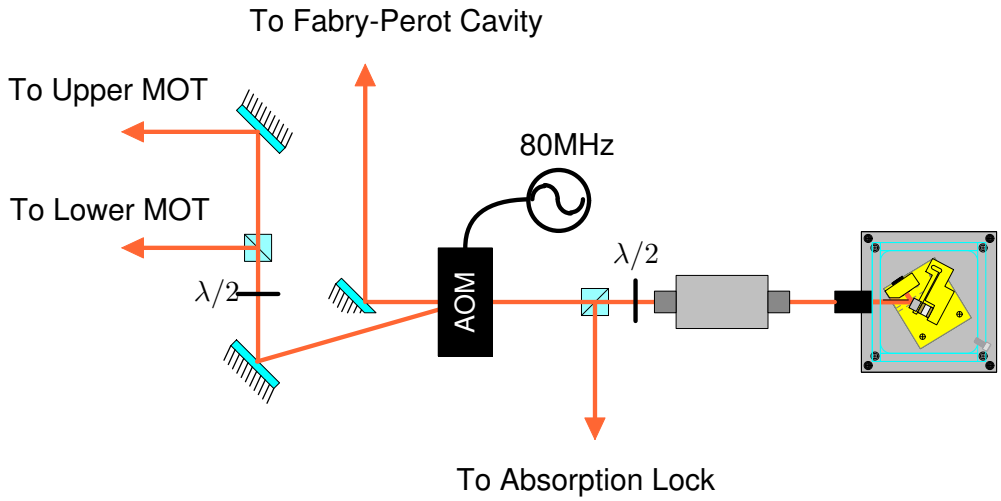

Figure 2.18: The distribution network for the repump grating stabilized laser.

split the beam between the upper and lower MOTs. Typically, the waveplate is set so that 5 mW are sent to the upper MOT while 4 mW are sent to the lower MOT. This repump splitting was chosen as it gave the best fully loaded lower MOT even through both MOTs appear to be relatively insensitive to the exact power in their own repump beam.

2.3.1.4 Laser Diode Control Electronics

Both the master lasers and the slave lasers are operated with home built current controllers [36]. The controller was designed to supply up to 500 mA with a set current limit dependent on the diode used. Measuring current noise with the current output monitor through a bandpass amplifier, under test conditions of $I_{out} = 200$ mA, there was an observed rms noise of about

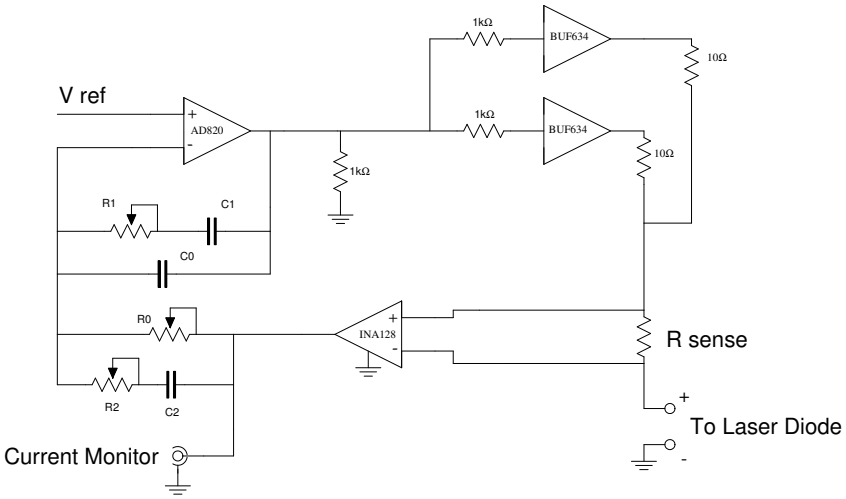

Figure 2.19: A simplified schematic for the laser diode current controller circuit. A full schematic can be found in Ref. [36].

$100\,\mu V_{rms}$ on a 2 V dc signal in the 2 Hz to 200 kHz band. This corresponds to $5 : 10^5$ rms current noise. In the 2 Hz to 20 kHz band, the rms noise was about $20\,\mu V_{rms}$, which is about $1 : 10^5$ rms current noise. The drift is limited by the sense resistor which is between -50ppm/C and 100ppm/C according to the manufacturer. Self-heating of the sense resistor is rather small and most changes are likely to be due to ambient temperature variations. More practically, we have observed drift under $1 : 10^4$ on the few hour scale from tens of seconds after turn on. Longer term drift is expected to be on the order of $1 : 10^5$ stemming from the long term stability of the voltage reference.

The current controller design is based on a standard PID feedback loop

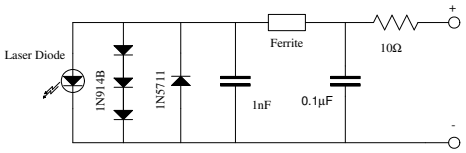

Figure 2.20: The laser diode protection circuitry.

and a buffered current output as shown in Fig. 2.19. The current sense is done with a Caddock SR10 1 Ω 4-point sense resistor and measured by an INA128 instrumentation amplifier. The amplifier is set to have a gain close to 10 and may be trimmed for accuracy giving a current monitor of 1 V for every 100 mA of output current. This trimming is for the purpose of removing the small absolute error of the sense resistor, if such accuracy is desired. In principle, however, it is only really important to have noise-free operation and stability rather than accuracy. We trimmed the output accuracy to under 0.1%. The PID is in a single opamp configuration, where the various time constants are coupled. This is hardly a problem in this circuit. In general, one can think of C0 as the high frequency roll-off, C1 and R0 as the integrator, R1/R0 as the proportional gain level, and R2 and C2 with R1 as the differential. We found excellent performance without the differential part of the circuit, simply omitting these components (R2 and C2) and using fixed resistors of values R0=R1=4.99 kΩ and capacitors C0 of 39 pF and C1 of 10 nF. This gives an integration bandwidth of about 20 kHz and a unity proportional level.

Laser diodes are extraordinarily sensitive to shocks. In fact, electrocution is the number one cause of death for laser diodes [30, 31]. In order to protect against this untimely death, the protection circuit shown in Fig. 2.20 was added to each diode. Several forward and reverse biased diodes were added to prevent the voltage from swinging too high in either direction. In addition, a ferrite bead and a low pass filter were added to reduce any noise that may be picked up by the cable connecting the laser diodes to the current driver.

2.3.2 Interaction Lasers

In addition to the laser diodes, there are two far off resonant lasers used in the experiment. Due to their far detuning and high power, they produce excellent conservative traps with negligible spontaneous emission (see Appendix A). In order to have both attractive and repulsive potentials, one laser is situated to the red of the Rubidium atomic transition and the other is to the blue side.

The repulsive potential is created by a Verdi laser manufactured by Coherent, Inc. The Verdi is a diode pumped, frequency doubled Nd:Vanadate solid state laser. Two laser diode assemblies pump the Nd:Vanadate crystal. The output of the crystal is frequency doubled with a lithium triborate (LBO) crystal held at a constant temperature of 151°C. An optical diode and an etalon are used to ensure single frequency mode operation. The output of the Verdi is 10 W CW at 532 nm with a specified linewidth of less than 5 MHz. Coherent specifies a power stability of $\pm 1\%$ over a 2 hour period and noise of

less than 0.1% in the 10 Hz to 1 GHz range.

The attractive potential is generated by a Ytterbium fiber laser, model YLD-10-1064, produced by IPG Photonics. The laser consists of several multimode, 1 W, laser diodes operating at 970 nm that pump an Ytterbium doped fiber. From this, 10 W of CW laser power at 1064.4 nm is produced. The fiber has an emission bandwidth of $\approx$ .31 nm and the annoying feature of random polarization. The output power instability (over 4 hours) is on the order of 1% while the short term stability, in the frequency range of 1 kHz to 20 MHz, is on the order of 0.8%.

2.4 Magnetic Trap

One of the easiest way to create a BEC is through magnetic trapping and evaporative cooling. This requires a magnetic trap that avoids the problem of Majorana flip loss (as in a quadrupole trap), but it was preferred to remove some of the complexities of other magnetic traps (i.e. the standard Ioffe-Pritchard trap and variants). The Quadrupole Ioffe Configuration (QUIC) trap, first designed by the group of Theodor W. Hänsch, fills that role [27].

2.4.1 Quadrupole Ioffe Configuration

The QUIC trap consists of three coils: a quadrupole coil pair and a Ioffe coil as shown in Fig. 2.21. Alone, the pair makes a quadrupole magnetic field, which is suitable at lower currents for running a MOT. This is a principle advantage to this magnetic trap, in that others require more difficult mode

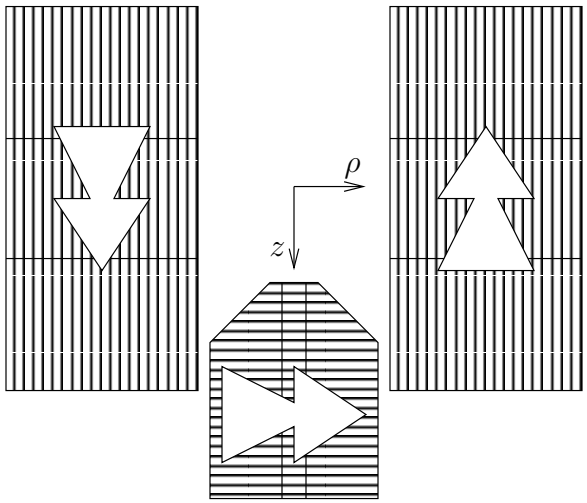

Figure 2.21: Top view of the QUIC trap. The trap consists of a quadrupole coil pair and a Ioffe coil. Alone, the pair makes a quadrupole magnetic field, which is suitable at lower currents for running a MOT. The large arrows show the direction of the current in the coils.

matching to transfer atoms from a MOT into the trap.

The basic idea of operation is that the quadrupole coil pair run at a low current to provide the fields for a MOT. At some point, the atoms may be optically pumped into a trapped state of the magnetic trap and the coil currents then ramped up to make a quadrupole magnetic trap. The MOT atoms are in the same location as the magnetic trap, so mode matching of the traps is not needed. Now, before evaporatively cooling, the Ioffe coil current is ramped up to equal that of the quadrupole coils. At this point, with identical current in all coils, the fields have maximum stability. Also, the magnetic trap is now compressed and is suitable for evaporative cooling. The disadvantage of this design is that the field minimum has moved toward

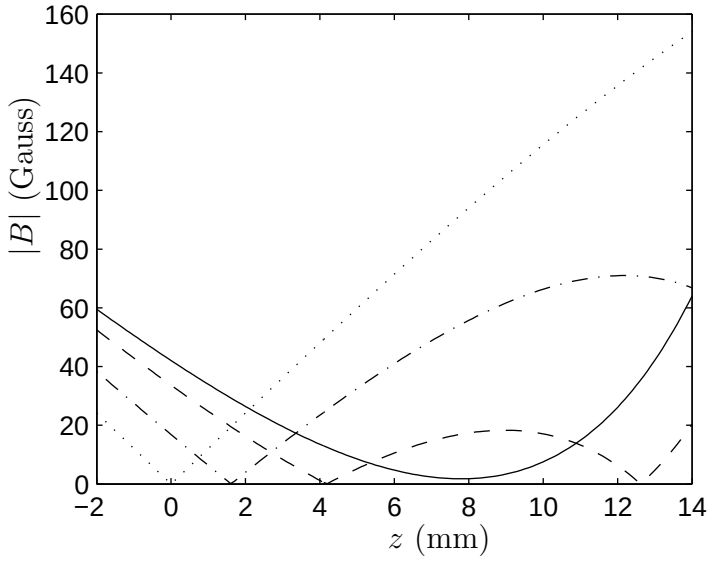

Figure 2.22: Calculated field for our QUIC trap. Field magnitude along the z-axis is shown for different situations. In all cases, the current in the quadrupole coils is $I_Q = 25\,\mathrm{A}$. The dotted curve is for Ioffe current $I_I = 0\,\mathrm{A}$, which corresponds to the case of a purely quadrupole field. The dot-dashed and dashed curves correspond to $I_I = 10\,\mathrm{A}$ and $I_I = 20\,\mathrm{A}$, respectively. The solid curve is when $I_I = I_Q = 25\,\mathrm{A}$. This curve corresponds to a situation with trap frequencies of $\omega_z = 2\pi \cdot 18\,\mathrm{Hz}$ and $\omega_{rad} = 2\pi \cdot 225\,\mathrm{Hz}$ with $B_0 = 1.8\,\mathrm{G}$.

the Ioffe coil. This places a limit on optical access to the BEC. Figure 2.22 shows the field magnitude along the z-axis while transferring from a purely quadrupole to the quadrupole-Ioffe trap.

The QUIC trap fields are similar to those of a standard Ioffe-Pritchard configuration near the trap minimum [37]. A vector field plot is shown in Figure 2.23. The potential, $V(\mathbf{r}) = \mu|B(\mathbf{r})|$, near the minimum is given by

$$V(\mathbf{r}) = \mu B_0 + \frac{m}{2}(\omega_z^2 z^2 + \omega_\rho^2 \rho^2)\,, \tag{2.2}$$

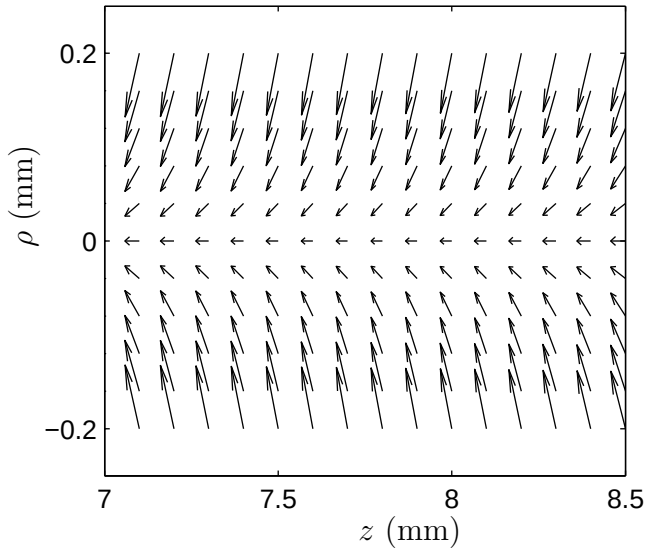

Figure 2.23: Vector field plot for the compressed QUIC trap. The lower axis is z, the distance from the pure quadrupole zero. The Ioffe coil is located to the right.

where $\mathbf{r}$ is specified by axial, z, and radial, ρ, components relative to the field minimum, and m is the atomic mass. This is a harmonic potential with trap frequencies given by $\omega = \sqrt{\mu B''/m}$, where B'' is the field curvature in the given direction. In the case of the radial direction, the curvature is

$$B''_\rho = \frac{B'^2_\rho}{B_0} - \frac{B''_z}{2}\,. \tag{2.3}$$

This is approximately $B''_\rho \cong B'^2_\rho/B_0$ when the coil currents are equal (i.e. B'_ρ is large and B_0 small). The trap frequencies are therefore given by

$$\omega_z = \sqrt{\mu B''_z/m}\,, \tag{2.4}$$

and

$$\omega_\rho = \sqrt{\mu B'^2_\rho/mB_0}\,, \tag{2.5}$$

where B'_ρ is the radial field gradient, B''_z is the axial field curvature, and B_0 is the field minimum. Since the quadrupole trap has gradients $B'_x = B'_y/2$, where B'_x is the gradient along the quadruple coil axis, the radial gradient is the geometric mean: $B'_\rho = \sqrt{B'_x B'_y} = B'_x/\sqrt{2}$. For the $|F = 2, m_F = +2\rangle$ ground state of ^{87}Rb, the factor $\sqrt{\mu/m} = 2\pi \cdot 1.2765\,\mathrm{Hz}$ and the trap frequencies are

$$\omega_z = 2\pi \cdot (1.2765\,\mathrm{Hz}/\sqrt{\mathrm{G/cm^2}})\sqrt{B''_z}\,, \tag{2.6}$$

and

$$\omega_\rho = 2\pi \cdot (1.2765\,\mathrm{Hz}/\sqrt{\mathrm{G/cm^2}})\; B'_\rho/\sqrt{B_0}\;. \tag{2.7}$$

At $I_I = I_Q = 25\,\mathrm{A}$, theoretical values are $B'_\rho = 235\,\mathrm{G/cm}$, $B''_z = 195\,\mathrm{G/cm^2}$ and $B_0 = 1.8\,\mathrm{G}$. This corresponds to trap frequencies of about $\omega_z = 2\pi \cdot 18\,\mathrm{Hz}$ and $\omega_\rho = 2\pi \cdot 225\,\mathrm{Hz}$. Small adjustments in B_o are made by an auxiliary Ioffe coil, thus setting the operating value of ω_{ax}.

2.4.2 Coil Structure and Construction

The approximate dimensions of the coils are as follows. The quadrupole coils have a 34 mm inner diameter, a 68.5 mm outer diameter, and a 32 mm thickness. The Ioffe coil has a partially conical end, with a 7.5 mm inner diameter, a 26 mm outer diameter, a 37 mm inner thickness, and a 33 mm outer thickness. The quadrupole coils are separated by 75 mm (between the centers of the coils) and the Ioffe coil is displaced 38 mm from the quadruple center to its center. These dimensions should not be taken too seriously, because they approximate the shape of the actual round wires and their locations.

Fig. 2.24 shows the coils and location of the magnetic wire. Each coil is wound around a PVC rod and encased in a water-tight PVC holder for cooling (see below). The Ioffe coil has 4 layers of windings with 20 gauge magnet wire. There is a set of 1/16" nylon rods from Small Parts, Inc. oriented perpendicular to the direction of winding between each layer. The coil was wound such that there is a spacer layer, 42 turns, a spacer layer, 41 turns, a spacer layer, 39 turns, another spacer layer, and finally 37 turns for a total of 159 turns. The quadrupole coils use 14 gauge magnet wire and have a set of 3 layers of turns then a nylon spacer followed by another set of 3 layers and spacer followed by a set of 4 layers. The number of turns per layer are: spacer, 18, 17, 18, spacer, 18, 17, 18, spacer, 18, 17, 18, 17. This is a total of 176 turns for each quadrupole coil.

To wind the coils, a pair of Teflon winding blocks was made to hold the inner PVC rod in a lathe which was slowly turned by hand. Teflon was used since epoxy does not stick to it strongly. Around the inner rod and after each subsequent layer of turns for the Ioffe coil, or after 3 layers of turns for the quadrupole coils, a set of spacers was put in place with 5 minute epoxy. These rods were placed around the the circumference of the coil approximately 1/2" to 3/4" apart and oriented perpendicular to the windings. After each coil was completed, it could easily be removed from the Teflon blocks. Each coil was then glued with a much stronger 24 hour epoxy called Cold Weld from Permatex. This gluing was in various places, mostly on the outside, along the rim to make sure the coil can not unwind in anyway, at the ends of the spacers

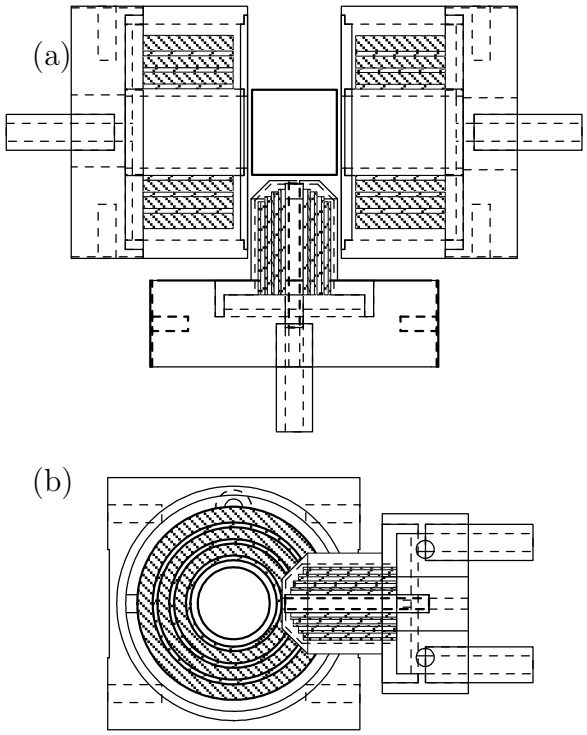

Figure 2.24: The three primary coils of the QUIC trap: (a) top view, (b) side view. Magnet wire is encased in PVC holders. The darker regions represent the copper wires and the lighter regions between the wires represent the nylon spacers. The spacers are oriented perpendicular to the coil turns. That is, in (a) all spacers are parallel with the plane of the paper and in (b) spacers come out of the paper for the quadrupole coils and parallel to the paper for the Ioffe. The PVC rods exiting the rear of each coil form base is a water tube connector.

to make sure there is a solid connection between them and the wire, and also from the wire and spacers to the inner PVC rod. This epoxy was intended to provide additional support for the coil against any strain and reinforce the 5 minute epoxy which may weaken in water. Great care was taken to not scratch the wire in this process.

Figure 2.24 shows machine drawings of the PVC coil holders with approximate dimensions of the magnet wire inside. The darker regions represent the copper wires and the lighter regions between the wires represent the nylon spacers. The spacers are oriented perpendicular to the coil turns. The inner PVC rods were then inserted into the PVC holders. Each holder has a base piece and an inner rod. Both holders have a single hat piece. In the case of the Ioffe coil, that piece fits over the the entire coil and attaches to the base piece. For the Quadrupole coils, the hat slips down the inner rod and over the coil attaching to the baseplate at two places. The position of the coil on the inner rod was set by the Teflon winding blocks so the coils are correctly positioned when they slip into place. The PVC holders were cemented together using standard PVC cement. In addition, an external PVC weld was made along all the seams of the seal.

The wire ends from each coil exited the housing and passed down each of the plastic water tubes attached to the coils. The wire then travels about 1.5 feet down the tube where it reaches a modified 0.5" brass Swagelock union tee. The tee has a small hole that was drilled into it opposite the perpendicular port. In addition, a copper tab was silver soldered onto the side of the tee.

The wire was soft soldered into the hole with the use of a propane torch. The extra slack of magnet wire was left inside the water tube beyond the brass connector for the case of a future break due to electro-chemical etching at the connection. In this scenario, the tee could be removed and re-soldered using some of the slack wire. The inside of the tee was also covered with Cold Weld. On the outside of the brass tee, the electrical connection is made to 10 gauge wire by bolting the lug on the wire to a hole in the copper tab on the side of the tee. The copper tabs were first cleaned with sandpaper to remove oxides from the soldering process.

The coils are cooled with water. Each PVC holder has two water connectors which are attached to 1/2" plastic tubes with nylon Swagelock connectors. The water enters each holder in the lower tube and exits the top allowing air bubbles to escape. The water then either passes through the gaps in the coil formed by the nylon spacers or goes around the outside of the windings. The water is primarily prevented from going straight from the inlet to the outlet and not passing the coil by a barrier that is machined into the PVC baseplate. The process water comes from the recirculating refrigeration chiller Merlin M-33 from Neslabs which is buffered by a massive water tank. This chiller has a cooling capacity of 1250 W. The quadruple coils each have a resistance of 0.29 Ω and the Ioffe coil has 0.40 Ω. At a maximum reasonable current of 30 A, this gives powers of about 260 W in each quadruple coil and 360 W in the Ioffe coil. The chiller's positive displacement pump puts out about 6 l/min at a maximum pressure of 60 psi. When operated at this max-

imum flow, the quadruple coils individually drop about 25 psi, the Ioffe coil 15 psi, and electronics FET heatsink about 50 psi. So when run in parallel the Ioffe coil receives about 2.4 l/min, each quadruple coil about 1.44 l/min, and the FETs about 0.72 l/min and the output pressure is only 6 psi. With these flows and the outstanding thermal contact, the coils only change temperature by about 2 °C.

The decision to use PVC for the coil housings was based on leaking problems that were associated with a former design. Originally, the housings had been made out of Plexiglass and sealed with the chemical Dichloroethane. Dichloroethane melts the Plexiglass allowing two adjacent surfaces to fuse together. Those housings had a nasty tendency to develop leaks. This likely occurred due to small gaps that the Dichloroethane did not seal because of the fact that small gaps are not filled by the substance since it only fuses contacting faces and adds no material. Also, Plexiglass tends to absorb water and swell [38]. This could further weaken the seal made by the Dichloroethane and lead to leaks. This problem was temporarily remedied by using the epoxy Cold Weld. The epoxy was put on the surface of the joints and at noticeable leaks. This brought temporary relief, but eventually it gave way to a leak that was not able to be patched. With the use of PVC cement and PVC welding, the current coils were constructed and sealed. They have yet to leak or show any signs of faltering.

In addition to the primary coils of the QUIC trap, various auxiliary coils were added. These coils are shown pictorially in Figure 2.25. For each of

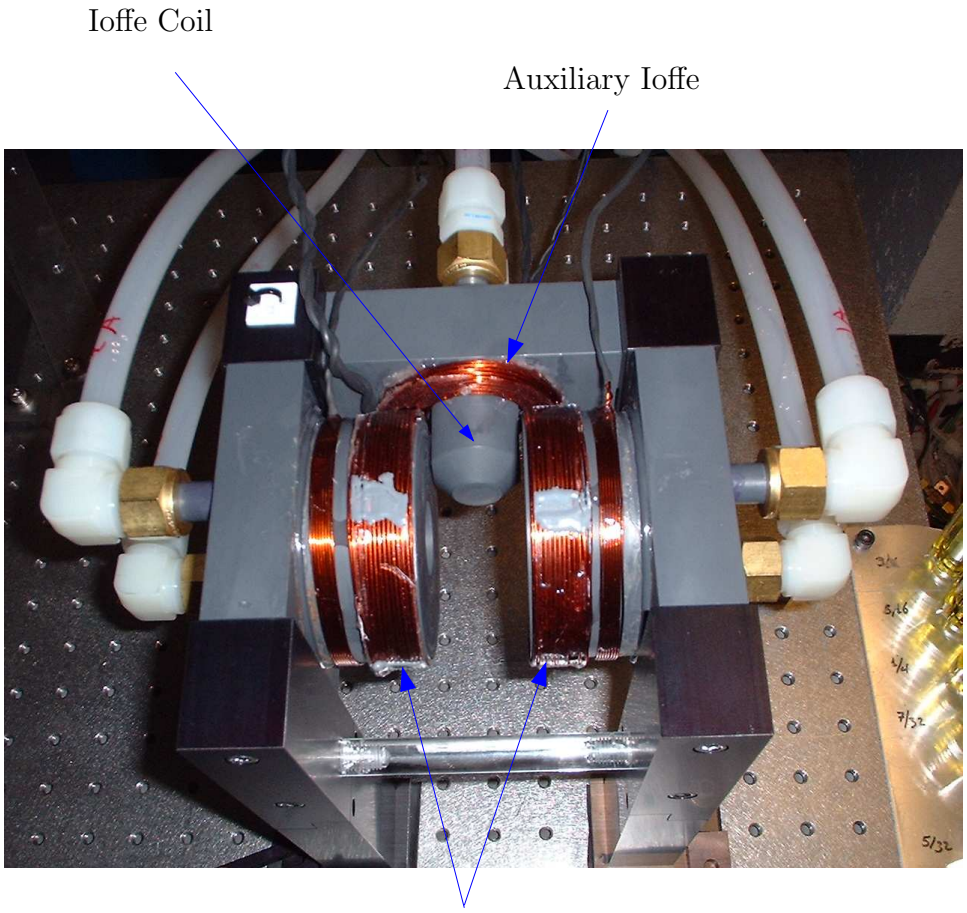

Figure 2.25: A photograph showing the coils of the QUIC trap. The Ioffe Coil, the Helmholtz pair, and the auxiliary Ioffe coil are labelled. The quadrupole coils are surrounded by the Helholtz pair.

these, the coils are self-supported with the turns attached together with epoxy. They were slipped over the PVC forms of the primary coils and are held in place by a few dabs of epoxy to the PVC. These coils are uncooled.

The first is the auxiliary Ioffe coil. This coil consists of about 40 turns of 20 gauge wire and has a resistance of about $1/4\,\Omega$. The purpose of this coil is to slightly alter the minimum field B_0. One can think about this coil as a small adjustment to the current in the actual Ioffe coil. Since the coil is uncooled, there is a limit to the current that is reasonable to put through it. The change in field minimum is approximately $\Delta B_0 \simeq (1\,\mathrm{G/A}) \cdot I_{\mathrm{IAux}}$. In practice, this coil can change B_0 by several Gauss.

The Helmholtz pair, which is mounted on the outside of the PVC holders of the main quadrupole coils, consist of 30 turns each of 16 gauge wire, and each coil has a resistance of about $0.05\,\Omega$. The pair produces a uniform field near the trap center along the arrow labelled ρ in Figure 2.25. The value of this field is about $B_{\mathrm{HH}} = (2.6\,\mathrm{G/A}) \cdot I_{\mathrm{HH}}$. Therefore, a field of $10\,\mathrm{G}$ can be obtained along the axis of the primary quadrupole coils for under a watt of power in each coil.

2.4.3 Current Driver Electronics

The power circuit for the QUIC trap consists of three current regulators and two MOSFET switches as shown in Fig. 2.26. The three current regulators are single opamp PID controllers which regulate the current based on a Hall sensor output (CLN-25 from F.W. Bell) by adjusting the analog gate

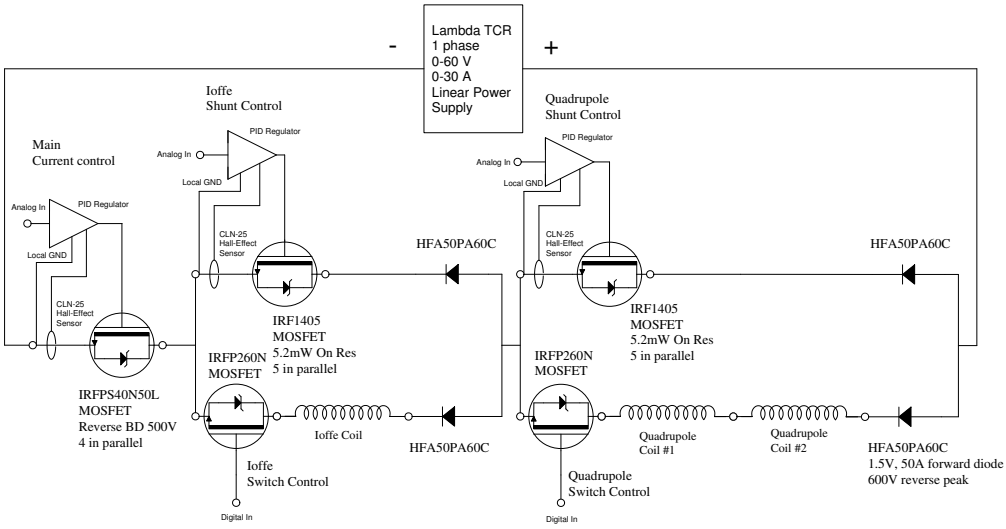

Figure 2.26: A schematic of the main power circuit that runs the magnetic trap coils.

voltage of their respective MOSFETs. These regulators are similar to those for our laser diode current controllers. The main current controller uses four IRFPS40N50L power MOSFETs from International Rectifier. These MOSFETs have a breakdown voltage of $V_{\mathrm{DSS}} = 500\,\mathrm{V}$. The two shunt regulators each use five IRF1405 power MOSFETs from International Rectifier which have a low on-resistance of $R_{\mathrm{DS(on)}} = 5.2\,\mathrm{m}\Omega$ each. This gives the FET bank an on-resistance of $1.04\,\mathrm{m}\Omega$. It is intended that this be much smaller than that of the load it shunts. These loads are about $0.5\,\Omega$ each. The MOSFET switches use a single IRFP260N. These are intended to fully shut off the a coil when it is desired and not used for regulation.

This design is flexible enough to allow various current configurations and ramps to be used, including a quadrupole trap for the MOT which is obtained with the Ioffe coil off, the QUIC trap after the Ioffe has been ramped on from the quadupole configuration, and the decompessed Ioffe trap which is at the location of the quadrupole trap. The decompressed Ioffe trap is produced by lowering the quadrupole currents and keeping the Ioffe current the same value as that used in the QUIC trap. This produces a weak symmetric Ioffe-Pritchard type trap which has moved back to a desired location at or near the quadrupole trap center. More will be said about the decompressed Ioffe trap in Chap. 5.

In the ideal operation mode for evaporation, the same current flows through all three of the QUIC trap's primary coils. In this case, only the main current regulator is operating, the two switches are wide open, and the

two shunts are totally disabled. During ramps, the analog inputs to the shunt controllers are used. This diverts current to or away from the coil. The coils may be slowly switched off or on together by using any combination of the two shunts and the main current regulator. For sudden switch off of the entire trap, the main MOSFETs are simply switched off. In this case, the main MOSFET's built-in 500 V zener voltage does the clamping for a quick linear current decay. The various forward diodes (HFA50PA60C) protect the power supply and also prevent the coils from switching through the shunt current regulator.

In constructing this circuit, there are three floating voltages which are labeled 'Local GND' in Fig. 2.26 near each regulator. At each location is a 0.5 A, $\pm$15 V power supply for the control electronics. The control signals shown are one analog input for each regulator and one digital input for each switch, which are brought in through analog and digital optocouplers. This allows for each control stage to float at any voltage along the chain and also prevents ground loops and protects our computer outputs from voltage spikes during switch off. There is also an earth ground 0.5 A, $\pm$15 V power supply for the front end of the optocouplers.

The HCNR201 analog optocoupler and the HCPL-2602 digital line receiver optocoupler, both from Agilent Technologies, were used in the circuit. The HCNR201 has an output photodetector and an identical photodetector on the input side. This allows for feedback linearization of the output with a precision opamp. This setup provides a very stable and accurate analog signal

with a bandwidth of order 100 kHz. This is far beyond the sweeps used in the experiment, which are on the order of 100 ms. This is also fast enough to be used for sudden switch off. The HCPL-2602 has a frontend that is directly driven by the input digital signal.

2.5 Control Electronics

A rather involved control system is needed for the experiment to run smoothly. The system consists of four computers running four different programs used for computer control and data acquisition. A brief description of the different elements of the system is provided below. A full description of the system as well as design notes, schematics, and construction plans for all elements of the system can be found online at Ref. [39].

Four computers are used to control and extract data from the experiment. The main control computer is a standard desktop personal computer (PC) computer running under Windows 2000. The main control program for the experiment runs from this computer. The program, *Control*, was written in Microsoft Visual C++ by Florian Schreck. The structure of the program is such that adding new experimental sequences can be done quickly and with little effort. The program has a graphical interface allowing the user to easily pick which options are to be performed as well as what the parameters for those options are. The program controls the outputs of four National Instrument cards, two digital and two analog output cards, residing in the computer.

The main data acquisition and analysis computer is also a PC running

Windows 2000. This computer runs the program *Vision* which acquires and processes images from the experiment. The program, also due to Florian Schreck, was written in Borland C++. This program communicates with the main control program, receiving experimental values and the parameters used during the experimental run. *Vision* displays the images taken by the two cameras and displays them on the monitor. The program also allows for manipulation and analysis of the data. Ideally, this computer would be directly connected to the two data taking cameras, but this was not possible. Due to limitations of the two cameras, separate computers must operate those cameras and send the data to *Vision* via TCP/IP.

One of the two computers devoted to camera interface is a Macintosh PowerMac computer running Macintosh operating system OS 8.6. It contains a NuBus card that communicates with the Princeton Instruments (PI) water cooled CCD camera. Several programs written in LabView receive the raw image, process it, and send data back to *Vision* on the main data processing computer. Attempts to upgrade this computer to a PC have failed due to the fact that it is the only computer with a NuBus card that can correctly communicate with the PI camera.

Finally, there is a PC running Windows XP that is used to interact with the Apogee Alta series air cooled CCD camera model U47+. A program written in Visual C++ interfaces with the Alta camera and sends the data to *Vision* on the main data acquisition computer. This camera is not controlled directly from the main data acquisition computer because there are no drivers

written in Borland C++ for the camera. Efforts were made to run both Borland C++ and Visual C++ on the main data acquisition computer to allow it to take the picture, but the two C++ programs would not communicate well together in such a configuration.

Specialized hardware was developed to interface the computers with the experiment. A slew of digital outputs and analog outputs are needed to turn on and off different devices as well as to control the output levels of those devices that need it. As was mentioned previously, the control computer houses five National Instrument cards providing 24 analog outputs and 32 digital outputs. Unfortunately, this does not provide enough control for the experiment, but it is impossible to add more cards to the computer due to the limited number of PCI slots in the motherboard of the computer. This problem was circumvented by designing and building an original parallel digital bus system and accompanying digital outputs and digital-to-analog outputs.

The parallel bus system consists of a parallel bus of 25 bits. Eight bits are used as an address for a 16 bit device. In addition there is one strobe bit which is used for timing. The control computer interfaces the bus system through a National Instruments NI6533 32 bit digital output board. The output of this board produces the 25 bit signals, a synchronous clock signal, and seven extraneous bits. The special National Instruments cable connects the NI board to several home built boards that buffer the NI outputs and use the synchronous clock to create the strobe bit. The output of these boards is the bus system.

The bus system is capable of accessing one 16 bit device every clock cycle labelled with one of 256 different addresses. During each clock cycle, the bus system controls either a card with 16 digital outputs or one 16 bit channel of an analog card that has eight outputs. The digital card takes the 16 data bits from the bus and uses those values to set the logic level of 16 latched and buffered digital outputs. Each of the analog cards accommodates eight buffered analog outputs. Two-four channel, 16 bit digital-to-analog converters are used on the board to convert the bus data bits into an analog signal.

The speed at which the system can operate is determined in part by the speed of the computer interface with the bus system. In addition, it is limited by the number of elements that the bus system is operating at one time. The NI cards are operated at a clock rate of 500kHz, putting an initial limit on how fast the bus can run a device. The other limit is that the bus can access only one device per clock cycle. If N devices are being updated at the same time, the updates must alternate between the N devices every N clock cycles, thus reducing the effective speed by a factor of N. Given the high initial speed of the bus, this has never been a major concern for the experiment since generally there are only a few simultaneous updates.

2.6 The Sequence

The previously described elements of the experimental apparatus are essential to the creation of a condensate. But mere descriptions of those elements do not do justice to the difficulty in producing a condensate. Therefore,

it is instructive to look at the process used to create a condensate from beginning to end starting with the collection of atoms out of a vapor.

2.6.1 Upper MOT

As previously mentioned, the upper MOT resides within the upper chamber. The pressure in the upper chamber is on the order of 10^{-7} Torr and dominated by rubidium vapor. This value is inferred from the known vapor pressure of rubidium at room temperature [19] along with the known pressure in the upper chamber of $< 10^{-9}$ Torr before the addition of rubidium into the chamber.

The upper MOT loads roughly 10^9 atoms in under half a second. Because there are no calibrated diagnostic instruments with which to measure the upper MOT, these specifications are only estimates. Two small CCD cameras, Ramsey Electronics model CCD338, are used to observe the upper MOT. An image of the upper MOT, taken with one of the survey cameras is shown in Fig. 2.27. A crude estimate of the number of atoms was generated by collecting fluorescence from the upper MOT and measuring it on a power meter. The exact number of atoms is not relevant since the experiments take place in the lower MOT.

Fig. 2.28 shows the layout of the optics used to create the upper MOT. Along the three orthogonal axes made by the six 2.75" ports, three retroreflected beams are used to create the MOT beams. The horizontal beam uses roughly half the power from one of the slave lasers. The beam has a $1/e^2$

Figure 2.27: A CCD image of the upper MOT.

waist of $\approx 8\,\mathrm{mm}$ with a power of $\approx 15\,\mathrm{mW}$. The two diagonal MOT beams are generated from the output of one slave laser. Approximately 40 mW is split with a 50% beam splitter into the two diagonal beams. Each beam has a $1/e^2$ waist of $\approx 8\,\mathrm{mm}$. The repump beam for the upper MOT is combined with the horizontal MOT beam in a 2" polarizing beam splitting cube. The beam has a $1/e^2$ waist of $\approx 8\,\mathrm{mm}$ with a power of $\approx 5\,\mathrm{mW}$.

The quadrupole magnetic field is supplied by two current loops. One loop is a coil which has a diameter of 3.2" and has 81 windings. It is situated next to the upper MOT chamber around the free horizontal beam port. The "matching" loop actually consists of two large coils with 81 windings shaped to resemble a matching 3.2" diameter coil. The reason this is done is because of the mechanical shutter, ion gauge, and ion pump that are connected to the

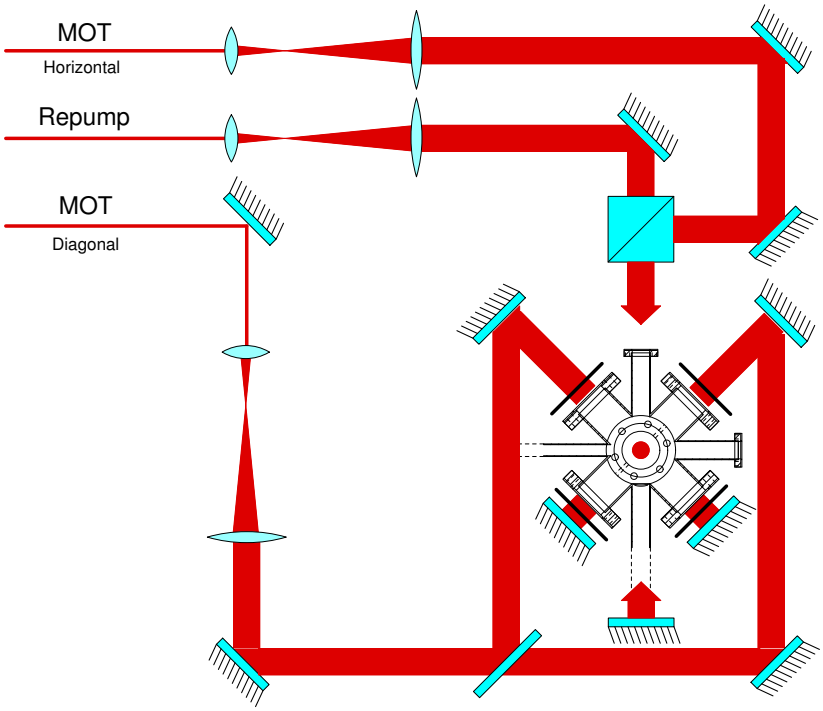

Figure 2.28: The optics layout for the upper MOT.

upper MOT chamber on the extended horizontal beam port. The two coils used to create the "matching" coil are themselves matched. Each coil has a roughly 2.5" diameter. A portion of the coil is shaped to be one half of a 3.2" diameter coil. The rest is bent at a right angle and extends away from the chamber. Together the coils make one almost seamless 3.2" diameter coil. The parts of the coils protruding away from the chamber are matched with current running in opposite directions, so that the magnetic field falls off quickly and has little effect on the quadrupole field inside the chamber. All three coils are

cooled via water cooling of their respective coil holders.

While all efforts were made to match the two coils, there still exists a slight imbalance between the two. To overcome this, the double coil is run at a slightly higher current. When loading an upper MOT the single coil is run at $\approx 2.8\,\mathrm{A}$ while the double coil is run at $\approx 3.4\,\mathrm{A}$. This creates a quadrupole field with an estimated gradient of $20\,\mathrm{G}$
rmcm. An added benefit of controlling the current in the coils separately is that it is possible to adjust the position of the upper MOT along the axis of the quadrupole coils.

2.6.2 Transfer

The transfer of atoms from the upper MOT to the lower trapping region is accomplished in a manner similar to that used by Madison et. al. [24]. A near resonant push beam is trained on the upper MOT. It continually pushes atoms from the upper MOT through the differential pumping tube to the lower chamber where the atoms are recollected in the lower MOT.

The push beam is generated from the Upper MOT Horizontal slave laser as shown in Fig. 2.13. As previously mentioned, the zeroth order of the slave laser is used to produce the push beam. The beam is designed to run concurrently with the upper MOT. The double pass in the beam path allows for tuning of the push beam, but in practice, the detuning is set to that of the upper MOT.

Before entering the chamber, the push beam is a collimated beam with

a waist of .75 mm and a power of roughly 6 mW. Approximately 10 cm before entering the upper chamber through the top 1.33" port, the beam passes through a 200 mm focal length lens. This focusses the beam to a waist of approximately 100 μm about 5 cm before hitting the atoms. The divergence of the beam is such that it has a waist of roughly 1 cm at the position of the lower MOT while not clipping on the differential pumping tube.

2.6.3 Lower MOT

Situated in the center of the glass cell in the UHV region of the vacuum chamber is a magneto-optical trap used to collect atoms transferred from the high pressure region of the chamber. The MOT consists of three pairs of mutually orthogonal counter-propagating beams. Unlike the upper MOT, the lower MOT beams are each independent.

As mentioned earlier, one slave laser produces the light for the lower MOT beams. The distribution for this laser is shown in Fig. 2.16 and described in Sec. 2.3.1. Before the lower MOT beams are created, the main beam is spatially filtered. After the spatial filter, the beam has a power of approximately 45 mW and a waist of approximately 0.75 cm. This beam is then split into six beams of approximately equal intensity. The beams are inserted into the glass cell chamber as seen in Fig. 2.29. The portion of the repump beam used for the lower MOT is spatially filtered and expanded to a waist of roughly 1.5 cm and has a power of about 5 mW. This beam is then inserted into one arm of the lower MOT beam path as shown in Fig. 2.29.

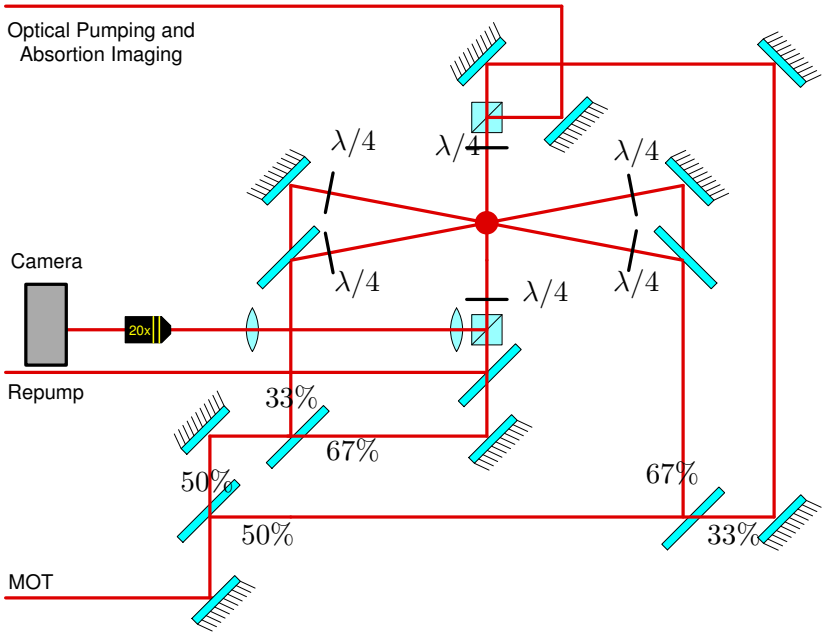

Figure 2.29: The optical setup for the lower MOT.

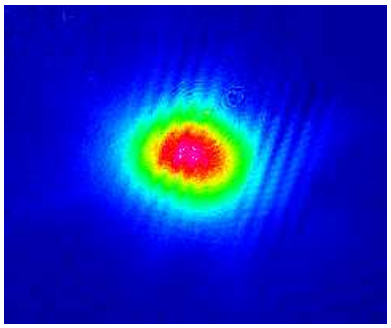

Figure 2.30: An absorption image of the lower MOT. The MOT contains $\approx 1.5 \times 10^9$ atoms. The image was taken with a probe beam detuning of 5 MHz to avoid saturating the image.

The magnetic field gradient required for the operation of the lower MOT is provided by the QUIC trap coils. In MOT operation, only the two quadrupole coils are in use. For typical loading conditions, 1.75 A of current are run through the coils. This produces a field gradient of ≈ 15 G/cm.

Atoms are loaded into the lower MOT from the upper MOT via the differential pumping tube as mentioned in Sec. 2.6.2. The initial loading rate for the lower MOT is typically on the order of 1.5×10^8 atoms per second. This rate starts to fall off after approximately three seconds as saturation effects begin. The cloud reaches a steady state number of 1.5×10^9 atoms after roughly twenty seconds of loading. Fig. 2.30 shows an absorption image (see Sec. 2.6.6 for a description of absorption imaging) of a fully loaded lower MOT. The cloud has a $1/e^2$ diameter of ≈ 2 mm. The temperature of the cloud is roughly $100 - 150\,\mu$K.

After the lower MOT has loaded, the cloud undergoes polarization gra-

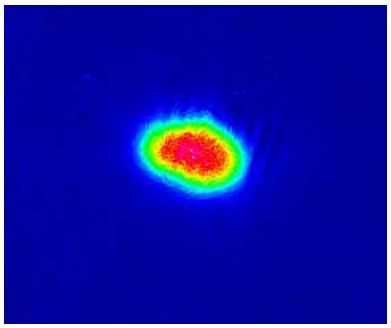

Figure 2.31: An absorption image of the lower MOT after polarization gradient cooling. The MOT contains $\approx 1.3 \times 10^9$ atoms. The image was taken with a probe beam detuning of 7 MHz in order to avoid saturating the image.

dient cooling [40, 41]. The intensity of the lower MOT beams is reduced to 50% of the loading intensity. At the same time the beams are detuned to 50 MHz red of the $F = 2 \rightarrow F' = 3$ atomic transition and the magnetic field is shut off. The atoms remain in the light for 5 ms after which they have been cooled down to a typical temperature of 25 μK with only a slight loss in atom number.

2.6.4 Optical Pumping and Transfer to the Magnetic Trap

The next step in the condensation process is optical pumping, followed by loading into a magnetic trap. The reasons for loading the atoms into a magnetic trap will become clear in the next section; this section focusses on how the atoms are put into a specific magnetic state so that they can be efficiently placed into a magnetic trap.

A review of what happens to an atom in a magnetic field is in order. In Chap. 1, it was explained that an atom behaves as a small magnetic dipole

and in a magnetic field, **B**. It feels a potential, $U_B = g_F m_F \mu_B B_z$ (see Eq. 1.5). By spatially varying the magnetic field, it is possible to build a potential that traps the atoms. The atomic magnetic moment precesses around the local magnetic field at the Larmor frequency, $\omega_L = \mu/\hbar\ B$. Viewing each atom as a magnetic dipole moment, if the external magnetic field direction changes slowly as an atom moves through space, the moment will adiabatically follow the field direction, that is $d\theta/dt \ll \omega_L$, where θ is the angle of the magnetic field with respect to some axis. The condition may also be written

$$\frac{\mathbf{v} \cdot \nabla B}{\omega_L B} \ll 1. \tag{2.8}$$

Therefore, since the magnetic trap has ∇B on the order of 250 G/cm and B at least 1 G, the above ratio is smaller than 0.01 for atomic velocities of order several hundred recoil velocities. The adiabaticity condition, therefore, applies to atoms in a magnetic trap loaded from a MOT.

For the ^{87}Rb ground state $5^2S_{1/2}$, the Landé factors are $g_{F=1} = -1/2$ and $g_{F=2} = 1/2$ [19]. This means that the states $|2, +2\rangle$, $|2, +1\rangle$, and $|1, -1\rangle$ are low field seeking states in that they will seek out a field minimum to reduce their potential energy. Since it is not possible to make a static magnetic field with a field maximum [34], traps must be made with a field minimum. Therefore atoms in low field seeking states are trappable atoms. In the case of a magnetic trap with too weak a field, as discussed above, atoms of sufficient temperature will see a trapping field that varies too quickly and may move to a different m_F state (likely an untrapped state). Such transitions are called

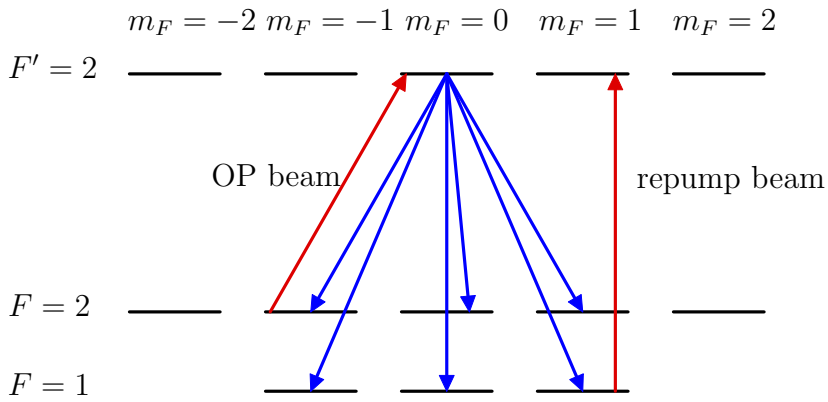

Figure 2.32: Diagram of the optical pumping scheme. Two beams are applied to the sample of atoms shown in red in the figure. The optical pumping beam (OP beam) is resonant on the $F = 2 \rightarrow F' = 2$ transition. Once in that state, the atom spontaneously decays to either the $F = 2$ or $F = 1$ ground state, shown in blue in the figure. A repump beam is needed as well to ensure that atoms that decay to the $F = 1$ are thrown back into the optical pumping cycle.

Majorana flips and result in trap loss. This is especially problematic for a trap with a field zero which results in Majorana flips for arbitrarily cold atoms.

In order to efficiently load atoms into the magnetic trap, as many of the atoms as possible must be put into a trappable state. This is accomplished through optical pumping, which is achieved by making the desired state, $|F = 2, m_F = +2\rangle$ a dark state. Fig. 2.32 illustrates the optical pumping scheme. A biasing magnetic field is applied to the atoms to define a quantization axis. At this point, a σ_+ polarized laser resonant on the $F = 2 \rightarrow F' = 2$ transition is applied to the atoms. It is important that the biasing magnetic field is not too strong so that the laser is still in resonance with all the magnetic

sublevels.

The σ_+ laser drives transitions from $|2, i\rangle$ state to the $|2, i+1\rangle$ state. Notice that since the state $|2, +2\rangle$ is a stretched state, there is no state to which it can be excited. This state is referred to as a dark state since the atoms no longer see the resonant light. Once in a dark state, atoms will remain in that state. If an atom does become excited, it will decay to one of the ground states available by selection rules with a probability determined by the Clebsch-Gordan coefficients. Since it is possible for the atoms to decay down to the $F = 1$ ground state, the repump laser is also turned on to keep atoms in the optical pumping cycle. After several cycles of excitation and decay, atoms will start to accumulate in the dark stretched state, which also happens to be the desired magnetically trappable state.

A weak magnetic bias field is needed in order to define a quantization axis. The optical pumping bias field is applied by a Helmholtz coil pair attached to the two large lower MOT quadrupole coil housings. As mentioned in Sec. 2.4.2, the two coils are driven in series creating a field on the order of several Gauss.

Two beams are required to implement optical pumping. The same repump beam on the $F = 1 \rightarrow F' = 2$ transition that is used to create the lower MOT is used for optical pumping. The optical pumping light on the $F = 2 \rightarrow F' = 2$ transition is created by the Upper MOT Diagonal slave laser as shown in Fig. 2.15. The beam is tuned to be exactly on resonance with the optical pumping transition with a power of approximately 1.5 mW. The

beam has a Gaussian profile with a waist of 15 mm that is clipped by an iris to a diameter of 19 mm. The beam is combined with one of the lower MOT horizontal beams in a polarizing beam splitting cube and enters the chamber as displayed in Fig. 2.29.

The optical pumping sequence takes 200 μs and dramatically increases the number of atoms loaded into the magnetic trap. Empirically, the number of atoms loaded into the magnetic trap is increased by slightly more than a factor of two. This increase in number comes at a small price. The repeated spontaneous emission events that make optical pumping work, heat the cloud of atoms. The amount of heating is quite small, increasing the temperature by about 5μK. This is an acceptable trade-off.

After the atoms are optically pumped into a state that can be trapped, they are loaded into the magnetic trap. As described previously, the magnetic trap consists of three coils. The two quadrupole coils create the gradient field used to load the transferred atoms into the MOT. To load into the trap, the current in those coils is ramped up followed by the ramping on of the Ioffe coil. Because the MOT coils and the magnetic trap coils are one and the same, there is no mode matching necessary in order to load atoms into the trap.

Fig. 2.33 shows a plot of the ramp on of the magnetic fields as atoms are loaded into the trap. At the end of the optical pumping sequence, the quadrupole coils are ramped on to a value of 15 A in 5 ms. Afterward, the coils are slowly ramped up to their final current of 28 A over a period of 500 ms.

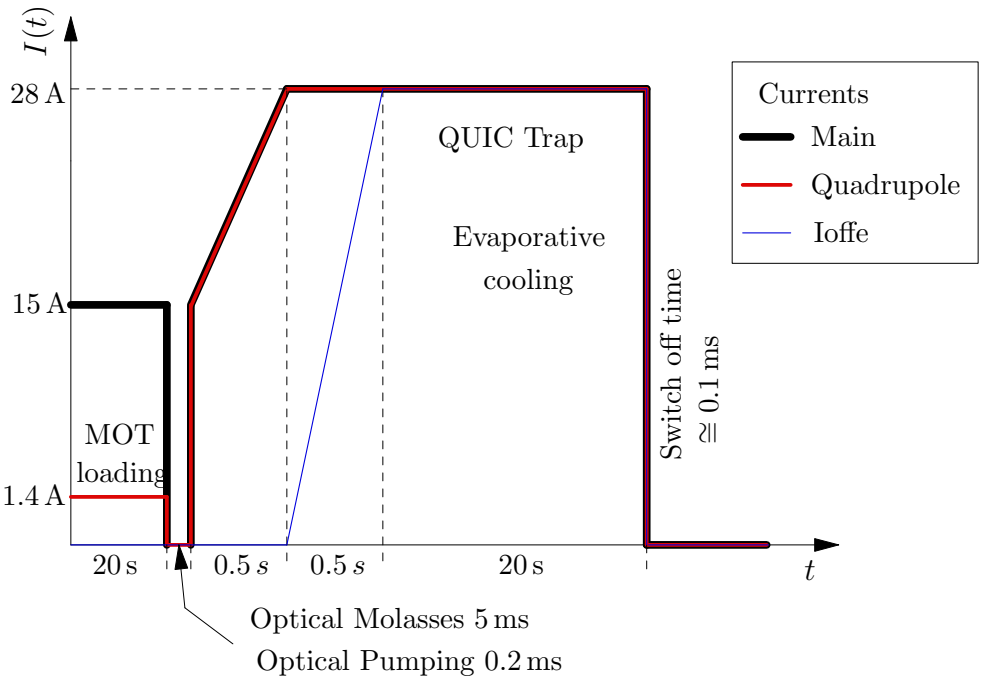

Figure 2.33: Plots showing the currents in the coils as a function of time. "Main" is the current through the main regulator. The plot shows the currents for the initial sequence down to production of BEC in the magnetic trap. The current is switched off at that point if BEC production is the end goal.

This trap is referred to as the compressed magnetic trap and Fig. 2.34 shows an image of atoms within this trap. At this point the Ioffe coil is switched on and ramped up to a current of 28A over the course of 500ms. The magnetic trap is now fully on. Fig. 2.34 shows an image of atoms in the full QUIC trap.

The current in the coils is regulated solely by the main current regulator in an effort to increase stability in the system. In this configuration, the trap center has moved by roughly 7.5 mm toward the Ioffe coil. The exact

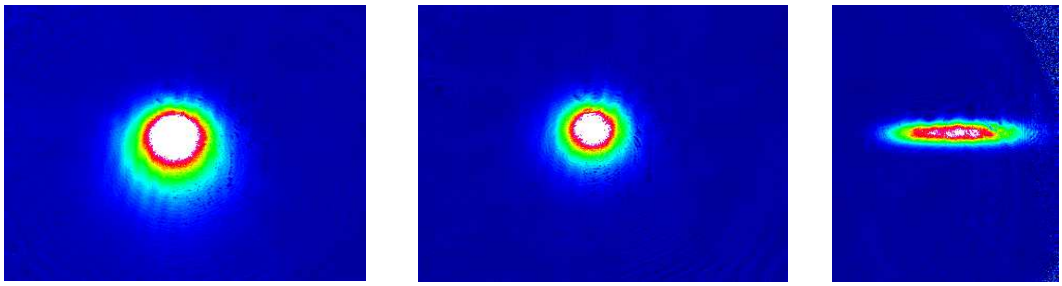

(a) (b) (c)

Figure 2.34: Images of atoms within different configurations of the magnetic trap. Image (a) shows the magnetic trap with 15 A in the two quadrupole coils. Image (b) shows the magnetic trap in the compressed trap configuration, and finally, image (c) shows the magnetic trap in the QUIC trap configuration.

displacement is difficult to determine due to limitations of the imaging system, but this is of little concern.

The magnetic trap is characterized by its trap frequencies and the magnetic field strength at the trap minimum. The trap frequencies are determined by "kicking" the cloud of atoms within the trap and observing the oscillatations. The cloud is "kicked" by offsetting the trap center slightly with a bias field, then letting the cloud evolve in the trap before taking an image. Fig. 2.35 shows the results of such a measurement. In this case, the trap frequencies are 120Hz in the strong direction and 19Hz in the weak direction. Since the trap frequencies are dependent on the trap minimum, it is important to know this value. The field minimum can be found through RF evaporation (see Sec. 2.6.5) by continuing the evaporation sweep until there are no atoms left. The frequency at which this happens corresponds to the energy offset at the bottom

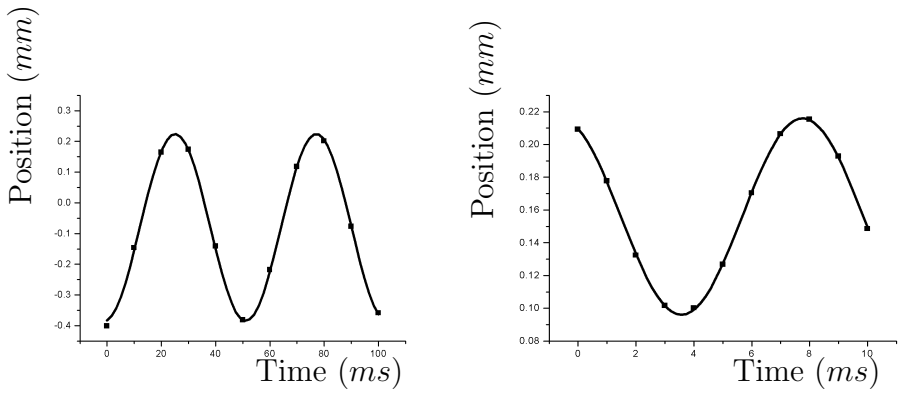

Figure 2.35: Plots showing the motion of the atomic cloud in the magnetic trap. From this measurement, it is possible to calculate the trap frequencies. The plot on the left shows oscillations along the weak axial direction corresponding to a trap frequency of 19 Hz. The plot on the right shows oscillations along the strong radial direction corresponding a trap frequency of 120 Hz.

of the trap, which can be converted into the magnetic field value at that point. In the case of the trap frequency measurements, the field minimum was 3.9 G. During typical operation, the field minimum is roughly 1.4 G (see Sec. 2.6.5). This yields trap frequencies of $\omega_{rad} = 2\pi \times 200$Hz and $\omega_{ax} = 2\pi \times 19$Hz.

2.6.5 Forced RF Evaporative Cooling

Standard laser cooling techniques are limited as to how far they can cool an atomic sample. Laser cooling operates on the principle that absorption of a resonant beam is directional, whereas the spontaneous emission of a photon from an atom is isotropic. Light fields appropriately tuned to the red of the atomic transition cause a swiftly moving atom to see the light as blue shifted

and hence in resonance. As the atom absorbs the photon, it gets a momentum kick slowing it down in that direction. This is used to cool and trap atoms with laser light.

The fact that this cooling is accomplished with discrete photon transfers leads to a limit in how far a sample can be cooled. While the spontaneously emitted photon has an isotropic radiation pattern leading to no net momentum, the square of the momentum distribution is nonzero. The atom undergoes a random walk in momentum space, leading to a spread in the width of the momentum distribution.

As mentioned earlier in Section 2.6.4, evaporative cooling is used to avoid the temperature and density limits associated with laser cooling. The particular means by which we evaporatively cool is known as forced RF evaporation. This method was first proposed and demonstrated for cooling magnetically trapped hydrogen [42]. Later, it was used to cool alkali atoms to quantum degeneracy [9–11], and is still the dominant means for achieving that goal. A thorough review of the subject can be found in Ref. [43] and Ref. [44].

There are several mathematical models that describe evaporative cooling [43, 45], but the principle can be explaine with a short example. Consider a system of N particles at temperature T_i. The energy distribution for such an ensemble of particles is given by a Maxwell distribution [46]. Now, imagine that the particles with energy greater than some value E_{cut} are removed from the group. The total energy of the group is lower, but the energy distribution of the particles is no longer thermal. To reach equilibrium again, the particles

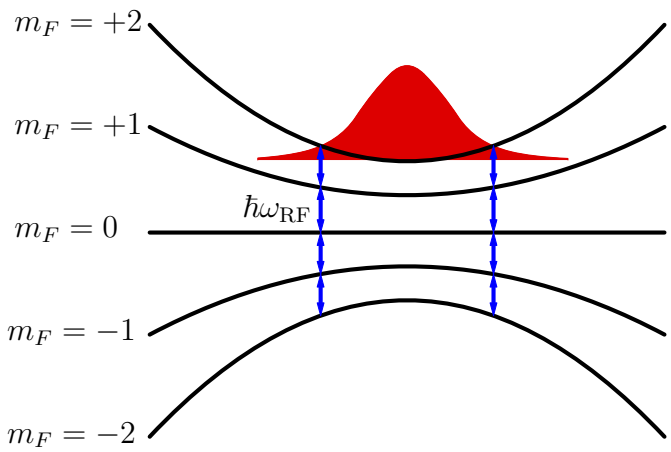

Figure 2.36: A schematic of how RF evaporation works. Each magnetic sublevel feels a different potential due to the magnetic field. Only the states $|F = 2, m_F = +2\rangle$ and $|F = 2, m_F = +1\rangle$ feel a trapping potential. Radio frequency photons create a position dependent resonance condition that forces higher energy atoms to flip their spins to untrapped states, thereby ejecting them from the trapping region.

rethermalize through elastic collisions with each other. The end product is an ensemble of particles with a lower final temperature, $T_f < T_i$.

The experimental realization of forced RF evaporation is illustrated in Fig. 2.36. As mentioned earlier, the atoms are loaded into a magnetic trap in a specific magnetic sublevel of the ground state, $|F = 2, m_F = +2\rangle$. The energy of the atom within the trap is the sum of the kinetic energy and the potential energy ($U = m_F g_F \mu_B |\mathbf{B}|$). The magnetic trap forms an anisotropic harmonic trap with a nonzero field minimum at the trap center. As an atom moves around the trap, it exchanges kinetic energy for potential energy, with

the more energetic atoms able to explore farther away from the trap center. These more energetic atoms are ejected from the trap through radio frequency (RF) spin flip transitions. The RF creates a position dependent resonance condition forming an effective energy cut in the sample. At some position, the energy difference between the different magnetic sublevels ($\Delta U = g_F \mu_B |\mathbf{B}|$) is equal to the energy of the RF photon ($E = \hbar\omega_{\mathrm{RF}}$) and atoms that reach that position will make a transition to a high field seeking magnetic sublevel. Once the atoms are in a high field seeking state, they are ejected from the trap. After some time longer than the inverse of the trap frequency, all the atoms with energy greater than the cutoff energy are removed from the trap. This is a single step evaporation process.

Forced evaporation refers to the process by which evaporation is artificially made to continue. In a single step process, the hot atoms are ejected and the cloud cools down. The number of atoms with an energy greater than the energy cut decreases, assuming that the collision rate stays constant. Therefore, the efficiency of cooling slows down and the process eventually comes to a halt. In order to force continuation of the evaporation process, the energy of the cut has to be continually reduced.

Efficient evaporative cooling relies on a constant elastic collision rate throughout the evaporative process. The elastic collision rate,

$$\Gamma_{elastic} = \overline{n}\sigma_{elastic} v \,, \tag{2.9}$$

depends on the mean density, $\overline{n}$, the scattering cross section, $\sigma_{elastic}$, and the

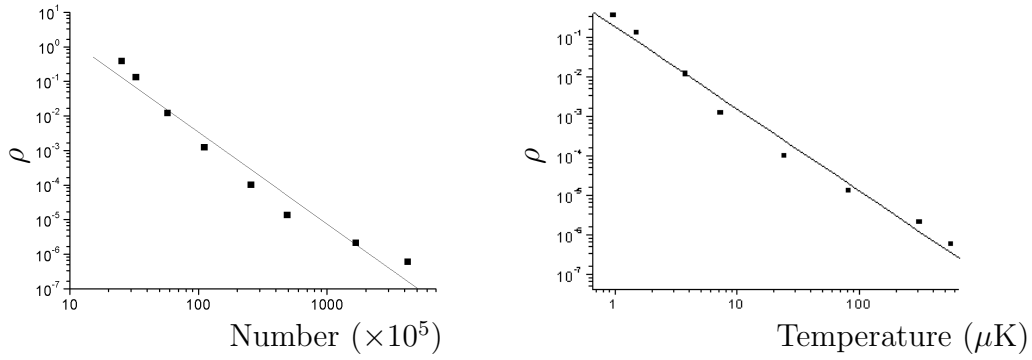

Figure 2.37: Plots of the change in phase space density, ρ, as a function of the change in atom number and the change in temperature of the cloud during evaporation.

relative velocity of the atoms, v. Since $\overline{n} \propto N/T^{3/2}$ and $v \propto T^{1/2}$, it is clear that $\Gamma_{elastic} \propto N/T$. Therefore, for evaporation to continue and not slow down, the temperature must decrease proportionally to the atom number.

The real quantity of interest here is the phase space density, ρ. A quick check shows that $\rho = n\lambda^3_{\text{deBroglie}} \propto N/T^3 \propto \Gamma_{elastic}/T^2$. By appropriately tailoring the decrease in the energy cut, it is possible to keep the elastic collision rate constant and increase the phase space density as the temperature drops. This is referred to as runaway evaporation. Fig. 2.37 shows the change in phase space density as a function of atom number as well as a function of temperature. In the experiment, the phase space increases as the inverse of temperature squared indicating that we are in the runaway evaporation regime. Fig. 2.38 shows images of atoms within the magnetic trap at various points during the evaporation process. The final result of this entire procedure

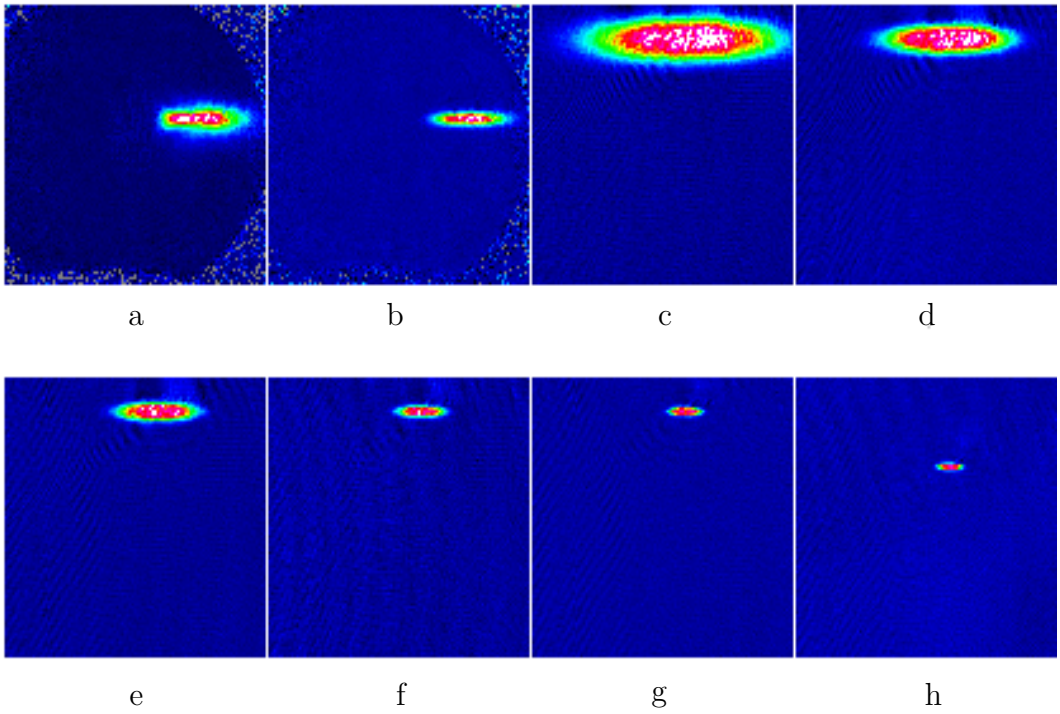

Figure 2.38: Images of the atomic cloud at various points during the evaporation sequence. Images (a) and (b) were taken with the wide angle imaging configuration while the rest of the images were taken with the close-in imaging configuration. The images were taken at the following points in the RF sweep of the evaporation sequence: (a)initial loading, (b)15 MHz, (c)5 MHz, (d)3 MHz, (e)2.1 MHz, (f)1.75 MHz, (g)1.65 MHz, (h)1.55 MHz.

is a ^{87}Rb condensate with approximately 10^6 atoms.

Within the experiment, a Stanford Research Systems function generator model SRS DS-345 is used to generate the radio frequency signal at a power level of 3 dBm. This signal is then amplified with a MiniCircuits RF amplifier model ZHL-3A with a minimum gain of 24 dB and a maximum output of 29.5 dBm. The signal is sent to a small coil located just below the

glass cell. The coil radiates the RF signal, thereby supplying the RF knife for forced evaporation. The impedance matching of the coil to the RF source was improved by a series $50\,\Omega$ resistor.

The frequency of the RF signal is ramped down exponentially. The ramp down starts at a value of 20 MHz and is ramped down to ≈ 1.4 MHz in a period of twenty seconds with a time constant of five seconds. The trap minimum can be found by evaporating until no atoms remain. Under normal operating parameters this occurs at a value of ≈ 1.2 MHz corresponding to a magnetic field offset at the trap center of 1.4 G.

2.6.6 Detection and Condensation

The primary means for analyzing the atoms is through absorption imaging. This method provides a straightforward means of determining the density profile of the cloud of atoms. Ref. [44] gives a detailed explanation of absorption imaging as well as other imaging schemes. A basic understanding can be obtained by considering a laser beam travelling through a dilute cloud of atoms. If the laser is near resonance, the atoms will scatter photons from the beam, leading to a loss in intensity. The absorption rate for this process can be described as

$$\frac{dI}{dz} = -\sigma_{eg} n I \,, \tag{2.10}$$

where

$$\sigma_{eg} = \frac{3\lambda^2}{2\pi} \frac{1}{1 + I/I_{sat} + 4(\delta/\gamma)^2} \tag{2.11}$$

is the photon-atom scattering cross section. Here, λ is the atomic transition wavelength, I_{sat} is the saturation intensity (see Appendix A), and γ is the linewidth of the atomic transition. By integrating Eq. 2.10, the absorption of the incident laser beam is found to be

$$I = I_o e^{-\sigma_{eg} \int n(x,y,z)dz} \,. \tag{2.12}$$

By measuring the profile of the incident beam, more appropriately called the probe beam, after it has passed through the cloud of atoms, it is possible to reconstruct the density profile. First, two pictures are taken of the probe beam, one without atoms, I_o, and one with atoms present, $I(x, y)$. The ratio of the two quantities,

$$A(x, y) \equiv \frac{I(x, y)}{I_o} = e^{-\sigma \int n(x,y,z)dz} \,, \tag{2.13}$$

is easily performed by a computer. This gives a flat profile with a large dimple that is proportional to the exponential of the integrated column density of the atoms. It is easier to work with the optical density,

$$D_{opt}(x, y) \equiv -\ln\left(\frac{I(x, y)}{I_o}\right) = \sigma_{eg} \int n(x, y, z)dz \,, \tag{2.14}$$

which is also trivial when solved numerically. $D_{opt}(x, y)$ gives a quantity that is directly proportional to the density of the cloud.

From this point it is possible to calculate the number of atoms that were imaged. By integrating the optical density and scaling it appropriately, the total atom number,

$$N = \int\int n(x, y)\, dxdy = \frac{1}{\sigma_{eg}} \int\int D_{opt}(x, y)\, dxdy \,, \tag{2.15}$$

is determined.

In addition, other quantities of interest can be calculated. As described earlier, the collision rate, $\Gamma_{elastic}$, is an important quantity especially in characterizing the evaporative cooling process. From Eq. 2.9, we know that $\Gamma_{elastic} = \overline{n}\sigma_{elastic}v$. The velocity of the atoms is proportional the square root of the temperature and the average density is proportional to N/V. The volume of a classical gas trapped in a harmonic potential is characterized by a $1/e^2$ width $\sigma_x = \sqrt{k_b T/m\omega_x}$. Therefore $\Gamma_{elastic} \propto N/T$. An interesting thing to note is that

$$D_{opt}(x=0,y=0) = \int n(x=0,y=0)\mathrm{dz} \propto \mathrm{N/T} \propto \Gamma_{\mathrm{elastic}}\,. \tag{2.16}$$

Simply by looking at the data images, it is possible to determine the collision rate. In Fig. 2.38, the collision rate stays constant, indicating that runaway evaporation is occurring.

Another quantity of interest is the temperature, which can be obtained in two ways. The simplest means is by taking an image of the cloud in the trap. If the trap is harmonic, the density distribution is given by the temperature of the cloud. Therefore by fitting the distribution to a Gaussian profile, the temperature is readily obtained.

Another means of discerning the temperature is through a time-of-flight measurement. By releasing the cloud from the trap, the momentum distribution of the cloud is converted into a position distribution. The resulting density distribution is a convolution of the initial distribution and the momentum dis-

tribution. If the cloud is imaged at some time τ after being released, the density distribution will be gaussian is shape with a $1/\sqrt{e}$ width given by

$$\sigma_x^2(\tau) = \sigma_x^2(0) + \frac{\sigma_p^2}{m^2}\tau^2\,, \tag{2.17}$$

where σ_p is the $1/\sqrt{e}$ width of the momentum distribution. From here the temperature is

$$T = \frac{\sigma_p^2}{mk_B}\,. \tag{2.18}$$

The experiment accommodates two orthogonal imaging systems. The origin of the horizontal probe beam is the Upper MOT Diagonal slave laser as depicted in Fig. 2.15 and described in Sec. 2.3.1. As the beam makes its way to the lower MOT chamber, it is tuned to resonance with a power of 5.0 mW. The beam profile is Gaussian with a diameter of roughly 30 mm that has been clipped with an iris to a diameter of 19 mm. It enters the chamber as shown in Fig. 2.29. It is combined with one of the horizontal lower MOT beams with the use of a 1" polarizing beam splitting cube. It then passes through the chamber, is absorbed by the atoms and exits the chamber. Upon leaving the chamber, the imaging beam is extracted from the MOT beam by another 1" polarizing beam splitting cube. After the cube, the beam is transported using two 120 mm focal length achromatic lenses. The image formed after this transport system is magnified using an interchangeable lens system. From there the beam is directed to the camera, a Princeton Instruments CCD camera model TE/CCD-5122TK/1UV. The CCD chip has a 512×512 array of 20 μm

pixels. The interchangeable lenses consist of a 38.1 mm focal length lens and a 4× objective leading to magnifications of .67× and 3.33× respectively.

In addition to the horizontal imaging system, there is a vertical imaging system. The vertical probe beam is created from the Upper MOT Horizontal slave laser as shown in Fig. 2.13 and described in Sec. 2.3.1. Similar to the horizontal imaging system, this beam is tuned to resonance with a power of 3.5 mW. The beam is combined with the push beam using a 1/2" polarizing beam splitting cube and enters the chamber from the same port. The beam passes through the upper chamber, the differential pumping tube, and the middle chamber before reaching the atoms. The beam is not collimated but rather focusses before the differential pumping tube then expands afterward to reach a diameter of roughly 15 mm at the atoms. After interacting with the atoms, the beam exits the chamber and is transported via additional optics to the Apogee Alta series U47+ CCD camera with a resolution of 1024 × 1024 pixels. The image is formed on the CCD with a 38.1 mm focal length lens, giving a magnification of 4.33×.

An additional feature of the vertical imaging system is that it is capable of making fluorescence images. By counting the number of photons, the atom number can be determined according to

$$N_{atoms} = \frac{8\pi \left[1 + 4(\Delta/\Gamma)^2 + (6I_0/I_{sat})\right]}{\gamma(6I_0/I_{sat})t_{exp}\eta_{count}d\Omega} N_{counts}\,, \tag{2.19}$$

where Δ is the detuning from the atomic transition, γ is the natural linewidth of that transition, I_0 is the intensity of one of the MOT beams, I_{sat} is the

saturation intensity, t_{exp} is the exposure time, η is the quantum efficiency of the camera, N_{counts} is the integrated number of counts on the CCD, and $d\Omega$ is the solid collection angle of the camera [18].

Additional analysis needs to be done on the images to verify that the cloud of atoms is a condensate, as absorption images of condensates are similar to any dense cloud. One method is to determine directly from the density profile of the cloud. When the cloud condenses, its density profile changes. A thermal cloud of atoms within a harmonic trap has a density distribution that is Gaussian. On the other hand, due to the mean field repulsion of the condensate, its profile is extended and matches that of the potential, a parabola (see Appendix B). A bi-modal density profile with a large parabolic central distribution and Gaussian wings is a clear sign of a condensate.

Another means of determining if the cloud is a condensate is observation of the cloud after a time of flight expansion. For a thermal cloud of atoms, the momentum distribution in a harmonic trap is Gaussian. Once released from the trap, the cloud spreads equally in all directions. The fully expanded cloud density will reflect the symmetric Gaussian momentum distribution by forming an isotropic cloud, providing that the expansion time is long enough such that the initial anisotropy is much smaller than the final cloud size. On the other hand, condensates behave differently. Others have shown that the density profile remains the same as the cloud expands, but that the mean field interaction changes the rate of expansion for the different dimensions according

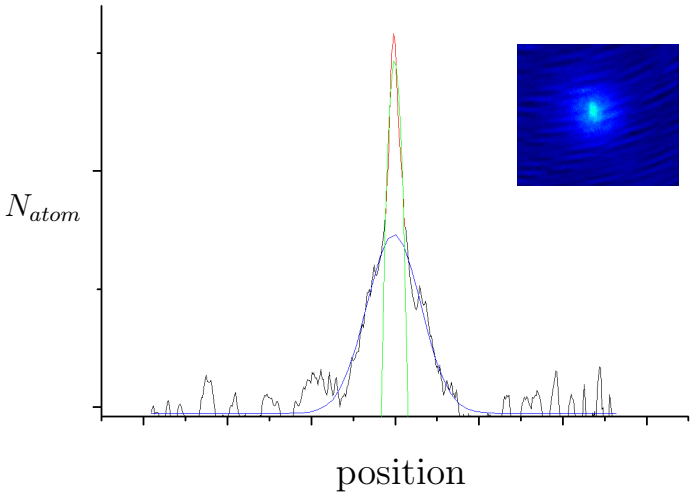

Figure 2.39: The bimodal distribution of a condensate. The inset image is a cloud of atoms with both a condensate and a thermal part. The plot is a profile of the density along one direction. The black and red lines are the raw data. The red line is the condensate and the black line is the thermal cloud. The green line is a parabolic fit to the condensate data, and the blue line is a Gaussian fit to the thermal data.

to

$$R_{radial}(t) = R_{radial}(0)\sqrt{1+\tau^2}, \quad (2.20)$$

$$R_{axial}(t) = R_{axial}(0)\left(1+\lambda^2\left[\tau\tan^{-1}(\tau t) - \ln(\sqrt{1+\tau^2})\right]\right). \quad (2.21)$$

where R_{radial} and R_{axial} are the condensate radii (see Appendix B), $\tau = \omega_{rad}t$ is the time of expansion scaled by the tight trap frequency, and $\lambda = \omega_{axial}/\omega_{rad}$ is the ratio of the two trap frequencies [10, 47, 48]. The tighter confined directions have a higher mean field energy which translates to a higher kinetic energy in those directions once the trap is turned off. Originally the cloud is cigar shaped in the anisotropic trap with the cloud thinner in the high frequency directions. After expanding for some time, the anisotropy changes orientation as the cloud is thinner in the weak trapping direction. This provides a clear signature of condensation. Fig. 2.40 shows an image of a condensate after expansion. The asymmetry of the cloud is a clear signature of condensation.

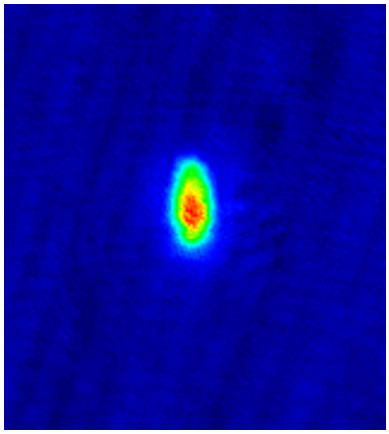

Figure 2.40: A Bose-Einstein condensate of ^{87}Rb. This image of a condensate with 8×10^5 atoms was taken 18 ms after being released from the magnetic trap. The asymmetry results from the asymmetry in the magnetic trap and is a clear sign of condensation.

Chapter 3

Atomic Billiards

3.1 Overview

The billiard is the simplest two-dimensional, time-independent system that exhibits non-trivial dynamics. It consists of a two-dimensional, flat potential region bounded by an infinitely sharp, infinitely high barrier enclosing a freely moving point particle which undergoes elastic collisions with the barrier walls. Despite the simplicity of the system, billiards can exhibit all forms of classical behavior, from simple integrable motion to chaotic motion. This vast array of dynamics is determined solely by the shape of the boundary [49]. With a circular boundary, the motion is very regular. However, if the circle is stretched infinitesimally in one direction, it will turn into a Bunimovich stadium. This system exhibits hard chaos with no stable trajectories [50].

Because of the simplicity of the system and the richness of the dynamics, billiards are an ideal testing ground for chaotic dynamics. Billiards ranging in shape from stadiums [50] to wedges [51] have been studied theoretically. Numerical simulations of billiards have been used to study problems in statistical mechanics[52, 53], and they have been experimentally studied in the context of quantum dots [54, 55] and microwave cavities [56–58].

Recently, our group[59] and another[60] have used the tools of atomic physics to study billiards. In these systems, cold atoms act as the point masses, moving within a billiard formed by light potentials. An advantage of this setup is the ease of creating arbitrary billiard shapes as well as the capability to create dynamic boundaries. In addition, cold atoms can be manipulated by adding controlled amounts of noise and dissipation. Also, by appropriately scaling the size of the billiard with respect to the de Broglie wavelength of the atoms, the system can be used to study either classical or quantum dynamics, as well as the transition between the two regimes.

3.2 The Wedge Billiard

The gravitational wedge billiard differs slightly from the traditional concept of a billiard in that a constant force, gravity, is applied in one direction. It is constructed of two straight barriers oriented at an angle θ with respect to gravity (See Fig 3.1). A particle of mass m within the billiard falls under gravity until it hits one of the walls, at which point it undergoes an elastic collision. It continues to move under the influence of gravity until it makes contact with the wall it just impinged upon or it hits the opposite wall. There is assumed to be no dissipation within the system, therefore this process continues *ad infinitum*. The top is open, but particles are still trapped within the region due to gravity.

The wedge billiard has been the focus of much theoretical work [51, 61–63]. Aside from being interesting in its own right, the wedge billiard model is

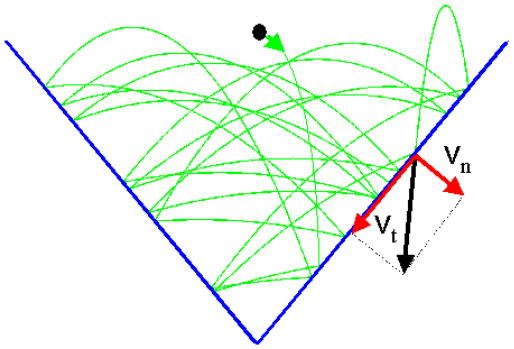

Figure 3.1: The gravitational wedge billiard. A particle of mass m, moving ballistically, undergoes collisions with the walls of the billiard that are at an angle θ with respect to gravity. The wedge has an angle of 2θ. The velocity at the point of impact can be resolved into components that are normal and tangential to the wall as shown.

relevant to other problems. It has been shown [51] that the wedge billiard is a reduction of the one-dimensional, three body, self-gravitating system.

The phase space trajectories of particles moving within the billiard provide a useful means to study the dynamics of the system. Since the billiard is a two-dimensional system, it has a four-dimensional phase space. Four dimensional spaces are difficult to visualize, so it is convenient to project the phase space onto a two-dimensional surface of section. As the energy is a constant of the motion and the particle will always make contact with the billiard walls, a two-dimensional Poincaré surface of section can be created.

The wedge potential homogeneity yields useful scaling properties. The potential is homogenous in that $V(\lambda x, \lambda y) = \lambda V(x, y)$[63]. As a result, a wedge of some angle θ looks the same regardless of whether it is 2 mm or 2 m in size.

This homogeneity allows trajectories to be scaled from one energy to another. Hereafter all trajectories will have a scaled energy of $E = 1$ for simplicity.

As a particle moves ballistically between elastic collisions with the walls, it is relatively easy to track its dynamics. Looking at the velocity of the particle immediately before the collision with the wall, it is possible to create a mapping so that a known velocity at one bounce will yield the velocity at the next bounce. Lehtihet and Miller derived the following map for the wedge billiard[51]. The map T_A

$$v_t^{i+1} = v_t^i - 2cot\theta|v_n^i| \tag{3.1}$$

$$(v_n^{i+1})^2 = (v_t^i)^2 \tag{3.2}$$

and the map T_B

$$v_t^{i+1} = (|v_n^i| - |v_n^{i+1}|)\cot\theta - v_t^i \tag{3.3}$$

$$(v_n^{i+1})^2 = 4\sin^2\theta - (v_n^i)^2 + 2\cos(2\theta)\left(v_t^i \sin\theta - v_n^i \cos\theta\right) \tag{3.4}$$

where v_t is the tangential component of velocity and v_n is the normal component of velocity (see Fig. 3.1) and the superscript refers to the bounce number, represent the two possible bouncing actions. T_A applies to the situation when the particle collides with the same wall as the previous bounce, while T_B is used when the particle hits the opposite wall. The condition

$$(v_t - 2\cot\theta v_n)^2 + v_n^2 \leq 1 \tag{3.5}$$

determines which map is used.

At this point is helpful to examine the structure of the surface of section. The coordinates v_n^2 and v_t were chosen to guarantee that the map is area-preserving [62]. The choice of coordinates and energy scale determines the shape of the phase space portrait (see Fig. 3.2). The boundary of the portrait is an inverted parabola such that $v_{\mathrm{n}}^2+v_{\mathrm{t}}^2 = 1$. The lower boundary corresponds to the particle having zero velocity normal to the wall at the time of collision. At the origin, this corresponds to a particle resting at the vertex, or sliding down the side of the billiard wall when the point is away from the center. The upper boundary represents the vertex of the wedge. Points along the upper boundary have the maximum tangential and normal velocity components which occurs only at the vertex. In Fig. 3.2, the red curve is a set of points that will be mapped to the upper boundary. Points above this curve are trajectories that have adequate v_n to travel to the opposite side of the wedge, whereas points below the curve will remain on the same side. This curve is the dividing line between points mapped with T_B or T_A, in other words, a mapping of Eq.3.5.

With some initial condition and the resulting points generated by T_A and T_B, a trajectory of the particle in phase space can be plotted, giving insights on the dynamics of the particle. Fig. 3.3 is one example of such a phase space, but with a collection of initial conditions. Some physical trajectories within the wedge are plotted for two of the initial conditions represented in the diagram.

As Fig. 3.3 demonstrates, a variety of dynamics can occur within the billiard. At the center of the portrait, marked by the black dot, the dominant

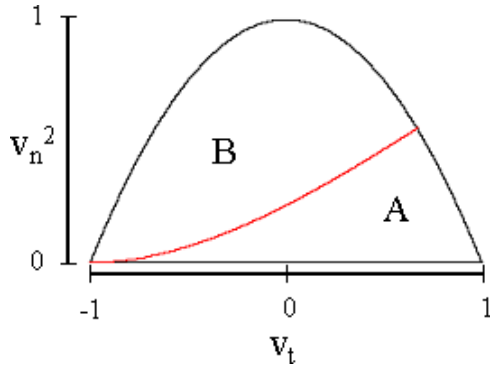

Figure 3.2: Partitions of the wedge map. The red curve denotes the condition separating the two types of bounces. Points in region A use map T_A while points in region B use map T_B.

fixed orbit is plotted. For all wedge angles there exists a trajectory such that the particle strikes one wall with zero tangential velocity, and travels to the opposite wall striking it with zero tangential velocity and identical normal velocity. This process repeats indefinitely. The physical path is symmetric about a vertical line originating at the vertex. While all wedge angles have a dominant orbit, the stability of that orbit depends strongly on the angle [51].

Away from the fixed point, other stable trajectories may be found. Each color represents a unique initial condition. The colored bands surrounding the fixed point in Fig. 3.3 represent stable trajectories. An example of a physical trajectory with quasi-periodic properties is also displayed. The particle bounces between the two walls within a well defined region of the billiard. Over time the particle collision points sample only that region within the wedge.

The other interesting behavior that is evident from the phase space portrait is chaotic motion. Surrounding the stable trajectories, there exists

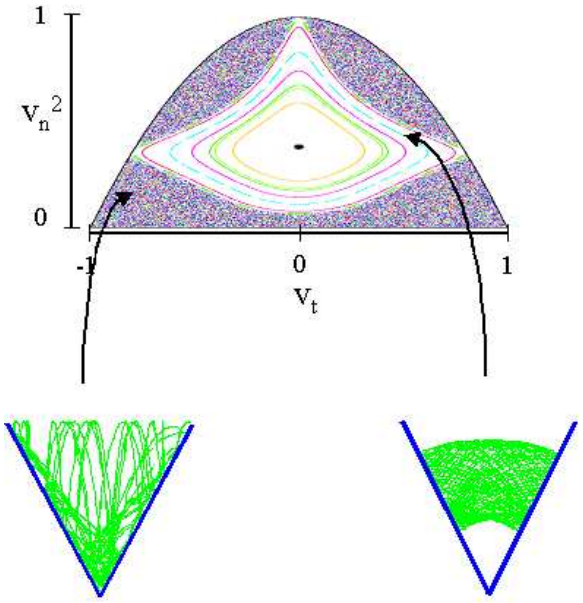

Figure 3.3: A surface of section for a $2\theta = 53^o$ angle wedge. Each color corresponds to one initial condition. Sample trajectories for two separate initial conditions are shown below the map. The trajectory on the left corresponds to a particle within the "chaotic sea." The trajectory on the right is a particle within an island of stability.

a region of "random" trajectories that appear to jump from point to point with no obvious pattern as seen in Fig. 3.3. A trajectory starting out in this "chaotic sea" will undergo ergodic mixing with trajectories of other particles in the "sea". The singularity of the vertex brings about this behavior [63]. The physical trajectory samples the entire wedge surface and will come arbitrarily close to the vertex. The importance of this will become apparent later.

The structure of the wedge phase space depends strongly on the angle of the wedge. Fig. 3.4 is a gallery of phase space portraits for various wedge angles, from which interesting patterns emerge for wedge angles between 0^o

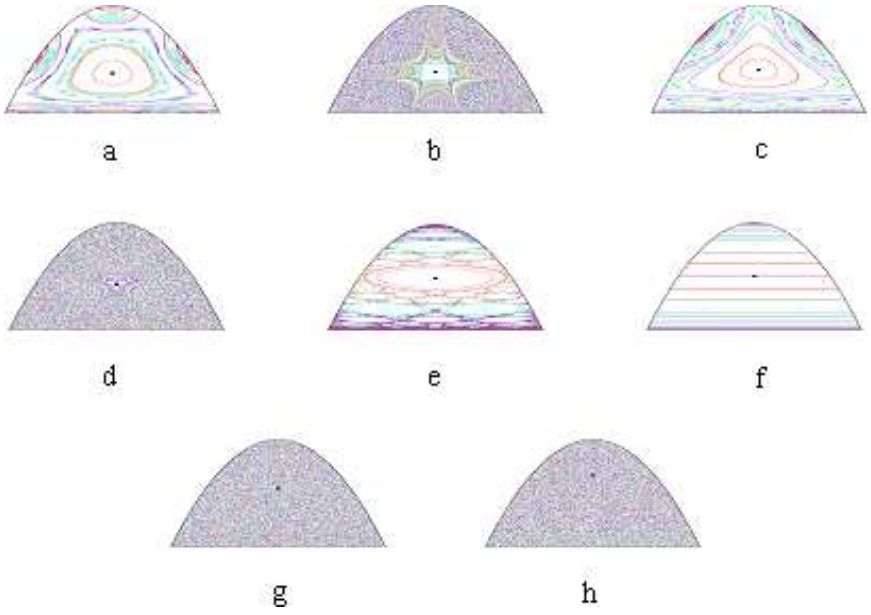

Figure 3.4: Phase space portraits for different wedge angles. θ = a) 22.5° b) 25.8° c) 30° d) 34.5° e) 44° f) 45° g) 50° h) 60°

and 45°. The phase space is mixed, as numerical studies have shown [51, 61, 63]. The ratio of chaotic to stable motion oscillates with the wedge angle, giving rise to what is known as a "breathing chaos" [61]. Wedge angles of $90°/(n+1)$, where n is a whole number, are distinct minima of this ratio. Similarly, there are certain catastrophic angles, namely 25.91° and 34.26°, which have a completely chaotic phase space. For all wedge angles greater than 45°, the phase space turns completely chaotic.

3.3 Experimental Techniques

In order to perform an experimental study of this system, a billiard is needed as well as a particle to bounce around inside the billiard. The tools

of atomic physics can provide these ingredients. Light potentials created by lasers can be used to form billiards of arbitrary shape. Laser cooled atoms are a ready source of particles to bounce around a billiard.

The goal of the experiment was to observe changes in the dynamics of the particle within the billiard by varying the wedge angle. As was mentioned earlier, the portions of the wedge that are sampled by an atom depends on kind of trajectory. If an atom happens to be in a chaotic trajectory, it will sample the entire wedge including the vertex. On the other hand, an atom in a stable periodic orbit, will only sample a limited portion of the wedge that will not include the vertex. With this in mind, a relative measure of the amount of stable orbits can be made. By poking a hole in the bottom of the wedge and waiting for a prescribed amount of time, the atoms with chaotic trajectories will drain out leaving the atoms with stable trajectories behind. By measuring the number of atoms left in the wedge after a given time, otherwise known as the survival probability, it is possible to see the ratio of chaotic to non-chaotic trajectories. This ratio can be compared for different wedge angles.

A necessary ingredient of the billiard system is the point like mass that bounces within the billiard. This role is filled by ultracold cesium atoms. The experimental sequence begins by loading $\approx 10^6$ atoms into a magneto-optical trap (MOT) [3]. The atoms are then subjected to a round of polarization gradient cooling. The resulting cloud of atoms has a gaussian spatial profile with a radius 0.2 mm and a temperature of $\approx 10\,\mu$K, which corresponds to a momentum distribution with width $\sigma_p = 7\,\hbar k$. A description of the experimental

apparatus can be found elsewhere[18, 21, 22].

By using a focused laser beam, a conservative gaussian trap of arbitrary size down to the diffraction limit and arbitrary depth up to the limits of the laser's output can be created (see AppendixA). By moving the beam any billiard configuration can be created. As shown in Fig. 3.5 any shape can be drawn by synchronously deflecting the beam along two orthogonal axes [64]. This allows us to create designer billiard potentials in the direction perpendicular to the optical axis of propagation.

A home-built Titanium:Sapphire (Ti:Sapph) laser provided the optical potential used to create the billiard wall. The Ti:Sapph laser was pumped by a Coherent I90 Argon Ion laser. With ≈ 8 watts of pump power, the Ti:Sapph produced roughly 600 mW of light at $\approx 850\,\text{nm}$. Within the cavity of the laser, there were several devices to ensure single mode operation including a birefringent filter, an optical diode, and an intracavity assembly from Coherent Laser Group. The measured linewidth of the laser is 10 MHz [18], although this is an upper bound due to the measurement technique. Further information on this laser, including its history, design and construction can be found elsewhere [18, 21].

The beam from the Ti:Sapph was used for a variety of experiments. Hence, the beam passed through several acousto-optic modulators (AOM's) used to divert a portion of the beam off to other experiments. One such 80 MHz AOM was used to pick off the billiard experiment's allotment of the beam. From there it was sent to the billiard imaging system.

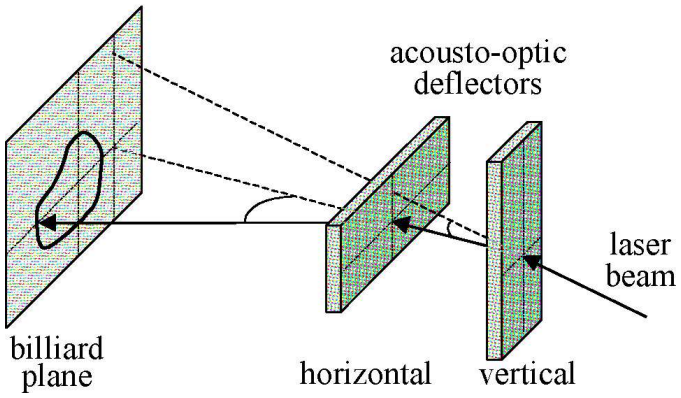

Figure 3.5: Two AODs mounted orthogonally to each other. By synchronously scanning the two deflectors, arbitrary shapes can be drawn.

To produce the shape of the billiard, the laser beam was scanned using an acousto-optic deflector (AOD) from Isomet, model 1205C-2-804B. The resonant circuit of the deflector has a bandwidth of 40 MHz with a center frequency of 80 MHz. This provides an angular deflection of 18.3 ± 4.6mrad for the first order diffracted beam at the center frequency. The deflector has a lead molybdate crystal with a 6 mm aperture, although the beam size was limited to ≈ 1 mm. This decreased the access time, T_{access}, of the deflector to $\approx 0.3\,\mu$s, where the access time is the time it takes an acoustic wave to transverse the beam. The figure of merit for a scanner is the number of resolvable spots (NRS). The NRS is computed from the time bandwidth product

$$NRS = \Delta f \times T_{access} \tag{3.6}$$

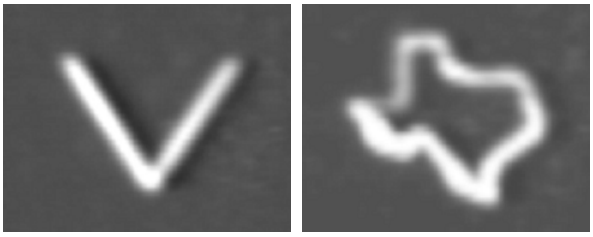

Figure 3.6: Examples of different shapes achievable using the scanning AOD method. The CCD image on the left is a wedge similar to the ones used in the experiment. The CCD image on the right is that of the state of Texas used as a test for the AODs.

where Δf is the bandwidth of the deflector [65]. The reduction in access time reduced the NRS from the specified 66 down to approximately 10.

The AOD's are controlled with drivers supplied by IntraAction Corp., model DE-802M26. The drivers are equipped with modulation inputs for frequency and power as well as a digital shut off switch. The drivers are capable of delivering up to 2W of RF power within a 60 MHz to 100 MHz frequency range. A peak diffraction efficiency of 85% at the center frequency was achieved with approximately 95% of the available power. The diffraction efficiency is a function of frequency, therefore the measured transfer function of the deflectors was used to modulate the RF power to ensure a flat response across the scanning range.

In order to make two-dimensional shapes, two AOD's were oriented along orthogonal directions as shown in Fig. 3.5. In this configuration, drawings on a 10 by 10 grid with a resolution of one grid square were possible, where a grid space is one spot size. While that resolution is by no means

ideal, it was possible to create billiards like those shown in Fig. 3.6.

The optical system shown in Fig. 3.7 was used to image the billiard on the cloud of atoms. A collimated beam from the Ti:Sapph laser passes through two orthogonal AOD's. From there, the deflected beam draws the shape of the billiard on the first lens. Since the beam is collimated, a tightly focused image of the billiard is created at the focal length of the first lens. Preceding the image, a short focal length lens on a translation stage is used to appropriately magnify the image. The typical magnification used was roughly 1/4. This image was directly transported to the chamber by a 1 to 1 telescope. The imaging system produced billiards with a $1/e^2$ wall thickness of 56μm and a total billiard size of up to $500\,\mu$m. These were verified by a knife-edge measurement as well as by a CCD image measurement.

In order to confine the atoms to the billiard plane, a standing wave was superimposed on the billiard beams (See Appendix A). The standing wave creates a series of vertical wells along the optical axis of the billiard beams. These wells provide confinement in the optical axis direction and free movement in the two orthogonal directions. Based on the initial size of the cloud of atoms, this created a series of approximately 1000 two-dimensional billiard systems.

The standing wave was created from the first order of an AOM before the billiard AODs. The polarization of this beam was rotated to be orthogonal to that of the billiard beam. A lens was matched to the final lens in the billiard set up to create a large collimated beam entering the chamber with a

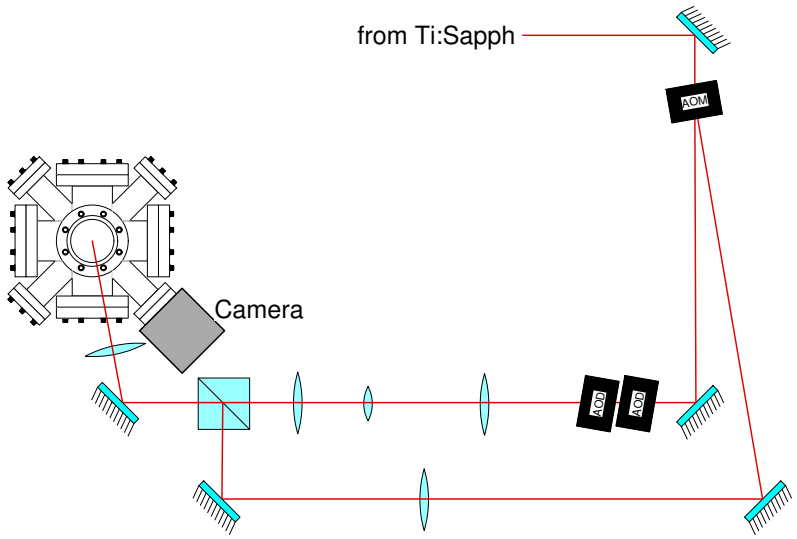

Figure 3.7: Layout of the optical setup for the billiards experiment. The beam from the Ti:Sapph laser is split by an AOM. The zeroth order beam is sent to the imaging system to create the billiard. The first order beam is used to create the standing wave. The two beams are combined in a polarizing beam-splitting cube and sent into the vacuum chamber.

$1/e^2$ diameter of 2.6 mm. On the other side of the chamber where the beams exited, a polarizing beam splitting cube and a mirror were positioned so that the billiard beam was directed to a beam dump and the standing wave beam was retro-reflected to create the standing wave.

The measurement of the atoms within the billiards was accomplished with a CCD camera, Princeton Instruments model TE/CCD-5122TK/1UV. The CCD chip has a 512×512 array of 20 μm pixels. Attached to the camera is a Nikon 105 mm f/2.8 D macro lens. The camera was mounted such that it had a view into the chamber via a small 2.75" port, which was at a 33^o angle

to the billiard beam's optical axis.

The atom number was measured by collecting the fluorescence of the atoms. By turning off all magnetic and optical fields, and turning on the MOT beams, an optical molasses was created. The atoms were held in this optical molasses for 50 ms while their spontaneously emitted photons were collected by the CCD camera. The atoms will move during the exposure time, but this does not affect the measurement of atom number. Since we are only concerned with atom number and not any spatial features, this is not a problem. By counting the number of photons, the atom number can be determined according to [18]

$$N_{atoms} = \frac{8\pi \left[1 + 4(\Delta/\Gamma)^2 + (6I_0/I_{sat})\right]}{\Gamma(6I_0/I_{sat})t_{exp}\eta_{count}d\Omega} N_{counts} \tag{3.7}$$

where Δ is the detuning from the atomic transition, Γ is the natural linewidth of that transition, I_0 is the intensity of one of the MOT beams, I_{sat} is the saturation intensity, t_{exp} is the exposure time, η is the quantum efficiency of the camera, N_{counts} is the integrated number of counts on the CCD, and $d\Omega$ is the solid collection angle of the camera.

The billiard had different sizes compared to the cloud of atoms depending on the angle of the wedge. The varying sizes led to different loading efficiencies. Therefore, the fluorescence from the surviving atoms had to be normalized against the loading efficiencies. For each wedge angle, a fluorescence image of the atoms in the wedge with no hole was made 25 ms after loading the billiard. This was sufficient time to allow those atoms that were not loaded to fall away from the billiard. This gave a measure of the loading

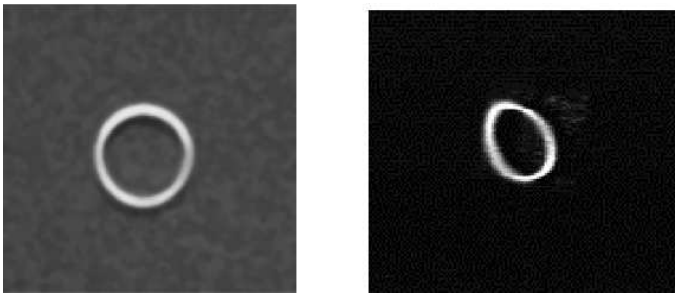

Figure 3.8: Two CCD images of a circular billiard. On the left, the deflectors are scanned at 10 kHz. On the right, the deflectors are scanned at 100 kHz.

efficiency and was used to normalize the results of the survival probability measurement.

The experimental sequence was initiated by collecting a cloud of cold cesium atoms in a MOT. The billiard with a hole in the bottom was turned on while at the same time the MOT was turned off, dropping the atoms into the billiard. The atoms were left to bounce around in the billiard for fixed lengths of time, allowing the atoms with chaotic trajectories to escape while the atoms with stable trajectories remained behind. The billiard was then turned off just as the freezing molasses was turned on, at which point the CCD camera collected the fluorescence of the atoms.

Before the experiment could take place, several issues had to be addressed. The scanning rate of the AOD's is a concern for the experiment. Ideally the deflector should be scanned as fast as possible in order for the atoms to experience a time-averaged potential. If the beam scans too slowly, the atoms will move into the beam path and be kicked during the following scan cycle, or worse yet, travel completely through the beam path and escape

the trap. The problem is that there is a limit to the scanning speed of a deflector. Since the NRS depends on the access time, the scan speed is limited by the access time[65]. In other words, in order to keep the same resolution, the scan must be slower than T_{access} otherwise the acoustic wave will change before it has crossed the optical beam. Faster scanning will cause lensing effects within the crystal, reducing the resolution. In the case of nonlinear scans, which are needed for arbitrary shapes, the situation is much worse [66]. As can be seen in Fig. 3.8, increasing the speed of the scan above a certain level will distort the shape of the billiard. It was found that around 80 kHz, the shape of the billiard started to deteriorate, while below 1 kHz atoms leaked out of the trap. Above 5 kHz, there was no noticeable effect on the atoms. In the experiment, the deflectors were scanned at 20 kHz to stay clear of either extreme.

Another issue to contend with is that the walls of the billiard are not infinitely hard. The wall profile is gaussian in nature rather than a step function. This allows the atoms to travel into the walls before being reflected. This softness has an effect on the dynamics. As seen in Fig. 3.9, the billiard appears to have a smaller angle than it actually does. Fig. 3.9 shows particle turning points on the billiard wall from a simulation where the gaussian profile of the walls was taken into account. As can be seen, toward the bottom of the wedge, the particles turn near the top of the wall, but closer to the top, the particles do not penetrate as far into the wall profile.

This effect is due to the fact that the particles are moving slower at the top of the billiard. When the particle is near the top of the billiard, most of its

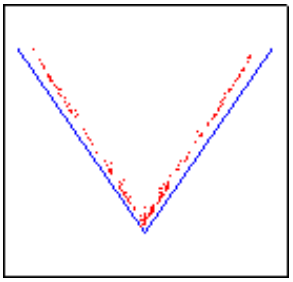

Figure 3.9: The effect of soft walls on the wedge billiard. The blue line represents the peak of the billiard potential. The red dots show the turning points for a particle bouncing off the wedge.

energy is in the form of potential energy, as opposed to kinetic energy. Since the particle is moving slower, it does not have to go as far into the soft wall before it hits its classical turning point. As the collision point moves closer to the vertex, the particles progressively penetrate further into the wall making the walls appear steeper than they are.

This effect was seen in both the simulations and the experiment. The soft walls effectively shifted the wedge angle by as much as 10^{o}. This effect was corrected for by making the potential of the billiard walls position dependent. A linear gradient was added to the potential height so that at the vertex, the potential was at its maximum and ramped down to zero at the top of the billiard. This correction factor is not exact since the penetration depth depends only on the normal component of velocity and not the total velocity. However, on average it is appropriate and was confirmed by both simulation and experiment.

Related to the problem of soft walls is spontaneous emission. Since

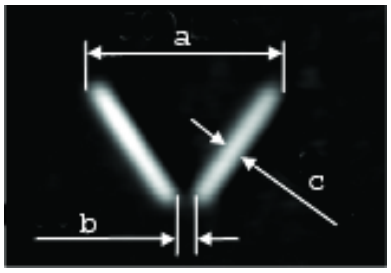

Figure 3.10: A CCD image of the actual wedge used in experiment. The dimensions are a) 500 μm, b) 50 μm, and c)56 μm

the atoms are bathed in light as they penetrate the wall, the possibility for absorbing a photon is present (see AppendixA). The far detuning of the billiard beam helps to keep the possibility of this event to a minimum. A numerical integration of the spontaneous emission rate over the path the atom takes while in the light during a bounce reveals the probability for a such an event to take place at less than 0.1% per bounce. An atom bounces on average 15 times during an experimental sequence, therefore the chance of spontaneous emission is an almost negligible 1.5%.

3.4 Results

The actual wedge used in the experiments is shown in Fig. 3.10. As was mentioned earlier, the $1/e^2$ spot radius is 28 μm. The Ti:Sapph was tuned 1.7 nm blue of the cesium atomic transition. Approximately 200 mW of power was in the optical beam used to create the billiard. This corresponds to a potential barrier of approximately 20000 $\hbar\omega_{rec}$ which is more than sufficient to contain atoms that have an initial mean energy of roughly 50 $\hbar\omega_{rec}$ and pick

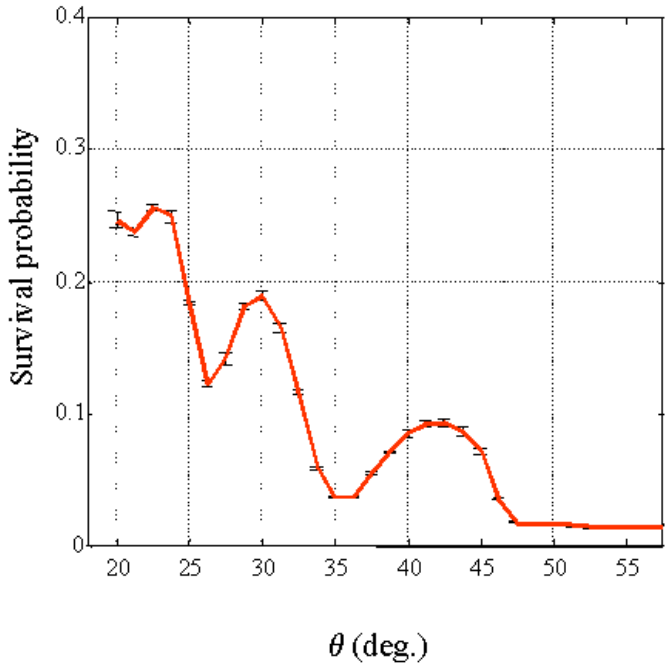

Figure 3.11: Survival probability as a function of the wedge angle. There are distinct peaks at 45°, 30°, and 22.5°, while near the catastrophic angles, 25.91° and 34.26°, there are distinct valleys. Beyond 45°, no atoms remain within the billiard.

up at most $5000\,\hbar\omega_{rec}$ as they fall from the top of the billiard to the bottom.

The measurement of the survival probability can be seen in Fig. 3.11. Qualitatively, the results appear to agree with theory. Clear peaks occur near 22.5° and 30° corresponding to 90°/4 and 90°/3 respectively. There appears to be a peak near 45°, although slightly shifted toward smaller angles. This can be explained by the fact that at 45° all the stable trajectories connect with the vertex, suppressing the peak at 90°/2.

Clear signatures of predominately chaotic behavior exist as well. At

26° and 34°, there are distinct valleys showing almost no survival probability. This is consistent with theory predicting global chaos for angles of 25.91° and 34.26° [61]. Similarly, above angles of 45°, the survival probability drops to zero. Again, this agrees completely with theory [51].

While qualitative agreement with theory is useful, a comparison with numerical simulations are more helpful to check our understanding of the system. Fig. 3.12 shows the experimental results alongside the results of a computer simulation. The simulation was performed using 10,000 particles and included the finite size of the billiard, the softness of the billiard wall, and spontaneous emission. There were no fitting parameters. The only alteration of the numerical results was a multiplication by 1/2. Aside from the original magnitude, the numerical results agree quite well with the experimental results.

One possible explanation for the magnitude discrepancy between simulation and experiment is interatomic collisions. Previous estimates of the collision rate for cesium atoms in this experiment gave an upper limit of 2.5% in 1 ms [67]. Given that the length of the experiment is 300 ms, the atoms likely experienced at least one collision during the course of the experiment. The collisions may mix the trajectories, enhancing the escape rate. This possible enhancement of the escape rate was not factored into the simulations, and this may account for the higher survival probabilities in the simulation.

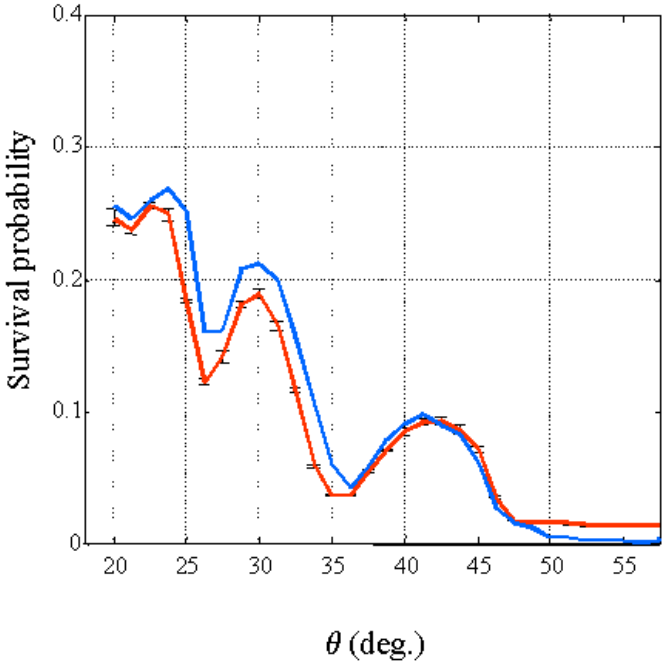

Figure 3.12: A comparison of experimental and numerical results for the wedge billiard. The red line represents the experimental results. The blue line is the numerical results which have been multiplied by a factor of 1/2.

3.5 Conclusion

Optical billiards provide a new testing ground for studies of chaos. Through the use of dual scanning deflectors, arbitrary two-dimensional billiard shapes can be drawn at will. The dynamics within the billiard is strongly dependent on the shape of the billiard. As this experiment has shown, billiards with unique mixing properties can be created. By appropriately choosing the shape of the boundary, a trap with ergodic mixing properties can be produced. This could be useful in stochastic cooling schemes that rely on mixing as one step in the cooling process [14].

This technique is not limited to billiard potentials. It can be extended into non-billiard like potentials by utilizing the soft-wall aspects of the potential. If the spatial extent of the shape drawn is roughly the same as the resolution, there no longer is a sharp boundary. Now there is a roughly harmonic potential where the flat potential of the billiard used to be.

The possibility of creating dynamic potentials also exists. There are limits on how fast the scanners can raster an image, but that image need not remain static. A circular billiard can be made such that the radius oscillates or deforms between a stadium potential and a circle at some frequency. Thus, the possibility of studying two-dimensional time-dependent chaotic systems exists.

To reiterate, the system studied in this experiment was completely classical in nature. The de Broglie wavelength of the atoms used in this experiment were much smaller than any other length scale in the experiment, making quantum effects negligible. However, that does not need to remain the case. With a higher resolution imaging system, it should be possible to make billiards on the order of tens of micrometers in size. With a sufficiently cold sample of cesium atoms, such as those produced through the use of lattice cooling techniques[18, 22, 68–70], it is possible to have de Bröglie wavelengths that are comparable to the size of the billiard. Alternatively, a Bose-Einstein condensate could be used as a source of cold atoms. The extremely low temperature of the condensate automatically yields de Bröglie wavelengths that are on the order of the billiard size. In addition, the Gross-Pitaevskii equation

governing the condensate has a nonlinear term, which means new studies of many body physics are also possible.

Chapter 4

Feedback Control

4.1 Overview

Manipulating ensembles of particles through feedback has evolved significantly since its use to increase the luminosity of antiproton beams [71]. This has led to proposals for cooling neutral atoms [14] and ions [72], as well as manipulation of wavepackets with ultrafast laser pulses [73]. The basic idea for feedback control of a physical system involves several steps. First, a measurement is made which probes the state of the system. Second, a correction to the system state is performed based on the result of the measurement. These together constitute feedback which may be used to control the system. The measurement as well as correction method differ among the various proposals and experiments in the field. In an experiment where the state of a system is to be controlled, it is desirable for the measurement to be as nondestructive as possible. Some experimental work [74] has involved the use of a high finesse optical cavity to monitor the position of an atom in real-time and to trigger a far-off-resonance dipole force trap (FORT) which confines the atom to a cavity mode. Other recent work [75] has involved making position measurements of atoms in an optical lattice and feeding back on that measurement to alter the oscillations of the atoms within the lattice. Our group has demonstrated a

method of feedback control that uses the method of recoil-induced resonances (RIR) [76, 77] to make a center-of-mass momentum measurement of a cloud of atoms and a moving optical lattice for changing the state of the system.

This experimental demonstration of real-time feedback control is a simplified single iteration model of stochastic cooling as discussed in Ref. [14]. A stochastic cooling setup entails a measurement and feedback determined correction as discussed here, but also includes a mixing process whereby the particles are allowed to rethermalize. In such a case, many iterations would be used to damp momentum fluctuations, for instance. In this demonstration, a measurement and correction are applied but without subsequent state mixing. This is not stochastic cooling, but rather a single iteration of a possible feedback sequence. Instead of damping out the momentum fluctuations of the ensemble, the average momentum of the entire group is damped. A measurement of the velocity distribution is made in order to obtain the center of mass velocity of the ensemble of particles. The information is used in real-time to provide feedback correction to the system in the form of a time dependent optical potential. This potential is a moving 1D optical lattice which traps the atoms and slows them to rest in the laboratory frame. The measurement-correction feedback iteration is done with relatively minor heating of the ensemble.

4.2 Recoil Induced Resonances

Most atom optics experiments are concerned with using light fields to affect atomic motion. This is accomplished when atoms scatter photons from laser beams. When this happens, the atom receives a momentum kick. The interesting thing is that by conservation of momentum, the light field must also have a momentum kick. The method of recoil induced resonances utilizes the change in the light field in an effort to measure the momentum distribution of the cloud of atoms.

The usual means for measuring the momentum distribution of a cloud of atoms is through ballistic expansion. In this procedure, the momentum distribution is converted into a spatial distribution. The trap holding the cloud is released and the atoms are allowed to expand for some amount of time. The atoms are then "frozen" in optical molasses [78] as a fluorescence image of the cloud is taken. This is repeated for various expansion times. By measuring the expansion of the cloud as a function of the expansion time, the momentum distribution of the cloud can be extrapolated. This method work extraordinarily well but has the disadvantage in that it is a destructive measurement.

As mentioned above, RIR works by measuring the change in momentum of a laser beam to determine the momentum distribution of the atoms. Granted, for there to be a change in the laser field's momentum, the atoms must have a change in momentum, but this can be kept to a minimum as will be shown. Therefore, this form of measurement, while not exactly nondestruc-

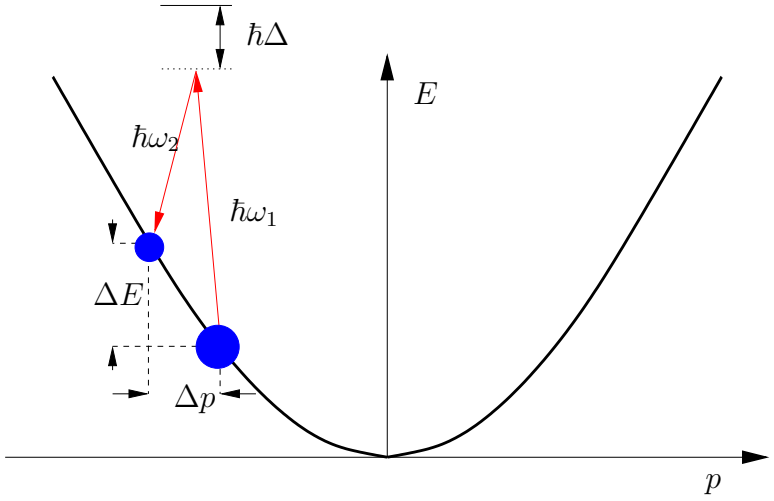

Figure 4.1: Stimulated Raman transitions between different motional states within a cloud of cold atoms. If the energy and momentum difference between two motional states within the cloud are equal to the energy and momentum difference beteen the pump and probe beams, the two classes are connected via a stimulated Raman process.

tive, is only minimally disruptive and the sample of atoms can still be used after the measurement.

RIR works by the process of stimulated Raman transitions between atomic motional states. Fig. 4.1 and Fig. 4.2 help to clarify the situation. Imagine two beams intersecting within a cloud of atoms. For any two velocity classes that have the same energy difference and momentum difference as photons in the two beams, stimulated Raman processes can occur. As atoms change velocity classes through this process, photons are redirected between the two beams. These deflected photons contain information about the population of the different velocity classes.

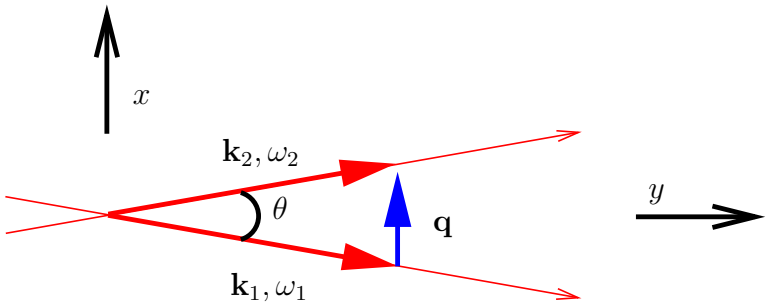

Figure 4.2: Beam orientation for RIR. The pump and probe beam intersect at an angle θ within a cloud of atoms. The momentum difference between the two beams is denoted by the wavevector $\mathbf{q}$.

Imagine two laser beams of nominal wavelength λ with wavevectors $\mathbf{k}_1$ and $\mathbf{k}_2$ ($k_1 \approx k_2 \equiv k_L$), which are detuned some amount Δ from the atomic resonance and δ with respect to each other, intersecting at a small angle θ in a cloud of atoms, as depicted in Fig. 4.2. For orientation, the beams are in the $x-y$ plane and the y axis lies along the axis of symmetry at an angle $\theta/2$ to both beams. Two separate conditions, one on momentum and one on energy, must be met in order for stimulated Raman transitions to take place. For the configuration depicted in Fig. 4.2, atoms can undergo a Raman transition from one motional state to another motional state when the difference in momentum between these two state is

$$\mathbf{p}_{final} - \mathbf{p}_{initial} = \hbar\mathbf{k}_2 - \hbar\mathbf{k}_1 = \hbar\mathbf{q} = \hbar q_x \mathbf{x}\,, \tag{4.1}$$

where

$$q_x = 2k_L \sin(\theta/2)\,. \tag{4.2}$$

For tiny angles, this is much smaller than the momentum distribution of the

cloud allowing for a much finer resolution of the atomic momentum distribution.

Similarly, energy must be conserved in the scattering process as illustrated if Fig. 4.1. This gives the relation

$$\frac{p_{final}^2}{2m} - \frac{p_{initial}^2}{2m} = \hbar\delta\,, \tag{4.3}$$

where δ is the frequency difference between the two beams. Together Eq. 4.1 and Eq. 4.3 create the condition

$$\mathbf{v}\cdot\mathbf{q} = vq_x = \delta - \frac{\hbar q_x^2}{2m}\,. \tag{4.4}$$

In the small angle limit, terms of order q_x^2 can be dropped leaving

$$\delta = \frac{p_x q_x}{m} \tag{4.5}$$

as the resonance condition for stimulated Raman transitions. This condition shows that there is a specific momentum class, p_x, singled out by a particular value of δ that is allowed to undergo Raman transitions.

The rate at which photons are scattered from one beam to the other depends on the population of the two velocity classes that are in resonance with each other. It has been shown [76, 77] that the scattering rate, W, from one beam to another is

$$W = N\frac{\pi}{2}\Omega_R^2\hbar m\frac{\partial\Pi}{\partial p}|_{p=\frac{m\delta}{q}}\,, \tag{4.6}$$

which is proportional to the derivative of the the momentum distribution, $\Pi(p)$. Here, N is the number of atoms, m is the mass of an individual atom,

and Ω_R is given by

$$\Omega_R = \frac{\Omega_1 \Omega_2}{2\Delta}, \tag{4.7}$$

where Ω_i is the resonant Rabi frequency for each beam. Therefore, by measuring the scattering rate of photons from one beam to another, the derivative of the momentum distribution can be obtained.

For each value of δ, one point in the derivative of the momentum distribution can be measured. In order to map out the entire momentum distribution, the measurement of the scattering rate must be done for a range of δ. This can be accomplished by linearly chirping δ. The derivation of Eq. 4.6 was done for a static δ, hence the assumptions used in that derivation place certain limits on the frequency chirp. Previous work [25, 79] has shown that the maximum scan rate for a momentum distribution of width Δp is

$$r_{max} \approx \frac{1}{2\pi} \left(\frac{q\Delta p}{m} \right)^2 . \tag{4.8}$$

This stems from the fact that in order to resolve a width of $\Delta\omega$, it is necessary to remain within the resonance condition for at least a time $\Delta t = 2\pi/\Delta\omega$. Likewise, if the resonance condition for two velocity classes is held for too long, then a substantial change in the momentum distribution can occur. The inverse of the Rabi frequency sets the time scale at which significant population transfer happens. This leads to a minimum scan rate of

$$r_{min} \approx \frac{\hbar q^2}{m} \Omega_R \, . \tag{4.9}$$

These limits will have to be followed for Eq. 4.6 to be valid.

It is appropriate at this point to be reminded of the fact that the RIR measurement is only minimally non-destructive. The fact that photons are scattered necessarily means that momentum is transferred to the atoms, spreading the momentum distribution. During each Raman transition an energy equal to $\hbar\delta$ is transferred either to or from the atoms. Integrating this over the entire sweep duration gives an average energy transfer of [25, 79]

$$E_{measurement} = \frac{4\pi}{r}\Omega_R^2 \hbar\omega_r \sin^2(\theta/2)\,. \tag{4.10}$$

This leads to a spreading of the momentum distribution described by

$$\sigma^2_{p,total} = \sigma^2_{p,initial} + 2mE_{measurement}\,. \tag{4.11}$$

4.2.1 Frequency Modulated RIR

The RIR measurement relies on photons being scattered either into or out of the probe beam. It is the change of the power in this beam that leads to a measurement of the momentum distribution. This gives rise to a ripple in the power on top of the probe beam. A figure of merit for the strength of the signal is the ratio of the ripple amplitude to the initial power in the probe beam. Because of noise and incomplete subtraction of the background power level, the minimum acceptable value for this ratio has been limited to 10^{-3} [79]. Due to the low resolution, previous experiments [80–83] were required to have the pump and probe beams close to resonance in order to have an observable signal. This led to a large amount of spontaneous emission, thereby heating the sample. This defeats the purpose of using RIR as a nondestructive means of measuring the momentum distribution.

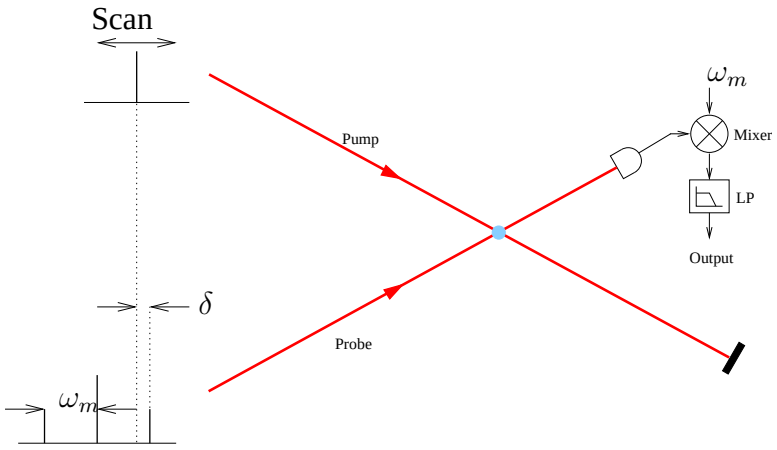

Figure 4.3: A schematic of frequency modulated recoil induced resonances. The probe beam has frequency sidebands placed on it by an electro-optic modulator. The pump beam is scanned in frequency such that the difference in frequency between it and the upper sideband of the probe beam is δ. After interacting with the atomic sample, the power of the probe beam is measured with a fast photodiode. That signal is mixed with the original modulation frequency ω_M to recover the RIR signal.

Frequency modulation spectroscopy is a method that allows us to detune farther away from resonance, hence reducing spontaneous emission, while still retaining a useful signal-to-noise ratio [79]. Fig. 4.3 gives a diagram to help illustrate the method. First, the probe beam is phase modulated at a frequency of ω_M before interacting with the sample of atoms. This puts frequency sidebands on the carrier beam spaced by integer multiples of ω_M and having a power spectrum given by [25]

$$I_{initial} = I_o \left[\sum_k J_k^2(M) + 2 \sum_{k<l} J_k(M) J_l(M) \cos([k-l]\omega_M t) \right] , \qquad (4.12)$$

where the amplitudes of the sidebands are given by Bessel functions and M is

the depth of modulation.

The frequency of the probe beam is appropriately chosen so that one of the sidebands adjacent to the carrier is very close in frequency with the pump beam while the carrier and the other sidebands are far away in frequency. If ω_M is much larger than the width of the momentum distribution, then only that sideband can interact with the atoms. Now, the pump and probe beams are used in the traditional manner to perform an RIR measurement. Upon exiting the atomic sample, the phase modulated probe beam contains the RIR signal at a frequency of ω_M. This can be seen be upon inspection of Eq. 4.12. It is clear that sidebands equidistant in frequency from the carrier are equal in intensity but 180^o out of phase. Therefore, if no atoms are present, the sidebands at $\pm\omega_M$ and higher will completely destructively interfere. On the other hand, when atoms are present, they interact with the pump and probe beams scattering photons either into or out of one of the probe beam sidebands based on Eq. 4.6. When the two sidebands of the probe beam interfere, the destructive interference is not complete. This gives rise to a photocurrent signal with amplitude

$$I_{sig} = \frac{2}{M} J_1^2 R\hbar\omega_o W \tag{4.13}$$

at the frequency of the phase modulation. If this signal is then mixed with the original modulating frequency ω_M, the output will be the near DC RIR signal. This in essence acts as a high frequency lock-in amplifier increasing the signal-to-noise ratio.

The RIR measurement determines the average momentum of the cloud

of atoms as a zero-crossing of the RIR curve, and this information can be used in a feedback scheme to stop the atoms. The intersecting beams create a standing wave or one dimensional lattice that is moving at a velocity

$$v_{\rm sw}^{\rm lab} = 2\delta\nu \frac{\lambda}{2\sin(\theta/2)} \tag{4.14}$$

with respect to the laboratory and

$$v_{\rm sw}^{\rm atoms} = 2\delta\nu \frac{\lambda}{2\sin(\theta/2)} - \frac{\overline{p}}{m} \tag{4.15}$$

with respect to the atoms. Assuming that the atoms are not initially at rest in the laboratory frame, a linear frequency sweep uniformly decelerates the lattice until it comes to a stop with respect to the atoms. Beyond which, the lattice accelerates in the opposite direction until it comes to a stop in the laboratory frame. The zero crossing of the RIR lineshape corresponds to when the lattice is stationary with respect to the atoms. By turning up the intensity of the beams at the zero crossing, deep potential wells are created that can decelerate the atoms as the standing wave comes to rest in the laboratory frame. This procedure of measurement and correction thereby stops the cloud of atoms in the laboratory frame.

4.3 Experimental Techniques

This experiment was performed using cesium atoms from a standard vapor-cell magneto-optic trap (MOT) [3]. The MOT apparatus used is the same one used for the billiards experiment (see Chapter 3) and is described in

great detail in Ref. [18, 21, 22]. We trap approximately 10^6 cesium atoms with Gaussian distributions in position and momentum with widths of $\sigma_y = 180\,\mu$m and $\sigma_p = 8.5\,\hbar k$, respectively. The experiment starts when the MOT is turned off and the atomic cloud is allowed to fall freely under the influence of gravity for 10 ms, during which it expands to a width of $\sigma_y = 350\,\mu$m. After these 10 ms, the cloud is subjected to an RIR velocity measurement.

The experimental setup used is shown in Fig. 4.4 and is similar to that which is described in Ref. [79]. The two RIR beams start as a single beam generated by the same Ti:Sapph laser used in the billiard experiments (see Chapter 3). In this experiment the light was detuned 6 GHz red of the $6S_{\frac{1}{2}}(F = 4) \rightarrow 6P_{\frac{3}{2}}(F' = 5)$ transition near 852 nm. This detuning was verified through the use of a wavemeter [18, 22] and a Fabry-Perot cavity. This beam is sent through an AOM operating at 80 MHz. This modulator (AOM1) is used to split the original beam into a pair which have a frequency difference of 80 MHz. This pair is to become the pump and probe beams.

The zeroth order beam from AOM1 is double passed through AOM2 operating at 54 MHz+$\delta\nu$ where $\delta\nu$ is a variable frequency. The double pass allows the driving frequency of AOM2 to be swept without steering the beam. It is then spatially filtered to clean the beam profile and aligned to hit the atomic cloud after a 10 ms free fall. The beam has a frequency that is shifted 108 MHz+$2\delta\nu$ relative to the original beam, and has a Gaussian intensity profile with a $1/e^2$ waist of 750 μm. This is the pump beam.

The first order beam from AOM1 is double passed through an electro-

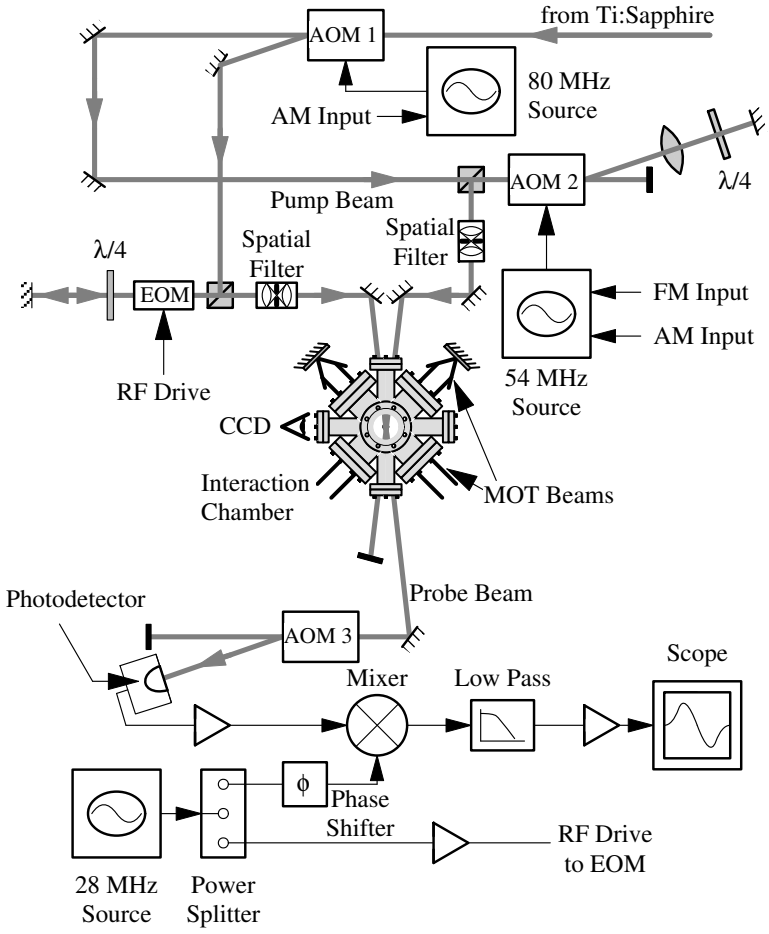

Figure 4.4: Experimental setup

optic phase modulator (EOM) from ConOptics Inc., model 350-40. Attached to the EOM is a helical resonator with a $Q \approx 250$ at a frequency of 28 MHz. The EOM is used to put sidebands on the carrier at ± 28 MHz . We drive the EOM to produce sidebands 2.5 dB below the carrier. The purpose of double passing the EOM is for reduction of residual amplitude modulation created by the EOM as the birefringence of the lithium niobate crystal drifts in time resulting in polarization modulation of the output beam at the driving frequency. Without compensation, the parasitic change in polarization results in a change in beam amplitude upon passing through the polarizing beam splitter cube that follows the EOM. The double pass setup with the quarter-wave plate allows us to correct for the drifts of EOM birefringence and reduce this effect. Following the EOM double pass, the beam is spatially filtered and aligned to intersect the atomic cloud where it has a $1/e^2$ waist of 750 μm. Since the beam was originally derived as the first order of AOM1, the carrier is 80 MHz above the original Ti:Sapph beam with sidebands at 53 MHz and 108 MHz. This is the probe beam.

The stimulated Raman transitions between motional states result from the interaction of the pump beam (108 MHz+$2\delta\nu$ relative to the original Ti:Sapph beam) and the upper sideband of the probe beam (at 108 MHz) which intersect at an angle $\theta = 4.5^{\circ}$. The frequency difference here is $2\delta\nu$, which is experimentally controlled. Depending on the frequency difference, Raman transitions are driven as the resonance condition in Eq. 4.5 is met. A frequency difference of $2\delta\nu = 0$ Hz, for example, corresponds to rest in the

laboratory frame, whereas $2\delta\nu = \pm 320\,\mathrm{Hz}$ corresponds to velocity classes at $\pm 1\, v_{rec}$. For a typical RIR measurement, $\delta\nu$ is linearly swept over a range that includes the entire velocity distribution. The best sweep rate for an optimal signal depends on the power in the beams as well as the detuning from atomic resonance [79]. Typically, the pump and probe beams have powers of 35 mW and 15 mW, respectively, with $\delta\nu$ swept at a rate of 74.3 MHz/s.

After the beams interact with the atoms, they exit the chamber where the pump beam is blocked. The probe beam passes through AOM3 after which the first order is detected by a photodiode. This additional AOM is used as a fast shutter to protect the photodetector from receiving intensities above the damage threshold during the correction phase which will be described shortly. Prior to interaction with the atoms, the FM sidebands on the probe beam were equal in intensity. As mentioned in Section 4.2 the interaction of the RIR beams with the atoms results in the scattering of photons from the pump beam into the upper sideband of the probe beam. The imbalance between the FM sidebands results in the amplitude modulation measured by a balanced photodetector from New Focus Inc., model 1607. The output of the detector is, therefore, a signal at the sideband frequency (28 MHz) with an amplitude that is proportional to the intensity mismatch between the sidebands (i.e. to the scattering rate which is proportional to the derivative of the velocity distribution).

The output of the photodetector is amplified and mixed with the original 28 MHz signal appropriately phase shifted which is subsequently low-pass

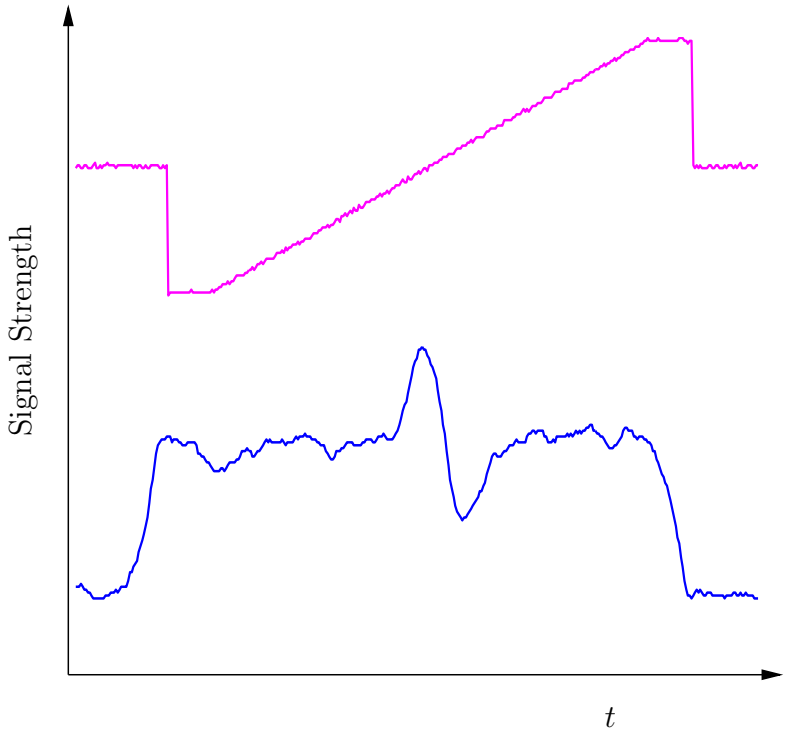

Figure 4.5: A typical RIR signal. The upper signal is the control voltage for the frequency sweep of the pump beam. The lower curve is the associated RIR signal. The DC offset of the RIR signal is due to residual amplitude modulation from the EOM at the modulation frequency. The vertical axis is arbitrarily scaled for the two signals.

filtered to remove the high frequency component and is then amplified. The result is a DC level with the dispersive RIR signal on top of it. The DC level fluctuates to some degree due to fluctuations of the residual amplitude modulation. A typical RIR scan is shown in Fig. 4.5.

In order to stop the falling atoms, the intensity of the pump and probe beam need to be increased when the standing wave formed by those two beams

is travelling at the same velocity as the atoms. To accomplish this, the RIR signal from the amplifier is fed into an analog electronic trigger circuit. The trigger circuit measures the DC level and subtracts it from the total signal. This leaves only the dispersive RIR lineshape which is compared to a reference voltage level. A trigger signal is generated once the signal passes the threshold level (see plots (a) and (b) in Fig. 4.6). Note that the trigger pulse actually comes prior to the zero crossing of the dispersive signal. To compensate for this offset, appropriate delays are added to the electronics that are triggered off this pulse. These delays are typically $20\,\mu$s and are not visible on the timing diagram in Fig. 4.6. The output of this comparator trigger is then used to initiate the sequence that stops the atoms. A timing diagram of the entire sequence is shown in Fig. 4.6.

The first curve (a) in Fig. 4.6 is the triggered RIR. Curve (b) shows the generated trigger pulse, curve (c) shows the linear frequency sweep which changes slope after the trigger for the reason explained below, and curve (d) shows the control signal for the correction which is achieved by increasing the intensity of both RIR beams. The combination of signals (c) and (d) brings the atoms to a stop in the laboratory frame as described above. During the high intensity phase (after the trigger), AOM3 is turned off (via an RF switch) to protect the photodetector. This is seen in curve (a). At the point of trigger on the curve, the light to the photodetector is turned off and the signal vanishes.

The increased intensity of the RIR beams provides the correction. The intensity in each beam increases according to $I(t) = I(0)/(1 + \Gamma t)^2$ [68]. This

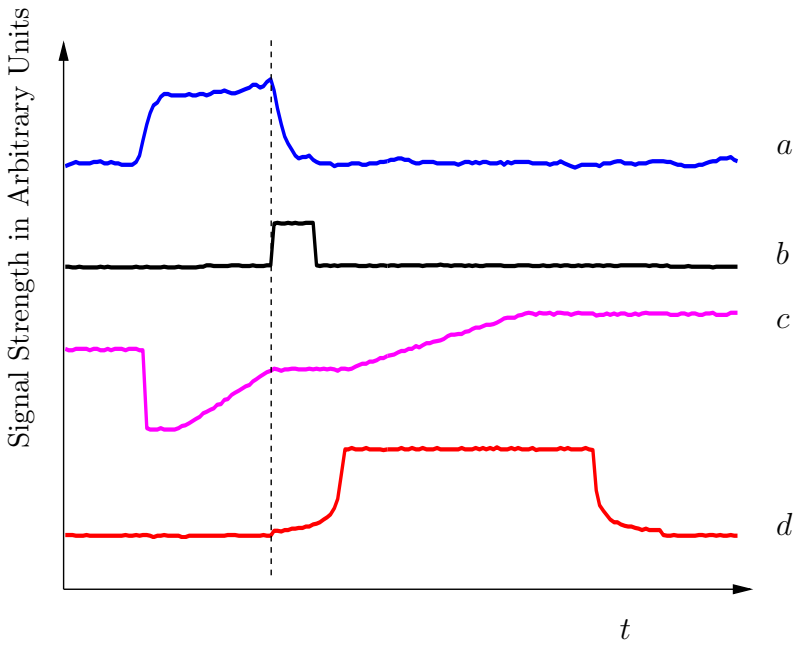

Figure 4.6: Timing diagram of voltage signals involved in the feedback scheme. The vertical axis is arbitrarily scaled for each signal. Signal (a) is the RIR signal up to the trigger point. Signal (b) is the trigger signal generated by the electronic trigger circuit. Signal (c) is the frequency sweep of the pump beam. Signal (d) is the control signal for the adiabatic increase of the beam intensity levels. The vertical dashed line marks the trigger point.

is an adiabatic increase to avoid heating the atoms during this process due to a sudden momentum kick. In the experiment we used $\Gamma = 44.4\,\mathrm{kHz}$ which disturbed the sample very little. Turning on the lattice more quickly was observed to heat the cloud significantly. On the other hand, size constraints limit the amount of time allowed for the adiabatic turn on. The beam size and cloud size are matched for an optimal RIR signal. Therefore, if the intensity is not raised quickly, the atoms will move out of the beam overlap region, and will not be caught in the moving lattice. The initial powers in the pump

and probe beams were 35 mW and 15 mW, and were adiabatically increased to 75 mW and 70 mW, respectively. Curve (*d*) in Fig. 4.6 is the amplitude modulation signal to AOM1 and AOM2 (with different heights for each) that provides this increase to higher intensity.

The frequency sweep is also altered after the trigger pulse. At first, the linear frequency sweep is stopped during the adiabatic turn on. Ideally, the lattice velocity should follow the free fall velocity of the atoms during the adiabatic turn on, but that is difficult due to signal delays (especially due to the low pass filter), therefore we simply hold the lattice at its current speed. Secondly, the acceleration of the lattice after the adiabatic turn-on (proportional to the slope of the frequency) is changed. In an accelerating lattice, atoms will undergo Landau-Zener tunneling [84], escaping the lattice, and will not be stopped. The constant acceleration is decreased to avoid this tunneling, but kept high enough so that atoms would not exit the beam overlap before being stopped. The initial lattice acceleration for the RIR scan was 810 $\mathrm{m/s^2}$ and was changed to 150 $\mathrm{m/s^2}$ for slowing.

4.4 Results

The primary result of this experiment is shown in Fig. 4.7. The data points on the lower red curve correspond to the initial cloud of atoms falling under gravity with no corrective slow-down. These are averaged over five free fall sequences. The dashed curve is a ballistic trajectory of the MOT falling under the influence of gravity.

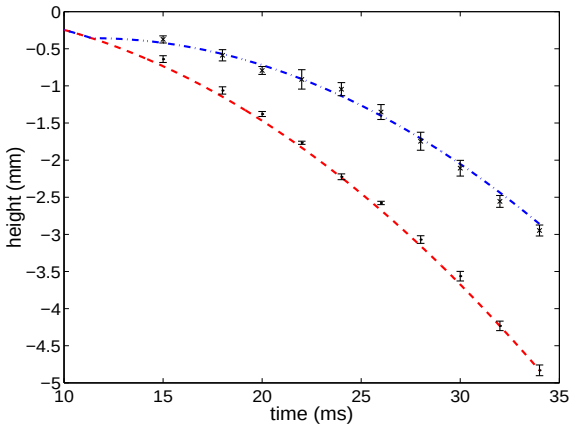

Figure 4.7: Center of mass position of a cloud of atomic cesium falling with and without correction. The data on the lower red curve is falling under gravity with no correction. The data on the upper blue curve is falling with a corrective slow-down at 10 ms.

The data points on the upper blue curve correspond to atoms that were stopped and then allowed to fall again averaged over ten correction sequences. For the first 10 ms, the atoms follow the same free fall curve as described previously. The RIR and slow-down sequence starts at 10 ms after the initial release from the MOT. The sequence stops the falling atoms and then releases them to fall again approximately 1.5 ms later. The dotted curve is a ballistic trajectory with an initial momentum of $0\,\hbar k$ at 11.5 ms. There is good agreement between the data and the idealized trajectory.

Ideally, the trigger pulse turns on the deep well lattice at a time when both the average velocity of the atoms and the lattice are the same. In this case, we achieve stopping efficiency of approximately 80% of the atoms. Perfect stopping efficiency is not possible in our system due to the lower intensities

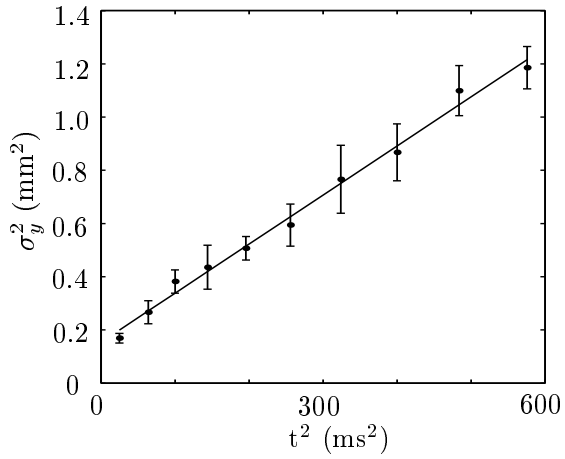

Figure 4.8: Temperature measurement of the cloud after stopping showing the cloud's expansion as a function of time.

in the wings of the beams creating smaller potential wells that can not slow the atoms. Another source of lower efficiency is noise on the RIR signal which causes the trigger time to vary. This leads to a velocity mismatch between the atoms and the lattice. Typically, the noise causes triggering within a window of 7 recoil velocities about the ideal trigger point. This problem is observed to result in loading efficiencies into the lattice as low as 50%.

To measure the heating effects of this method we plot the square of the width of the cloud, σ_y^2, as a function of time squared in Fig. 4.8. From this fit, we determine the momentum width via $\sigma_y^2(t) = \sigma_y^2(0) + t^2\sigma_p^2/m^2$. Before the correction sequence the momentum distribution has a width of $\sigma_p = 8.5\,\hbar k$ and after $\sigma_p = 12.2\,\hbar k$.

Heating results from various sources including spontaneous emission

and coherent processes involved in the RIR measurement as mentioned earlier in Section 4.2. The beams operate at a detuning of 6 GHz to the red of the atomic transition which allows for a reasonably small rate of spontaneous emission. We measure heating of the sample to a momentum width of $\sigma_p = 9\,\hbar k$ from this effect alone. A larger detuning may be used to decrease the spontaneous emission at the expense of a lower well depth for the corrective slow-down.

The RIR measurement is only approximately nondestructive. There is an increase in the momentum width due to the coherent scattering of photons as described in Section 4.2. In our system, the momentum distribution after an RIR measurement when not followed by a corrective slow-down has a width of $\sigma_p = 16\,\hbar k$. In the correction scheme, this heating effect is not fully present since the RIR scan is halted after the trigger which takes place before the halfway point in the scan. The heating effect of the coherent scattering may be reduced by decreasing the scattering rate. This may be accomplished by reducing the power in the beams and/or increasing the detuning. Of course, this is at the expense of the signal for the obvious reason that the signal is smaller if fewer photons are scattered.

Fundamentally, the measurement can not be fully nondestructive. Ultimately, the degree of nondestructiveness is determined by the threshold of the RIR measurement, which ideally is dictated by the shot-noise limit. The figure of merit here is the signal-to-noise ratio. A minimum signal-to-noise ratio, $\frac{S}{N}$, is required for the triggering electronics to work. For a shot noise

limited detector [79],

$$\frac{S}{N} \propto \frac{I_{\text{pump}}\sqrt{I_{\text{probe}}}}{\Delta^2}\,, \tag{4.16}$$

and the heating, H, goes as

$$H \propto \frac{\sqrt{I_{\text{pump}} I_{\text{probe}}}}{\Delta}\,, \tag{4.17}$$

where I_{pump} and I_{probe} are the intensities of the pump and probe beams. Therefore, for a fixed signal-to-noise ratio at the limit of the electronics,

$$H \propto \sqrt{\frac{\mathrm{S}}{\mathrm{N}}}\sqrt[4]{\mathrm{I}_{\text{probe}}} \tag{4.18}$$

The heating changes slowly as a function of the probe intensity. Within this experimental realization it would be difficult and at the limit of the detector's ability to reduce the heating any more and still have an acceptable signal-to-noise ratio.

4.5 Conclusions

The basic result of this proof-of-principle experiment is that real-time measurement and correction feedback are possible with a controllable amount of perturbation. The center of mass motion of the atoms was controlled in real-time with minimal disturbance to the sample. As demonstrated, this method does not rely on any *a priori* information about atomic motion. As long as the average velocity of the cloud is within the measurement range of the RIR scan, the scheme should work on any unknown average velocity.

Chapter 5

The Quantum Tweezer for Atoms

5.1 Overview

Scientists have long been interested in completely controlling the state of a quantum system. Doing so allows one to fully explore the fundamentals of quantum mechanics. Exotic systems such as entangled states, Schrödinger cat states, quantum computers, and quantum teleportation become possible [16]. As these these situations are active theoretical topics, an experimental realization of a single quantum system with control over the quantum mechanical state is desirable.

In order to engineer such quantum states, complete control over all degrees of freedom is required. A single neutral atom in the ground state of a microtrap provides a desirable starting point for producing different quantum states. In this system, a neutral atom with a specific internal state is in a well-defined energy eigenstate of a trap that is fixed at a chosen point in space. Our group has performed experiments that will lead to the production of atoms in the ground state of an optical trap with near unit probability.

The original idea for this scheme was developed by Niu and Raizen in 2002 [17]. In its simplest form, a Bose-Einstein condensate (BEC) is used as

a reservoir of atoms from which a microtrap extracts a single atom. It relies on the coherence properties of the condensate, as well as the mean field interactions of the atoms within the microtrap, to create a series of tunnelling opportunities for the atoms between the condensate and the tweezer. By appropriately tailoring the separation of the quantum tweezer from the condensate, as the system moves through the tunnelling opportunities, all but one of the atoms within the tweezer are forced to tunnel out. The end result is a single atom in the ground state of the microtrap.

This means for attaining a single neutral atom is not the only one available. Other ideas have been developed and pursued by different groups. Severral groups are pursuing single atoms through weak magneto-optical traps (MOTs)[85–87]. These MOTs are operated such that the the average number of atoms in the trap is on the order of one. When a single atom is detected in the trap, it is then loaded into an optical dipole trap [88, 89]. These schemes are fundamentally sound, but suffer from some undesirable features. They are not a deterministic source of atoms. In addition, the atom is not in a well-defined vibrational state of the dipole trap and requires additional work to place it into the ground state once it is captured. With the quantum tweezer, this comes free of charge.

Another possible method relies on the Mott insulator transition in Bose-Einstein condensates [90]. The Mott insulator transition occurs when a condensate is placed in an optical lattice. As the well depth of the lattice increases, a phase transition from a superfluid state to a number state in the

lattice sites occurs [91]. This produces number states within the lattice site, but at the cost of addressability. Optical lattices have well sites located half a wavelength away from each other making it near impossible to individually address a single atom within a well.

The remainder of this chapter explains the theory and implementation of the quantum tweezer. The exact means by which the tweezer extracts atoms is slightly changed from the original proposal. These differences as well as the actual data from the experiment are described below.

5.2 Quantum Tweezer Theory

The quantum tweezer uses a BEC as a reservoir for extracting single atoms. The scheme is depicted in Fig. 5.1 and Fig. 5.2. To begin, consider a one-dimensional condensate in a harmonic trap characterized by the frequency ω_x. The condensate is described by the following one-dimensional Gross-Pitaevskii equation

$$\left(-\frac{\hbar^2}{2m}\frac{\partial^2}{\partial x^2} + V_{ext} + g_{1D}|\phi^2|\right)\phi(x) = \mu\phi(x)\,, \tag{5.1}$$

where g_{1D} is the one dimensional coupling constant and μ is the chemical potential (see Appendix B). Here, $V_{ext} = \frac{1}{2}m\omega_x^2 x^2$ is the external potential that holds the condensate.

Within the condensate, a microtrap is slowly turned on at the center of the trap. In the beginning, the tweezer is only a small perturbation to the trapping potential. The microtrap is formed by two repulsive gaussian barriers

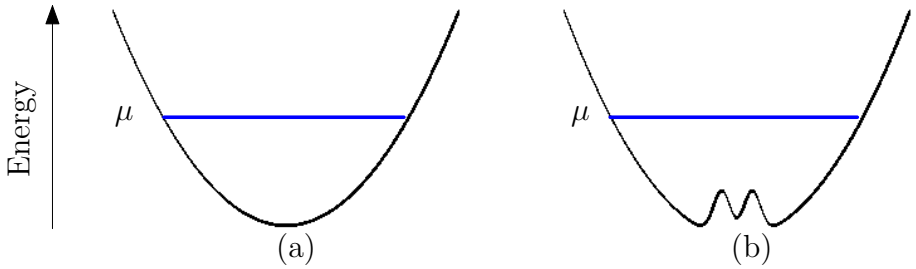

Figure 5.1: A diagram of how the tweezer works. In (a), a one-dimensional condensate is trapped in a harmonic potential characterized by the trap frequency ω_x. The blue line represents the chemical potential of the condensate. Image (b) shows the introduction of the tweezer into the condensate. It is slowly turned on in the center of the harmonic trap. At this point the tweezer is only a small perturbation to the harmonic trap.

forming a trapping region between the two of them. The potential takes the form

$$V_{dot}(x) = V_o(e^{-\frac{2(x-d)^2}{w_x^2}} + e^{-\frac{2(x+d)^2}{w_x^2}}) \,. \tag{5.2}$$

These two repulsive gaussian potentials are characterized by a waist w_x and a separation distance $2d$. Such a trap has a trapping frequency given by

$$\omega_x = \sqrt{\frac{8V_o}{mw_x^2} e^{-\frac{2d^2}{w_x^2}} \left(4\frac{d^2}{w_x^2} - 1\right)} \,, \tag{5.3}$$

(see Appendix A for details). Note that the external potential in Eq. 5.1 is now the sum of the harmonic trapping potential and the tweezer potential. The microtrap is turned on by increasing V_o and pushing the tweezer up in energy through the condensate. In addition to raising the energy of the states within the trap, it increases the potential by changing the trap frequency. This can be compensated for by adjusting the distance between the two gaussian barriers. The different multi-atom ground state energy levels become degenerate with the chemical potential of the condensate as the tweezer is ramped on.

It is through these degeneracies that the tweezer operates. When the energy level of the atoms within the tweezer and the chemical potential are equal, an atom in that state can tunnel out of the tweezer and back into the condensate. At this point the number of atoms within the tweezer decreases by one, thereby reducing the energy of the atoms within the tweezer and removing the degeneracy condition. As the tweezer potential continues to increase, the energy of the atoms is again degenerate with the chemical potential and an atom can again tunnel out of the microtrap. This process continues until the

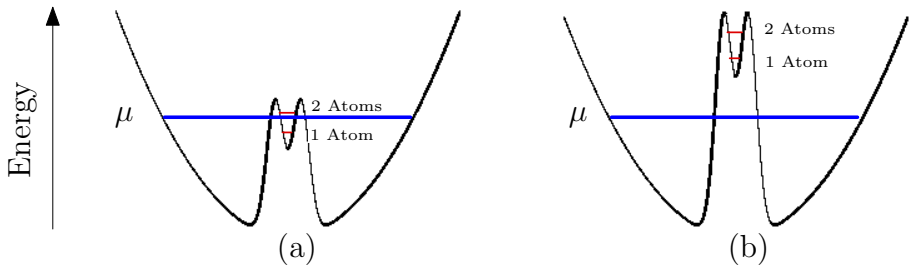

Figure 5.2: A continuation of the pictorial description of the quantum tweezer. In (a), the tweezer trap has risen and now the individual multi-atom ground states within the microtrap become degenerate with the chemical potential. The red lines represent the one atom and two atom ground states while the blue line represents the chemical potential of the condensate. Image (b) shows the tweezer after it has exited the condenstate and is fully decoupled from it.

tweezer has energetically pushed through the condensate and is completely decoupled from it. Whatever atoms happen to remain in the tweezer after the tunnelling opportunities will remain in the tweezer. In general, the output state of the tweezer will be some superposition of multi-atom ground states. The key to single atom extraction is to tailor the turn on rate of the tweezer such that only the single atom ground state has a high probability of being in the microtrap after extraction.

In order to obtain a better understanding of how to extract only one atom, it is instructive to look at the energy levels of the multi-atom ground states within the tweezer trap. The energy of the different states depends on the energy level of the trap, the number of atoms in the state, and the coupling of the state to the condensate. A mathematical analysis of the system [17, 92, 93] yields, for n atoms in the ground state of the tweezer,

$$E_n = nE_1 + \frac{n(n+1)}{2}\nu\,, \tag{5.4}$$

where E_1 is the energy of an atom in the trap relative to the chemical potential of the condensate and ν represents the repulsion atoms feel within the microtrap. The energy difference between the tweezer and the chemical potential has several contributions and has the form

$$E_1 = \epsilon_{Dot} + V_{offset} - \mu + \frac{g_{1D}}{2}NJ_{2,2} \tag{5.5}$$

where ϵ_{Dot} is the ground state energy level of the microtrap, V_{offset} is the potential offset created by the microtrap, μ is the chemical potential of the

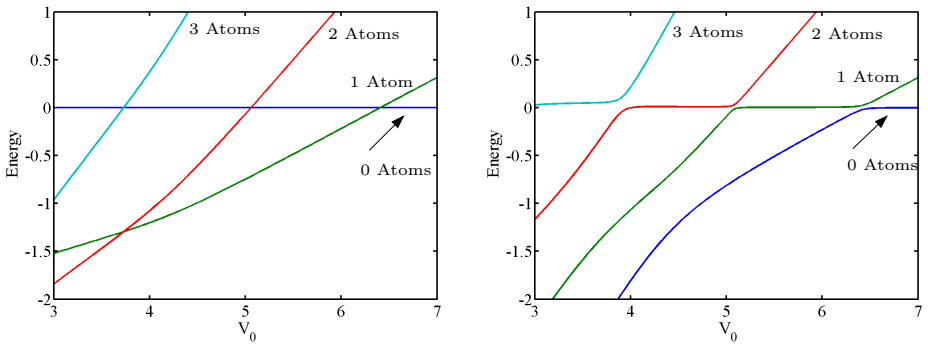

Figure 5.3: Energy diagrams for the multi-atom ground states within the tweezer as a function of the potential height of the tweezer. The diagram on the left corresponds to the case where the coupling between the tweezer and the condensate is neglected. On the right, the coupling is included, causing energy gaps where there were previously crossing. The energies are plotted in units of 5.65 nK. Plots courtesy of Artëm Dudarev [93].

condensate, and $J_{2,2}$ is the generalized overlap integral of an atom in the microtap with an atom in the condensate. It is given by the equation

$$J_{l,m} = \int (\phi_{BEC})^l (\phi_{Dot})^m \mathrm{dx} \tag{5.6}$$

where ϕ_{BEC} is the wavefunction of the condensate and ϕ_{Dot} is the wavefunction of the atoms within the tweezer. The mean field repulsion an atom feels when confined in the tweezer is given by $\nu = gJ_{0,4}$.

Fig. 5.3 shows the change in the energy levels as a function of the potential height of the tweezer. This calculation assumed a specific set of experimentally feasible parameters. The trap was assumed to have frequencies of 30 kHz in the tight dimensions and 3 Hz in the weak dimension. In addition, the tweezer trap was characterized by a trap frequency of 200 Hz, and 100

atoms were assumed to be within the condensate to have a reasonable lifetime due to three-body losses. Eq. B.22 yields a one-dimensional condensate with a chemical potential of $\mu \simeq 21\,\mathrm{nK} \cdot \mathrm{k_B}$. As the potential is increased, the energy levels will increase. When the tweezer is well below the chemical potential, the higher atom number states have lower energy, whereas when the tweezer is decoupled from the condensate, the higher atom number states have higher energy. This inversion of levels from inside the condensate to outside the condensate leads to level crossings as shown in Fig. 5.3. These level crossings physically correspond to the aforementioned degeneracies. The point when the $i+1$ atom level crosses the i atom level is when the potential has been raised such that the $i+1$ atom ground state is degenerate with the chemical potential. At this point, one atom from the $i+1$ state can tunnel out of the tweezer, reducing the number of atoms within the microtrap to i.

To quantify the tunnelling rates, analysis of the system including the coupling between the atoms in the tweezer and the condensate is necessary [17, 92, 93]. The off diagonal terms in the Hamiltonian give rise to this coupling. Fig. 5.3 shows the effect of this coupling on the energy levels. An energy gap appears at the energy level intersections, creating avoided crossings. These avoided crossings dictate the parameters under which an atom can tunnel from the tweezer to the condensate.

In situations where avoided crossings occur, the possibility of jumping from one energy level to another occurs via Landau-Zener tunnelling [94]. The probability of making the transition from one level to the other after one pass

is

$$P = \exp\left(-\frac{(2\pi)^2}{h}\epsilon_{12}^2/|\frac{d}{dt}(\epsilon_1 - \epsilon_2)|\right), \tag{5.7}$$

where ϵ_{12} is the energy gap between the two levels and $\frac{d}{dt}(\epsilon_1 - \epsilon_2)$ is the difference in the slope of the energy levels. In the case of the tweezer, this can be approximated as the slope of the lower energy level away from the gap. From this the probability for an atom to tunnel from the tweezer into the condensate can be calculated. Fig. 5.1 shows that when the tweezer is deep inside the condensate, the barrier between the tweezer and condensate is very small, if it exists at all. Therefore, the large coupling give rise to large energy gaps. As the tweezer potential is raised, the barrier between the tweezer and condensate grows, reducing the likelihood of atoms tunnelling out. The energy gaps therefore decrease.

The idea behind the tweezer is to pick an extraction rate for the micro-trap such that the system adiabatically follows the lowest energy level at each crossing until the final crossing, where the system makes a non-adiabatic jump across the energy barrier leaving one atom within the tweezer with high probability. Fig. 5.4 shows a plot of the probability of different number states in the tweezer after extraction as a function of extraction rate. The plot shows a region of extraction rates where there is high probability of pulling out a single atom with the tweezer. Over almost an order of magnitude in ramp on rates for the tweezer, the extraction probability is greater than 90%. It should be noted that this calculation assumed a linear increase in the tweezer potential. Conceivably, a nonlinear ramp could be used such that when the

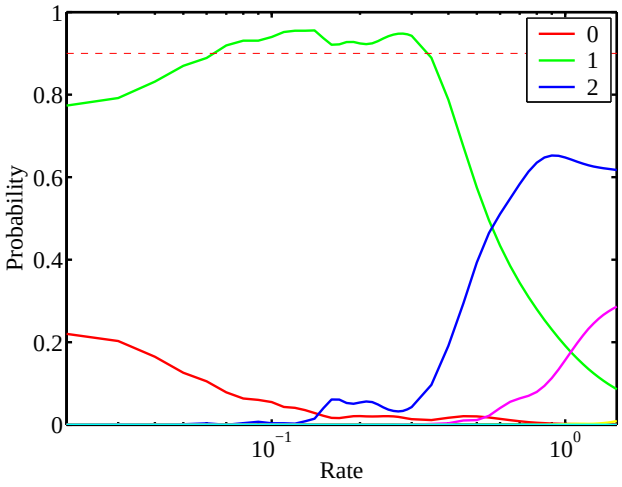

Figure 5.4: The probability of finding n atoms within the tweezer after extraction as a function of the extraction rate. The different colors correspond to different atom numbers as labelled in the upper right corner. The extraction rate is plotted in units of 4.3 nK/ms. The red dotted line highlights when the one atom extraction probability is greater than 90%. This range corresponds to extraction rates between roughly 30 ms and 130 ms which are feasible for the experiment. Plot courtesy of Artëm Dudarev [93].

gaps are large deep within the well, the potential rises slowly and increases later when the final one atom to zero atom gap is reached. This may lead to even higher probabilities for the one atom state.

5.3 Experimental Techniques

In order to perform the quantum tweezer experiment, several things are necessary. First, a one-dimensional condensate must be created. Specialized traps with high oscillation frequencies are required to reach the one-dimensional regime. In addition to those traps, a trap to create the tweezer is needed. And finally, a means to confirm single atom extraction is needed. This system needs to be able to detect the low light levels associated with a single atom scattering light as well as have the sensitivity to distinguish between a single atom or multiple atoms.

5.3.1 Optical Traps

The condensate produced within the QUIC trap and described in Chapter 2, Section 2.6 does not meet the requirements necessary to perform the quantum tweezer experiment. To begin with, it is very much a three dimensional condensate. It would be possible to evaporate further, hence reducing the atom number in the condensate and eventually reaching the one-dimensional condensate condition [95], but the trapping frequencies are still too low to perform the experiment. The weak trap frequencies do not provide a sufficient separation of the energy level crossings to achieve a pure number

state. The magnetic trap is limited in the range of trap frequencies it can produce. It will never be able to produce the 30 kHz tight confining frequencies required for the tweezer experiment to work.

In an effort to address these problems, a new procedure for creating condensates was developed. Optical traps offer an elegant solution to this dilemma. They can be easily adjusted to form many desired shapes, simply by changing a few optical elements. In addition, extremely high trap frequencies are possible by focussing the beam down to very small ($\approx 2\,\mu$m) waists. Appendix A provides details on the different geometries available by using optical traps.

The optical traps are created from the two far off resonance lasers mentioned in Chap. 2. The Verdi laser creates the repulsive potentials and the fiber laser creates the attractive potentials. Since the beams create interesting trapping geometries it is worthwhile to describe the beam preparation and transport to the chamber.

The red attractive traps are the simpler traps to create. The randomly polarized output of the fiber laser is split into two beams of equal intensity with a polarizing beam splitting cube (PBSC). These two beams will be used to create a vertical and horizontal red trap. The vertical trap is used to create lower dimensional condensates while the horizontal trap is used for alignment purposes. Both beams pass through an acouto-optic modulator (AOM) that acts as a fast shutter for the beams. The horizontal beam is generated from the first order of a 50 MHz AOM while the vertical beam uses

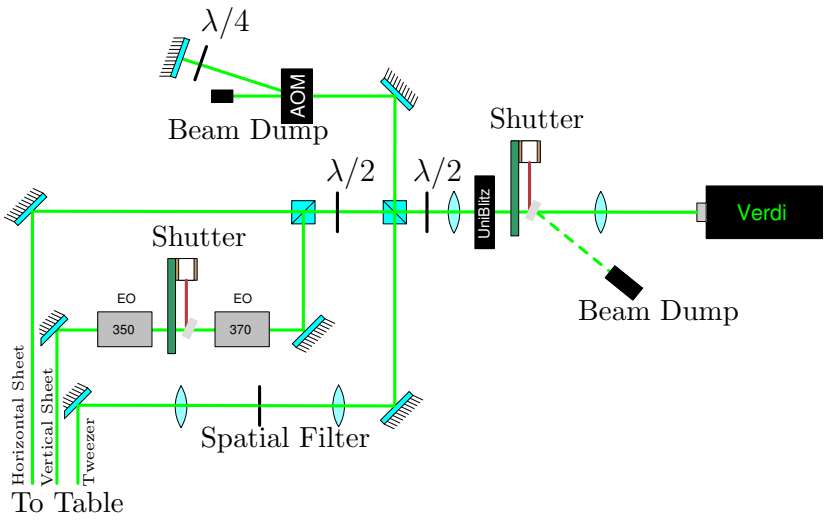

Figure 5.5: The layout of the optics on the Verdi table used to create the three separate repulsive traps.

the negative first order of an 80 MHz AOM. This ensures that there will be no static interference pattern, should both beams be used simultaneously with atoms. After the AOMs, both beams are spatially filtered and pass through a homebuilt shutter (see Chap. 2) in the beam path. At this point, the horizontal beam has a waist of roughly 3 mm and the vertical trap has a waist of roughly 5 mm. These collimated beams are then transported to the vacuum chamber.

The repulsive traps are more numerous and therefore distributed via a slightly more complicated scheme as shown in Fig. 5.5. The Verdi laser resides on a separate optical table. The output of the laser is sent through a telescope that is used solely for shuttering purposes. Within the telescope beam path are two shutters. The first is a homebuilt shutter with a silver mirror attached

to the flag. The reflected beam is sent to a beam dump. The additional weight of the mirror slows down the response of the shutter, reducing its effectiveness. This is remedied by the use of a second shutter, a UniBlitz 1" shutter with a reflective coating on the shutter blades. The UniBlitz shutter is fast, but the reflective coating has a low damage threshold, therefore it can withstand the full power of the Verdi for only a short time. Together, these two shutters act as the mechanical shutter, with the UniBlitz quickly blocking the beam and the homebuilt shutter blocking the beam shortly thereafter.

After the shutters, the beam goes through a $\lambda/2$ waveplate and a PBSC to create two beams with adjustable power control. One arm of the cube will eventually create the tweezer trap. This beam is double passed through a 40 MHz AOM using the first diffraction order. The output is separated using the PBSC. It is then spatially filtered. The collimated output has a waist of roughly 1.5 mm with a maximum of about 1 W of power. From this point the beam is transported to the table holding the vacuum chamber.

The other output beam of the cube is used to create the optical traps necessary to create a one-dimensional condensate. This beam is again sent through a $\lambda/2$ waveplate followed by a PBSC to split the beam into two beams of roughly equal power. One arm has a waist of roughly 1.5 mm with about 3 W of total power. This beam is transported directly to the main optical table. The other arm is passed through two electro-optic modulators (EOMs) acting as intensity modulators. The first EOM is from ConOptics, model 370, and is driven by one channel of a Trek high voltage dual amplifier, model 601C.

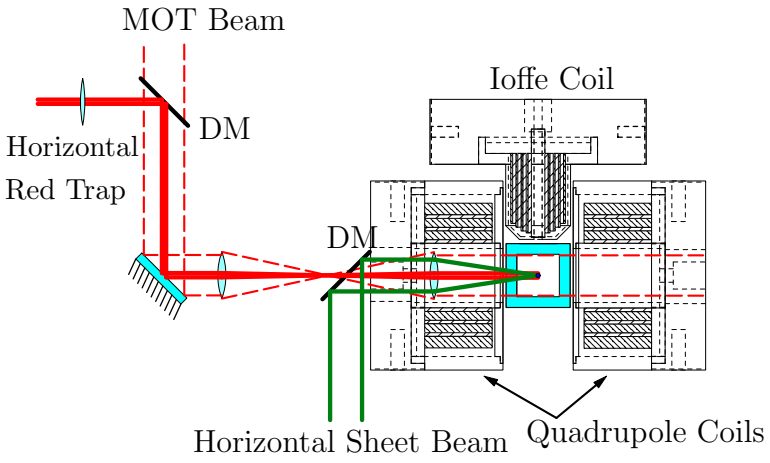

Figure 5.6: Layout of the horizontal optical traps. The beams make their way into the MOT beam path through the use of dichroic mirrors (DM).

The second EOM is also from ConOptics, but is model 350, and is driven by the other channel of the Trek amplifier. The two EOMs can provide 47 dB of attenuation to the laser beam. After the EOMs, the beam has a waist of roughly 1.5 mm and has a maximum power of 3 W.

Once the beams arrive at the chamber, they are appropriately shaped before entering. The traps can be organized according to their orientation with respect to the chamber. The horizontal traps are comprised of a horizontal red trap and a horizontal green sheet trap. The vertical traps consist of a vertical red trap, the vertical green sheet trap, and the tweezer trap.

The horizontal traps enter the glass cell as shown in Fig. 5.6. Before entering the chamber, the horizontal red trap passes through a 300 mm focal length lens. The beam is then superimposed on the lower MOT beams with

the use of a dichroic mirror (DM). The lens is approximately 300 mm away from the center of the chamber, where the atoms are located. The focussing of the red beam is such that at the atoms, the beam is symmetrical with a waist of $\approx 40\,\mu$m. The beam from the Verdi table passes through an acousto-optic deflector with a bandwidth of 50 MHz centered at 110 MHz. The first order of this beam passes through a 50 mm focal length lens. This lens is the first lens of a telescope used to expand the beam. The final lens of the telescope is a 250 mm achromat creating a collimated output beam with a waist of ≈ 7.5 mm. This beam is then transported to the chamber through a series of mirrors. Immediately before entering the chamber, the beam passes through a 50 mm focal length lens, as shown in Fig. 5.6, which focusses the beam to a waist of $2.6\,\mu$m at the location of the atoms. To create a sheet, within the collimated portion of the beam, a 1000 mm focal length cylindrical lens is used to move the focus in one direction off of the atoms. The end result is a sheet beam that has a waist of $\approx 2\,\mu$m in the direction of gravity and $\approx 100\,\mu$m perpendicular to gravity.

The vertical traps enter the chamber in a slightly more complicated manner. The vertical red trap beam passes through a 150 mm lens, after which it focusses to a spot at the focal length of the lens. This spot is then imaged using the lens tower shown in Fig. 5.7. A 200 mm lens in the upper part of the tower forms a transport system from the image which is then reflected upwards with a dichroic mirror. The beam passes through a 50 mm Gradium lens and is focussed to a spot above the position of the atoms. The 150 mm

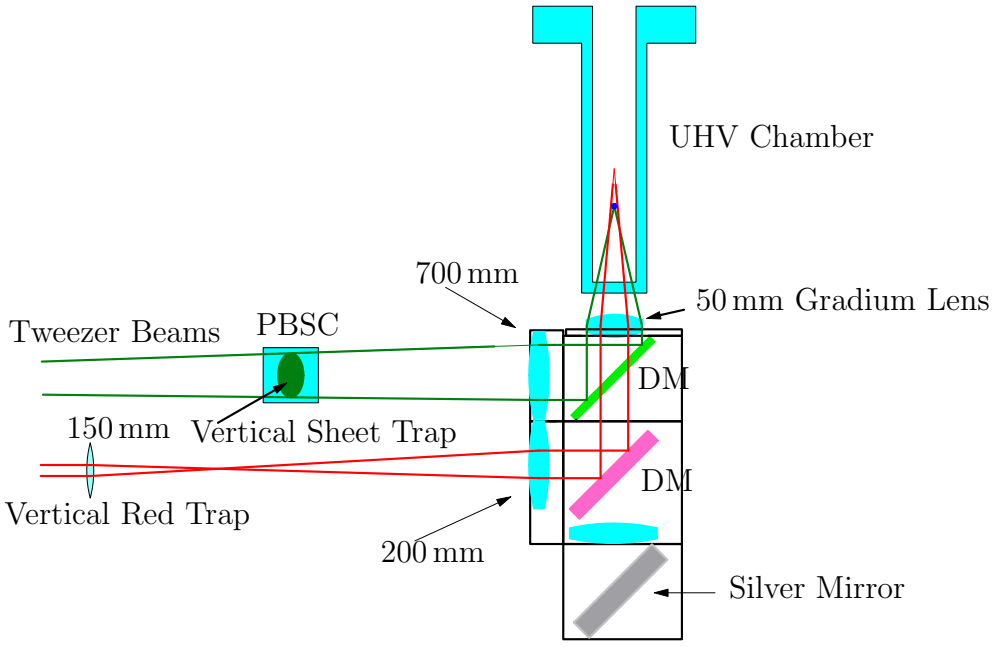

Figure 5.7: Layout of the vertical optical trap beams. The beams enter the chamber through a tower of optics located below the glass cell. The bottom optical port is separate from the optical traps and is used for the vertical imaging system.

lens is positioned such that at the location of the atoms, the beam has a waist of $\approx 40\,\mu$m.

The vertical green sheet trap is formed in a manner similar to the horizontal green sheet trap. The beam from the Verdi table passes through a 140 mm focal length lens. This lens, in conjunction with a 700 mm focal length lens, forms a telescope which expands the beam to a waist of approximately 6 mm. Within the telescope region, a polarizing beam splitting cube (shown in Fig. 5.7) is used to combine the vertical green trap with the tweezer trap; the tweezer trap will be described later. The collimated beam is reflected by a dichroic mirror upwards toward the aforementioned Gradium lens. The Gradium lens focusses the beam to a spot with a waist of $\approx 2.6\,\mu$m at the location of the atoms. As before, in order to make the green vertical trap a sheet, a 100 mm focal length cylindrical lens is placed in the beam path. This time it is placed within the telescope region, moving the focus in one direction away from the atoms. The end result is a beam with a waist of $\approx 2.6\,\mu$m in one direction and $75\,\mu$m in the other direction.

The last vertical trap is the tweezer trap. Again, this trap is similar to the two other green traps. The beam from the Verdi table passes through an acousto-optic deflector with a bandwidth of 50 MHz centered around 110 MHz. This deflector has the capability of being driven by multiple frequencies simultaneously. A bank of temperature stabilized voltage controlled oscillators (VCOs) are controlled by the computer such that they produce a desired set of frequencies. The RF power of these VCOs are individually computer con-

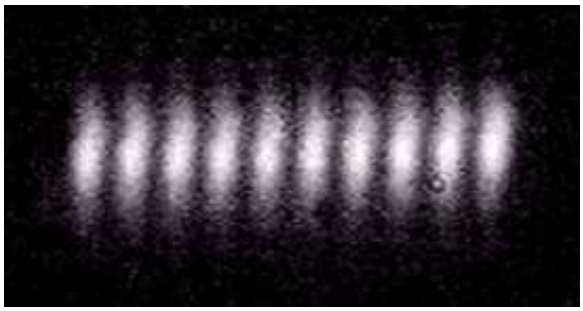

Figure 5.8: A CCD image of the tweezer beams. This image shows the full capabilities of the tweezer trap system. Ten spots are made with a spacing of approximately $10\,\mu$m. The spots are $\approx 6\,\mu$m in diameter in the small dimension and $\approx 12\,\mu$m in diameter in the long dimension. For the actual tweezer experiment, only two spots are needed to create the trap potential, but the image demonstrates the capacity of this method.

trolled through voltage controlled attenuators. The frequencies are combined on a MiniCircuits 16 way RF power combiner. The output of the combiner is sent to a MiniCircuits three watt broadband linear amplifier which drives the deflector. The experiment typically uses up to ten different frequencies at once to drive the deflector, creating ten different spots with separations determined by the frequency differences.

The first order output of the deflector passes through a 140 mm focal length achromatic lens located at the focal distance away from the deflector. This lens is the first lens of a telescope that expands the beam to a waist of 6 mm with a 700 mm focal length lens. Within the telescope beam path, the beam is superimposed with the vertical green trap through the use of a PBSC as shown in Fig. 5.7. After passing the Gradium lens it is focussed to a spot

on the atoms with a waist of $\approx 3\,\mu$m. For the tweezer trap, a sheet geometry is not needed, but a little asymmetry is useful to guarantee that the atoms do not see a weak spot in the trap. Therefore, a 1000 mm focal length cylindrical lens was placed in the telescope beam path to slightly elongate the trap in one direction yielding a spot with waists $\approx 3\,\mu$m by $\approx 6\,\mu$m. Fig. 5.8 shows an image of the tweezer beams creating a lattice potential.

5.3.2 Magnetic Trap Decompression

Before the condensate in the QUIC trap can be loaded into the optical trap, it must be moved to the center of the glass cell, which allows for better optical access. In Chap. 2, the field in the compressed trap was discussed. The compressed trap is when the field minimum is small and the gradients are high. In this configuration, the trap is suitable for evaporative cooling. A disadvantage, however, is that the trap center is located near one of the walls of the glass cell. It is possible to move the trap minimum back near the center of the chamber by lowering the current in the quadrupole pair and maintaining the current of the Ioffe coil. In this case, the gradients, especially in the radial direction, are decreased. Using a numerical simulation, a plot of the fields for this case is shown in Fig. 5.9. In the figure, for $I_I = 25\,\mathrm{A}$ and $I_Q = 7.5\,\mathrm{A}$, the field has approximate values of $B'_\rho = 71\,\mathrm{G/cm}$, $B''_z = 42\,\mathrm{G/cm^2}$ and $B_0 = 42\,\mathrm{G}$. This corresponds to trap frequencies of about $\omega_z = 2\pi\cdot 8.25\,\mathrm{Hz}$ and $\omega_z = 2\pi\cdot 12.7\,\mathrm{Hz}$. In this case, the simulation shows the trap center moving past the center position demonstrating the capability. In the experiment, the

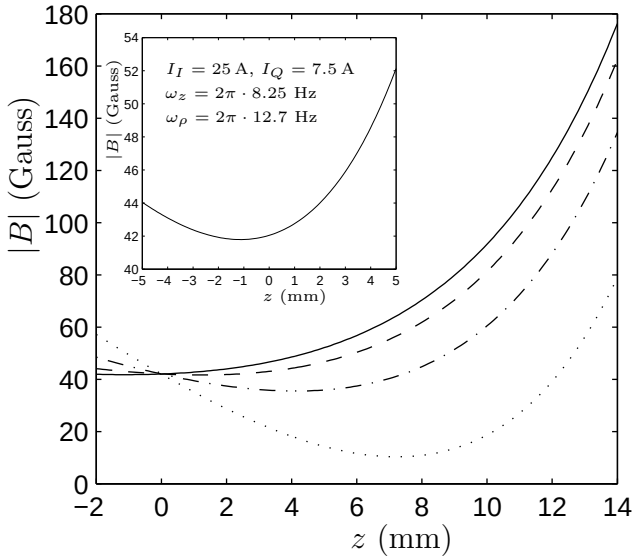

Figure 5.9: Calculated field for the uncompressed QUIC trap. Field magnitude along the z-axis is shown for different situations. In all cases, the current in the Ioffe coil is $I_I = 25\,\mathrm{A}$. The dotted curve is for quadrupole current $I_Q = 25\,\mathrm{A}$, which corresponds to the compressed trap. The dot-dashed and dashed curves correspond to $I_Q = 15\,\mathrm{A}$ and $I_Q = 10\,\mathrm{A}$, respectively. The solid curve is when $I_Q = 7.5\,\mathrm{A}$. This curve corresponds to a situation with approximate trap frequencies of $\omega_z = 2\pi \cdot 8.25$ Hz and $\omega_z = 2\pi \cdot 12.7$ Hz, with $B_0 = 42\,\mathrm{G}$. This roughly symmetric trapping minimum is near the center of the chamber. The plot inset shows a closer view of the trap minimum in the final case; clearly it has moved slightly beyond the chamber center.

same behavior is observed. The Ioffe coil is held at 28 A while the quadrupole coils are reduced to a current of roughly 8.5 A to bring the trap back to the center along the Ioffe coil axis.

In addition, several auxiliary coils are used to return the trap to the center in the two other axes. A vertically oriented levitation coil is necessary to counteract gravity. Since the trap is very weak in this configuration, gravity is strong enough to pull the trap center down. A water cooled coil located on the bottom of the middle vacuum chamber provides a magnetic gradient field for this purpose. With a current of about 8A, the coil can provide enough force on the atoms to counter gravity and return the trap to its original position in the vertical direction. The optical pumping bias coils are used to shift the magnetic trap back to the center along the quadrupole axis.

During the switch on of the QUIC trap's primary coils, it is not important to worry about kinks in the current because the atoms are hot. After evaporation, the atoms are very cold, and when decompressing the trap back to the quadrupole center it is necessary to carefully choose a current profile which will not excite the atoms. More specifically, a continuous acceleration is needed. If the acceleration is chosen to be of the form $a(t) = -A\omega^2 \sin \omega t$, with $A > 0$, this can be integrated to find the velocity $v(t) = \omega A \cos \omega t + C$ and the position $x(t) = A \sin \omega t + Ct + x_0$, where $\omega t_{\text{end}} = 2\pi$. Using the boundary values $a(0) = a(t_{\text{end}}) = 0$ and $v(0) = v(t_{\text{end}}) = 0$, yields the constants $A = (x_0 - x_{\text{end}})/2\pi$ and $C = (x_{\text{end}} - x_0)/t_{\text{end}}$, where $x_{\text{end}} = x(t_{\text{end}})$. So,

the trap center position is moved in time according to

$$x(t) = \frac{x_0 - x_{\text{end}}}{2\pi} \sin\frac{2\pi t}{t_{\text{end}}} + \frac{x_{\text{end}} - x_0}{t_{\text{end}}} t + x_0. \tag{5.8}$$

In order to actually move the atoms, the current in the quadrupole pair has to be adjusted. The position moves from the QUIC trap center at 28 A to the region of the quadrupole center at around 8.5 A. Because the current dependence is rather complicated, it was simplest to determine the positions experimentally, by varying the current settings and imaging the cloud. The current for the desired position was determined numerically from the above equation.

5.3.3 BEC in an Optical Trap

After moving the magnetic trap back to the center of the glass cell, the cloud is loaded into a gravito-optical trap. This is performed in several steps. First, the horizontal green sheet sheet is turned on below the cloud. The beam is turned on over a period of 300 ms to a power of roughly 300 mW. After the sheet is on, the cloud is compressed by "turning on" gravity. This is accomplished by turning off the levitation coil used to cancel out the effects of gravity. The coil is ramped off in 100 ms leaving a compressed cloud. Now the cloud is confined in one dimension through the combination of gravity and a repulsive sheet. In order to confine the atoms in the two remaining directions, the vertical red trap is turned on at the same time as the sheet to a power of approximately 50 mW.

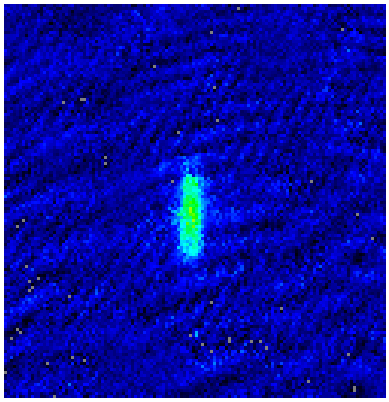

Figure 5.10: An absorption image of the condensate created in the optical trap. The image was taken 18 ms after being released from the trap. The cloud contains $\approx 2.3 \times 10^5$ atoms and has a diameter of 240 μm in the long direction and 80 μm in the short direction.

At this point the atoms are contained in both an optical trap and a magnetic trap. The magnetic trap is now ramped off to create a pure optical trap. During this process, the intensity of the red trap is lowered slightly. This provides some amount of evaporative cooling to counteract any heating that may have occurred during the shut off of the magnetic trap. The magnetic trap ramp down occurs in five steps, which decrease the current in the coils as well as adjust current in the auxiliary coils to keep cloud stationary as the fields shut off. This takes place over the course of 2.5 seconds while lowering the red trap intensity by 2 dB.

The end result of this process is a condensate in a pure optical trap. This is verified through a time of flight measurement. Fig. 5.10 shows and absorption image of the cloud after a time of flight of 18 ms. The clear asymmetry

of the cloud indicates that it is a condensate. The estimated trap frequency for the gravito-optical trap is roughly 500 Hz in the tight direction which is parallel to gravity (see Appendix A). In the other two directions, the trap frequencies are roughly 10 Hz.

5.3.4 High Frequency Optical Traps

In an effort to achieve the high trap frequencies necessary to perform the tweezer experiment, compressed sheet traps were used in both the vertical and horizontal directions. Two blue detuned sheets were used to create a trap around the atoms. Implementation along the horizontal axis was accomplished by driving the acousto-optic modulator with two frequencies to add an additional sheet. Then the sheets were compressed by decreasing the difference between the two frequencies. Along the vertical axis, an acousto-optic modulator would need to be installed and used in the same way. The only problem with this approach was that it was not possible to achieve high enough trap frequencies. An analysis using the formulas from Appendix A, with careful consideration of the experimental realities of the system reveals that at most only 5 kHz is possible. In addition, compressed sheet traps create an anti-trapping potential in the perpendicular direction that would be difficult to accurately counterbalance with a red trap.

Optical lattices provide an attractive solution to the problems associated with sheet traps. The trade-off is that individual addressability is lost. Another means to obtain high optical gradients yet retain individual address-

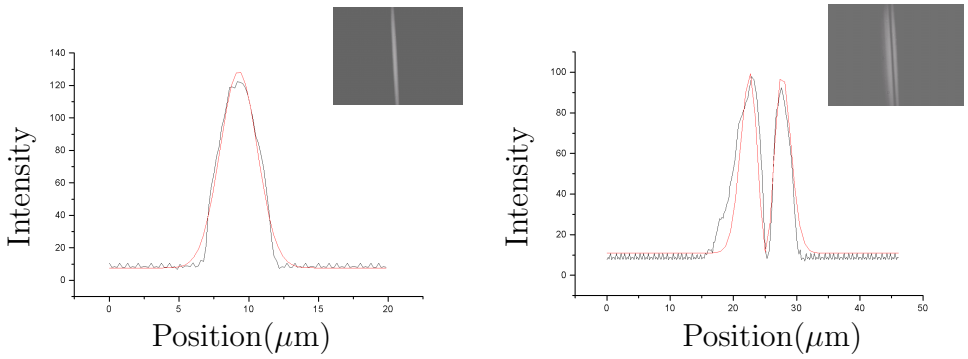

Figure 5.11: Plots of the intensity, I (in arbitrary units), as a function of position for the vertical sheet trap without (on the left) and with (on the right) the phase plate. Inset in the upper right of each plot is a CCD image of the full beam from which the profile was obtained. The red lines are fits to the data. On the left, the profile is fit to a gaussian with a waist of 2.6 μm. On the right, the profile is fit to a TEM_{01} mode with a waist of 3.6 μm.

ability of the trap is through the use of TEM_{01} mode traps. TEM_{01} mode beams have the tightly focussed spatial features of a double sheet trap, but do not suffer from the unwanted potential offset in the center.

The TEM_{01} mode beams are simple to create experimentally. Within the collimated beam path of the optical setup for the sheet traps, an anti-reflection coated window was inserted. One half of the window had an additional coating that consisted of an ≈ 6900 Å thick layer of magnesium fluoride. The thickness is such that the portion of the beam that passes through the coating receives a π phase shift. The end result is that at the focus of the beam, where the atoms are, the beam profile is no longer gaussian but rather has a dark stripe down the center. Fig. 5.11 shows CCD images of the beam profile at the focus as well as profiles of the beam quality.

The phase plate does not produce a true TEM_{01} mode beam. Fig. 5.12 shows how the phase plate affects the beam. The π phase shift changes the complex amplitude of the beam such that the gaussian profile now has a discontinuous change of sign at the origin. A true TEM_{01} has a complex amplitude of the form of a (0,1) order Hermite-Gaussian function[29]. The difference between the two is rather substantial, but each has the same dark stripe in the center of the intensity profile. This can be seen by taking the Fourier transform of the complex amplitude, as the focussing lens does, then squaring the result to obtain the intensity profile [65]. The result shows a TEM_{01} type profile with longer tails than a true TEM_{01} profile. This higher order spatial noise is most likely due to the sharp discontinuity introduced by the phase plate. This behavior is also seen in the CCD images of the beam. While the higher order spatial noise is not ideal, it does not pose a problem since it is necessarily away from the beam focus and thus away from the atoms.

The true evidence that this is an acceptable means of producing a TEM_{01} trap is that it traps atoms. After creating a condensate in the gravito-optical trap, the TEM_{01} mode trap is ramped on in two steps. First, in the horizontal direction, the trap is ramped on over a period of 100 ms a distance of 6 μm above the position of the sheet with roughly 50 mW in the beam. Then, the lower sheet is simultaneously ramped off as the TEM_{01} mode beam is turned completely on. In this fashion, a condensate of $\approx 5 \times 10^4$ atoms is loaded into the trap.

Expansion of the atoms within the trap reveal that the cloud is indeed

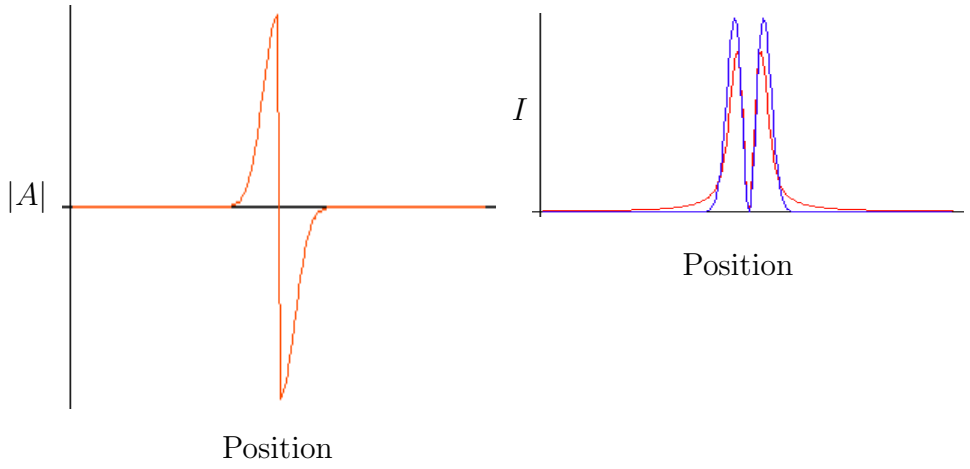

Figure 5.12: Plots of the effect of the phase plate on a gaussian beam. The phase plate gives a π phase shift to half of the beam changing the amplitude, $|A|$, as shown in the plot on the left. On the right, in red, is the square of the Fourier transform of the amplitude showing the beam intensity profile, I. For comparison, the beam profile of a true TEM_{01} mode beam of equal power is shown in blue.

a condensate. Within the trap, the condensate is two dimensional. This can be verified through the use of Eq. 5.11. Upon release, in the tight confining direction, the cloud will spread like a gaussian wavepacket since it only occupies the ground state vibrational level of the trap. A single particle gaussian wavepacket has a wavefunction given by [96]

$$\psi(x,t) = \langle x|\psi(t) = \frac{1}{\sqrt{\sqrt{\pi}(a + (i\hbar t/ma))}} e^{-\frac{x^2}{2a^2(1+(i\hbar t/ma^2))}}, \qquad (5.9)$$

where $a = \sqrt{\hbar/m\omega}$ is the harmonic oscillator length. Since the density is the wavefunction squared, it has the form

$$n(x,t) = \psi^*(x,t)\psi(x,t) = \frac{1}{\sqrt{\pi(a^2 + \hbar^2 t^2/m^2 a^2)}} e^{-\frac{x^2}{a^2(1+\hbar^2 t^2/m^2 a^4)}}. \qquad (5.10)$$

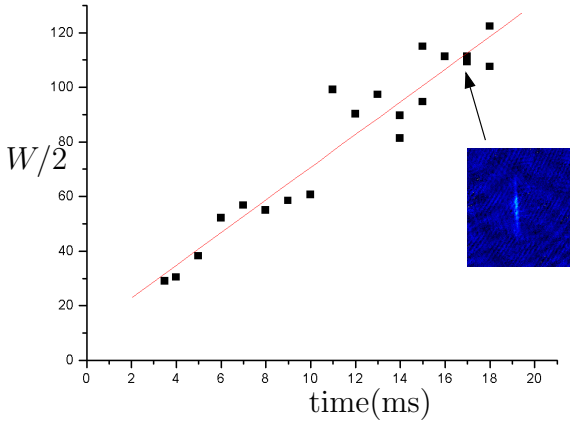

Figure 5.13: A plot of the half waist, $W/2$, of the the condensate as a function of time after release. The fit using Eq. 5.11 yields a trap frequency of 16 kHz. After optimization, higher trap frequencies have been achieved. Inset is an absorption image of the condensate for one of the data points corresponding to a time of flight of 17 ms.

This is simply a gaussian profile that has an expanding waist, described by

$$W(t) = \sqrt{2}\sqrt{\frac{\hbar}{m\omega}}\left(1 + t^2\omega^2\right)^{1/2} . \tag{5.11}$$

Fig. 5.13 shows a plot of the half waist of the density distribution as a function of time after release. The fit of the data clearly shows that the cloud expands as a two dimensional condensate. In the horizontal direction, trap frequencies as high as $\omega_{tight} = 2\pi \times 23\,\text{kHz}$ have been achieved. A similar TEM_{01} mode trap was constructed in the vertical beam path and trap frequencies as high as $\omega_{tight} = 2\pi \times 45\,\text{kHz}$ have been observed.

Loading into a crossed TEM_{01} mode trap consists of first loading the

atoms into the horizontal trap then into the vertical trap. This has been accomplished and atoms are held within the trap, but no verification that the cloud is still a condensate has been done as there is no obvious means of doing so. Since individually each trap is capable of loading a condensate, it stands to reason that a crossed trap geometry should do the same since the traps are ramped on adiabatically.

The end result of this procedure is the creation of a single condensate in a very tight trap. The optical trap holding the condensate is characterized by frequencies of 45 kHz by 16 kHz by 10 Hz. In this highly asymmetric trap, the condensate is one-dimensional as long as the atom number is below 4×10^4 (see Chap. 1 Sec. B.4). This can be verified by counting the number of atoms within the trap using the single atom counting capabilities of the experiment (see Sec. 5.3.5).

5.3.5 Single Atom Detection

In order to verify the ability of the tweezer to extract single atoms, it is necessary to detect single atoms. This feat is accomplished using an arrangement similar to that of D. Meschede [88]. The atom is placed into a weak MOT such that it is trapped and will fluoresce. The fluorescence from the atom is then collected with a large collection angle lens system. The collected light is transported to an avalanche photodiode (APD) that counts the individual photons emitted by the atom. With appropriate suppression of scattered background light, the signal to noise ratio can be large enough

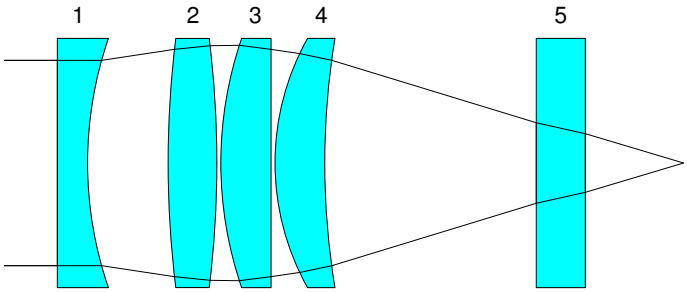

Figure 5.14: Single atom detection "super lens". The lens system consists of four lenses: 1) 40.0 mm focal length plano-concave lens, 2) 50.0 mm focal length bi-convex lens, 3) 40.0 mm focal length plano-convex lens, 4) meniscus lens with 26 mm and 78 mm radii of curvature, and 5) 5 mm thick slab of fused silica.

to distinguish the quantized fluorescence of individual atoms. In this way, a single atom can be detected.

The collection lens used in this scheme is actually a carefully chosen collection of lenses. The design is identical to that used by Meschede [97]. Four lenses, in addition to one wall of the glass cell that comprises the vacuum chamber, are appropriately spaced to create a "super lens" (see Fig. 5.14) with a solid collection angle of roughly 2% of 4π. The lens system was designed to reduce spherical abberations up to 7th order and astigmatism to 3rd order. Designed for imaging, this system is more than adequate since we are only interested in light collection. Regardless, the lens system works well for the purposes of this experiment.

The "super lens" is positioned such that the fluorescent light from the

atom is collimated. This beam is transported a distance of 80 mm from the chamber to give room to clean the beam and measure the fluorescent light. After approximately 80 mm, the beam is focused with a 60 mm achromat through a 100 μm pinhole. This reduces the amount of background scattered light. From here the beam passes through two 50 mm lenses and is focussed onto an APD to measure the fluorescence light level. To ensure that no stray light enters the beam path of the transport optics, the entire path is enclosed with black cardboard paper.

Single atoms were observed with an APD. The APD is manufactured by Perkin Elmer, model SPCM-AQR-14. The APD has an active area of 175 μm and an overall photon detection efficiency of $\approx$ 66% at 780 nm. The dark count for the APD is 50 counts per second with a maximum of 100 counts per second. The APD is capable of a mean count rate of 5 million counts per second before saturation effects start to become appreciable. The module can withstand count rates up to 15 million counts per second before damage occurs. This limit is never approached during the course of the experiment.

The APD is an extremely sensitive device that can be easily destroyed by an excessive amount of light, therefore, a series of protection devices are in place. Immediately in front of the APD is an interference filter with a 10 nm bandwidth centered at 780 nm. This filter reduces the fluorescence signal by $\approx$ 50% but reduces scattered light outside the bandwidth by roughly four orders of magnitude. Additionally, a UniBlitz shutter is in front of the APD. It only opens during the measurement of single atoms. This reduces the

possibility of stray light hitting the APD. An electronic security box was also built for additional protection. This box contains several TTL inputs to trigger a relay that disconnects the APD from its power source. The TTL inputs include a software trigger as well as photodiode signals. The photodiodes are placed on the table near the APD. Once the light level on the photodiodes increases beyond a threshold level, the protection circuit is activated.

Before the system could be used for detecting single atoms from the tweezer, it had to be tested against a known source of single atoms. This was accomplished by measuring the atom number in a weak MOT with a tiny capture volume. Previous experiments [85–87] had captured single atoms within a MOT. A similar set up was designed to measure the sensitivity of the APD and collection optics to single atom detection (SAD). The first step was to create a weak MOT with a tiny capture region.

First the magnetic field gradient of the existing MOT setup was increased. The current in the quadrupole coils was increased to 28 A, yielding field gradients of roughly 265 G/cm. To further reduce the capture region as well as weaken the trap, a different set of MOT beams were used. A dedicated SAD MOT beam was created out of the zeroth order of the lower MOT beam as described in Chap. 2. This beam is transported to the lower MOT region where it is combined with the regular lower MOT beams. This was accomplished by mixing the SAD MOT beams with the regular MOT beams on a 90%-10% beam splitter. The end result is a second set of MOT beams that have a waist of 0.5 mm and a power of approximately 0.1 mW per beam. In

addition, the repump beam for the SAD MOT was reduced. A mechanical flipper with a 1 mm aperture was placed in the repump beam path. When the SAD MOT is activated, the aperture is flipped into place reducing the repump beam to 1 mm in diameter. The reduction in size and power of the beams makes the MOT weak so that it would only capture a few atoms, but it also has the benefit of reducing the amount of scattered light that reaches the APD.

When a SAD MOT is created, the shutter protecting the APD is opened, and a recording of the count rate from the APD is made. Fig. 5.15 shows a data set from one typical experimental run. In this case, the MOT beams were tuned 3.5 MHz from the cycling transition and both the MOT beams and repump beams were operating at 20% of the full value. The plot shows the count rate obtained from the APD as a function of time. The count rate was derived by counting the number of photons for 100 ms. The plot shows the count rate every 100 ms over the entire observation of 350 seconds.

There are distinct quantized steps corresponding to an integer number of atoms within the MOT. A recording of the background count rate was made for 1 second by leaving the magnetic field gradient off, which resulted in a rate of 30,700 counts per second. Afterwards, the gradient was applied and atoms entered the trap. As an atom enters the trap, the fluorescence counting rate makes a discrete jump of approximately 11,400 counts per second. This can be seen more easily in a histogram plot of the counting rate.

Fig. 5.16 shows a histogram plot of the data set from Fig. 5.15. The

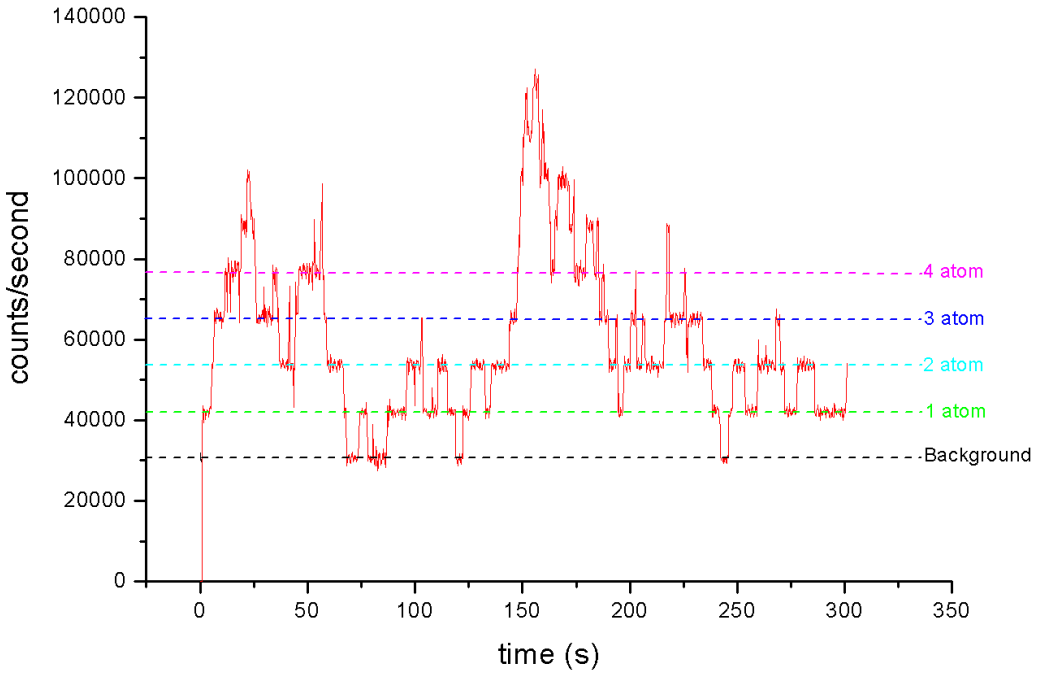

Figure 5.15: Photon count rates taken during the operation of a weak MOT. This data was taken with a MOT detuning of 3.75 MHz, MOT intensity of 20% maximum, repump intensity of 20% maximum, and a magnetic field gradient of 265 G/cm. The average background scattered light signal is 30,700 counts per second. Each atom provides an additional signal of 11,400 counts per second. The quantized levels corresponding to different numbers of atoms within the MOT are highlighted with colored lines.

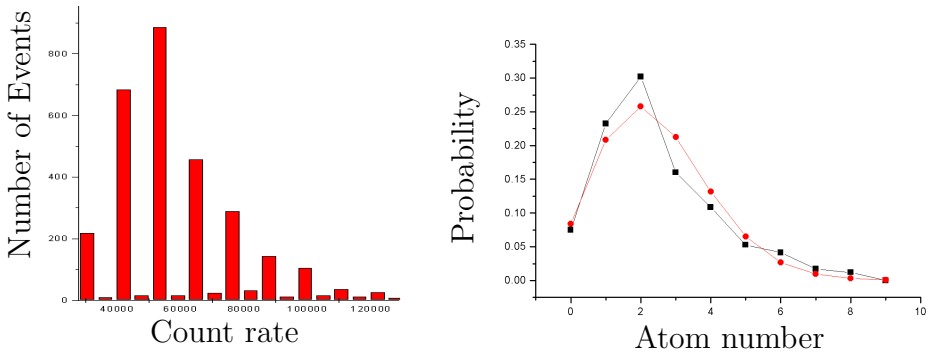

Figure 5.16: A histogram of the counts shown in Fig. 5.15. The data was sorted into a histogram with bin sizes that are half the single atom signal rate centered at the background signal rate. The plot on the right shows the fit of the histogram peaks to a poissonian distribution as would be expected for a random process such as the loading of a MOT. The poissonian fit had an average atom number of 2.475.

data was sorted into bins 5,700 counts per second wide in size, starting at the background counting rate. The histogram clearly shows distinct peaks every 11,400 counts per second that arise from an integer number of atoms in the trap. The graph also reveals the lack of signal in between the sharp peaks. A comparison of the peaks to the valleys measures the error rate of the number detection of the system. For the zero, one, and two atom cases, the correct number of atoms is determined at least 95% of the time or better.

Aside from statistics on the detection ability, the histogram can be used to analyze the statistics of atoms within the trap. The average number of atoms trapped in the MOT is found to be roughly 2.475 atoms. It is a random process by which atoms from the background vapor find the trapping

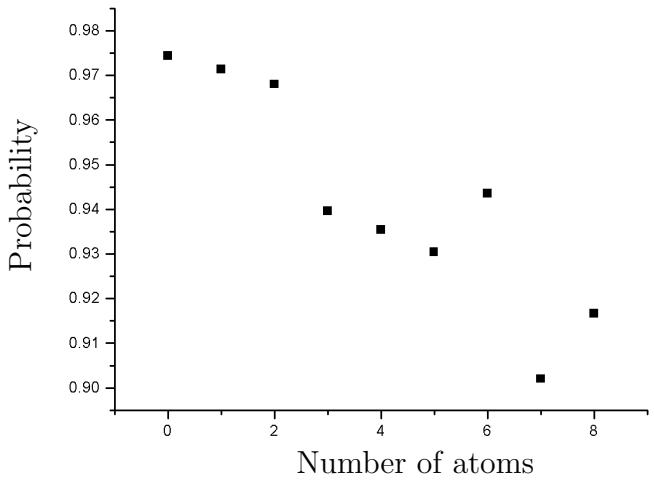

Figure 5.17: A plot of the reliability of the single atom detection system. The probability displayed is that of finding the same number of atoms on the next measurement cycle as a function of the measured atom number.

region and become trapped within the MOT. Therefore, one would expect a oissonian distribution for the atom number within the trap. Fig. 5.16 shows the probability distribution for finding atoms within the trap, as well as a fitted poissonian distribution. The fit shows good agreement between the poissonian and the actual probability distribution.

Fig. 5.17 shows the reliability of measurements made with the single atom detection system. The plot gives the probability of measuring the same number of atoms in the MOT during the next measurement cycle. As can be seen from the plot, the probability is near 97% for zero, one, or two atoms. This is useful in that if a single atom is extracted and placed in the MOT

capture region before it is turned on, there is a 97% probability that any atoms measured with the detection system are those placed in the MOT after extraction and not those loaded from background vapor or lost from the MOT. In conjunction with the error statistics obtained in the histogram, it is possible to measure a single atom and know with over 93% accuracy that it is the extracted atom.

5.4 Future Outlook

Presently, a great deal of progress has been made towards the experimental realization of the quantum tweezer for atoms. To date, it is possible to create a single, one-dimensional condensate with tight confining trap frequencies of 23 kHz and 45 kHz, of which the geometric mean is greater than the 30 kHz value used in the simulations. The weak direction is much easier to manipulate, and trap frequencies in the range of 5 Hz to 20 Hz are possible. As for the microtrap, single and multiple traps have been created and calculated trap frequencies of up to 200 Hz are possible. The detection apparatus for the single atom has been built and tested. Quantized fluorescence corresponding to an integer number of atoms within the SAD MOT has been observed, verifying the reliability of the detection scheme. Therefore, the majority of the experimental apparatus necessary to perform the experiment exists and is in place.

At this point, it should be possible to perform the experiment. A large parameter space can be explored. The tweezer trap frequency, the weak trap

frequency for the condensate, and the extraction rate are just a few of the parameters that can be adjusted to find an operating region where an integer number of atoms are extracted.

One remaining step is required before it is possible to verify that the experiment works. A method to clean the optical traps is needed. Great effort was taken to make the trapping beams as clean as possible, but fringes still exist on them. Therefore it is possible that atoms can get trapped within the fringes, leading to complications for the detection of the single extracted atom. One means of cleaning the optical trap is to use a magnetic orbiting potential (MOP). The MOP consists of a low current quadrupole field offset from the center of the optical trap through the use of the auxiliary coils. The magnetic trap center is made to circle around the optical trap by adjusting the current in these coils. In this manner, the magnetic trap can circle around the optical trap, removing atoms from the fringes of the optical trap. Afterwards, the magnetic trap is turned off and the "mopped" atoms fall away. The end result is the single atom in the optical trap.

After the successful extraction of a single atom has been performed, it is still necessary to demonstrate that the atom is in the ground state of the trap. This can easily be done by allowing the atom to tunnel out of the tweezer. The extracted atom is actually in a metastable state. The repulsive trap provides a barrier against a free space continuum. Therefore, it is always possible for the atom to tunnel through the tweezer wall. To minimize this possibility, the tweezer depth will be increased after extraction to reduce the

tunnelling possibility. By lowering the well depth of the tweezer trap, it is possible to observe the tunnelling rate of atoms out of the trap. Since the tunnelling rate depends on the barrier height, the rate will be dependent on the vibrational state the atom occupies. Therefore, the tunnelling rate will be a good means of verifying occupation of the ground state vibrational level.

The remaining hurdles to extracting a single atom and verifying that it is in the ground state are relatively small and should be overcome in a short amount of time, barring any catastrophe to the experiment. Once completed, a variety of experiments using single, neutral atoms are possible. Rabi oscillations can be performed by two tweezer traps close together. This leads in nicely to experiments in quantum computation where spatially localized qubits are formed by two adjacent wells [98]. With this scheme, a phase gate is easily implemented and with Rabi oscillations forms a complete set of operators that can perform any quantum algorithm [16]. Along another direction, experiments in atom entanglement and multiparticle atom interferometry will be possible [99]. These experiments would require the addition of a high magnetic field coil to reach a Feschbach resonance in ^{87}Rb which is necessary to adjust the scattering length of the rubidium atoms [100]. The aforementioned experiments do not form an exhaustive list. Any experiment requiring a single, well-defined quantum state is now possible.

Appendices

Appendix A

Optical Dipole Traps

A.1 Overview

Optical dipole traps are used extensively throughout the experiments described in this dissertation. The use of optical potentials to trap atoms has been around for quite some time and been written about extensively (see Ref. [101, 102] for additional reviews). Due to the extensive use of optical potentials in this dissertation, it is useful to have handy a listing of the necessary formulas to calculate traps depths and frequencies.

A.2 The Dipole Potential

One of the major tools used in the laboratory to control the behavior of atoms is the optical dipole trap. The optical dipole trap is based on the fact that alkali atoms have a large electric dipole moment. If a laser is directed onto one of these atoms, the atom behaves as a dipole interacting with the electric field of the laser. This creates an energy shift known as the AC Stark shift or light shift. In addition, if the frequency of the laser is near the transition frequency for the atom, there is a resonant enhancement to the light shift.

Alkali metal atoms have an electronic configuration such that they have

one electron in their outer shell while all the inner shells are filled. This configuration leads them to behave similarly to a hydrogen atom. As a very good approximation, the motion of the single electron in the presence of an ac electric field can be treated as a damped, driven harmonic oscillator. In this model, an electron with charge q and mass m is attached to the nucleus via a spring with constant k, damping b, and is driven with a force $F_o = qE_o$ from an incident light field. The electron moves in the same direction as the polarization of the incident electric field which is taken to be the x direction in this case. The electron obeys the following equation of motion [32]

$$m\ddot{x} + b\dot{x} + kx = qE_o e^{i\omega t}\,, \tag{A.1}$$

or in a more transparent formulation

$$\ddot{x} + \gamma\dot{x} + \omega_o^2 x = \frac{qE_o}{m} e^{i\omega t}\,, \tag{A.2}$$

where τ, the lifetime of the atomic transition, is $1/\gamma$, and $\omega_o^2 = k/m$ is the square of the transition frequency. For the case of rubidium, the natural linewidth is $\gamma \approx 2\pi \times 6\,\mathrm{MHz}$ and $\omega_o \approx 2\pi \times 384\,\mathrm{THz}$ making this system a driven, under-damped harmonic oscillator.

A closer look at Eq. A.2 sheds some light on the behavior of the atom in the presence of a light field. The solution of the equation contains two parts: a transient solution that dies off on a time scale of order $1/\gamma$, and a steady state solution that mimics the driving force. The transient is [103]

$$x_{trans}(t) = x_o e^{\frac{-\gamma t}{2}} \left(\cos(\omega_1 t) + \frac{\gamma}{2\omega_o} \sin(\omega_1 t) \right)\,, \tag{A.3}$$

where $\omega_1 = \sqrt{\omega_o^2 - \gamma^2/4}$. Since in this under-damped system $\omega_o >> \gamma$, we can say $\omega_1 \approx \omega_o$ and neglect the second term in Eq. A.3. Therefore,

$$x_{trans}(t) = x_o e^{\frac{-\gamma t}{2}} \cos(\omega_o t)\,, \tag{A.4}$$

is a transient behavior that oscillates at the transition frequency, but dies away on a timescale on the order of the excited state lifetime. The transient behavior is initiated by the initial interaction of the laser and quickly dies away. This quickly dying behavior is of little use here.

The steady state part of the solution has the form [32]

$$x_{ss}(t) = \frac{qE_o e^{i\omega t}}{m(\omega_o^2 - \omega^2 + i\gamma\omega)}\,. \tag{A.5}$$

The real part of the solution, which describes the motion of the electron, is [103]

$$x_{ss}(t) = \frac{qE_o/m}{\sqrt{(\omega_o^2 - \omega^2)^2 + \omega^2\gamma^2}} \cos(\omega t - \delta)\,. \tag{A.6}$$

This shows that the electron oscillates at the same frequency as the driving force with a phase shift

$$\delta = \tan^{-1}\left(\frac{\omega\gamma}{\omega_o^2 - \omega^2}\right)\,, \tag{A.7}$$

determined by the detuning of the laser from the atomic resonance transition and an amplitude determined by both the driving force as well as the detuning.

Of interest here is the phase shift between the driving electric field and the oscillating dipole [104]

$$p(t) = qx_{ss}(t) = \frac{q^2E_o/m}{\sqrt{(\omega_o^2 - \omega^2)^2 + \omega^2\gamma^2}} \cos(\omega t - \delta)\,. \tag{A.8}$$

As the detuning grows, the phase shift approaches 0 or π depending on whether the detuning is to the low side or high side respectively of the atomic transition. Therefore, for detunings that are to the low side, or red, of the transition, the dipole will oscillate in phase whereas for detuning to the high side, or blue, of the transition, the dipole will oscillate out of phase. The energy of a dipole in an electric field is given by [101]

$$U = -\frac{1}{2}\langle p(t) \cdot E(t) \rangle \,. \tag{A.9}$$

From Eq. A.8 and Eq. A.9 it is clear that the dipole potential is proportional to the electric field squared. Therefore, since the intensity of a light field, I, is also proportional to the electric field squared, we see that

$$U \propto -\frac{I}{\Delta} \,, \tag{A.10}$$

where $\Delta = \omega - \omega_{\mathrm{o}}$ is the detuning from the atomic resonance transition. If the laser field has a spatially varying intensity distribution, the potential will vary spatially and the force felt by the atom will be

$$F(x) = -\nabla U(x) \propto -\frac{\nabla I}{\Delta} \,. \tag{A.11}$$

So for detunings to the red of the atomic transition, there is a decrease in potential energy in areas of higher intensity leading to an attractive force whereas for detunings to the blue side of the atomic transition higher intensity creates a potential barrier and a repulsive force.

A.3 Gaussian Beams

It is now clear that light will create a potential for an atom. To make use of that fact, it is important to know what beam profiles are possible and hence what trapping potentials can be formed. Since light is an electromagnetic wave, Maxwell's equations in free space are an appropriate starting point [105].

$$\boldsymbol{\nabla} \cdot \mathbf{E} = 0 \tag{A.12}$$

$$\boldsymbol{\nabla} \cdot \mathbf{B} = 0 \tag{A.13}$$

$$\boldsymbol{\nabla} \times \mathbf{B} = \epsilon_o \frac{\partial \mathbf{E}}{\partial t} \tag{A.14}$$

$$\boldsymbol{\nabla} \times \mathbf{E} = -\mu_o \frac{\partial \mathbf{B}}{\partial t} \tag{A.15}$$

From here, it is possible to solve for the wave equation that governs electromagnetic waves. By taking the curl of Eq. A.12, one arrives at [29]

$$\nabla^2 E - \frac{1}{c^2} \frac{\partial^2 E}{\partial t^2} = 0, \tag{A.16}$$

where $c = 1/(\epsilon_o \mu_o)^{1/2}$ is the speed of light in vacuum.

Let us assume that the solution to Eq. A.16 is a wave of the following form

$$E(\mathbf{r}, t) = A(\mathbf{r}) e^{i\omega t} e^{i\phi(\mathbf{r})}\,, \tag{A.17}$$

where $A(\mathbf{r})$ and $\phi(\mathbf{r})$ are a spatially varying amplitude and phase. Substituting Eq. A.17 into Eq. A.16 yields the Helmholz equation [65],

$$\left(\nabla^2 + k^2\right) A(\mathbf{r}) = 0\,, \tag{A.18}$$

where $k = \omega/c$ is the wavenumber of the electromagnetic wave. The solution to the Helmholz equation gives the amplitude of a wave travelling in the z direction with frequency ω, and some transversely varying amplitude and phase. If the assumption is made that the beam varies slowly in the z direction compared to the transverse directions, then one arrives at the paraxial equation

$$\nabla_t^2 \mathrm{A} - 2\mathrm{ik}\frac{\partial \mathrm{A}}{\partial \mathrm{z}} = 0, \tag{A.19}$$

where ∇_t^2 is the transverse part of the Laplacian operator. This result is based off the assumption that $\frac{\partial^2 A}{\partial z^2}$ is small compared to all the other derivatives. This assumption holds for beams that are either focussing or defocussing with a cone angle of less than $\approx 30^{\mathrm{o}}$ [29], as is the case for all the beams discussed in this dissertation.

A.3.1 Gaussian Traps

There are a variety of different solutions to the paraxial wave equation. The most commonly used is the gaussian beam solution. In this case, the solution takes the form [29, 65]

$$A(\overrightarrow{r}) = A_o \frac{W_o}{W(z)} e^{-\frac{\rho^2}{W^2(z)}} e^{ikz + ik\frac{\rho^2}{2R(z)} - i\zeta(z)}, \tag{A.20}$$

where $W(z)$ and $R(z)$ are the $1/e^2$ waist and wavefront radius of curvature, respectively. The gaussian beam will focus at some point $z = 0$ where it is characterized by a waist

$$W_{\mathrm{o}} = \left(\frac{\lambda_L z_{\mathrm{o}}}{\pi}\right)^{1/2} \tag{A.21}$$

and a wavefront radius of curvature, R, that is infinite. Away from this position, the waist and wavefront curvature will change according to

$$W^2(z) = W_{\rm o}^2 \left(1 + \left(\frac{z}{z_{\rm o}}\right)^2\right) \tag{A.22}$$

and

$$R(z) = z\left(1 + \left(\frac{z_{\rm o}}{z}\right)^2\right). \tag{A.23}$$

The distance $z_{\rm o}$ is known as the Rayleigh length and is the distance where the waist has increased to $\sqrt{2}W_{\rm o}$. $\zeta(z)$ is a phase retardation effect known as the Guoy effect, but is of little concern here.

Suppose that a laser operates at a wavelength λ_L. At the focus, it has a gaussian beam profile of

$$I(\rho, z) = I_{\rm o} e^{-2\rho^2/W_{\rm o}^2(z)} \tag{A.24}$$

where the prefactor

$$I_{\rm o} = \frac{2P}{\pi W_{\rm o}^2} \tag{A.25}$$

is the peak intensity.

As was shown earlier, laser light creates a potential for the atoms such that $U \propto I$. Therefore, the light shift creates a potential of the form [106]

$$U(\rho, z) = U_{\rm o}(z) e^{-2\rho^2/W_{\rm o}^2(z)}, \tag{A.26}$$

where the factor

$$U_{\rm o}(z) = \frac{\hbar\gamma^2 I_{\rm o}(z)}{24 I_{sat}} \left[\left(\frac{1}{\delta_{1/2}} + \frac{2}{\delta_{3/2}}\right) - g_F m_F \sqrt{1-\epsilon^2}\left(\frac{1}{\delta_{1/2}} - \frac{2}{\delta_{3/2}}\right)\right]. \tag{A.27}$$

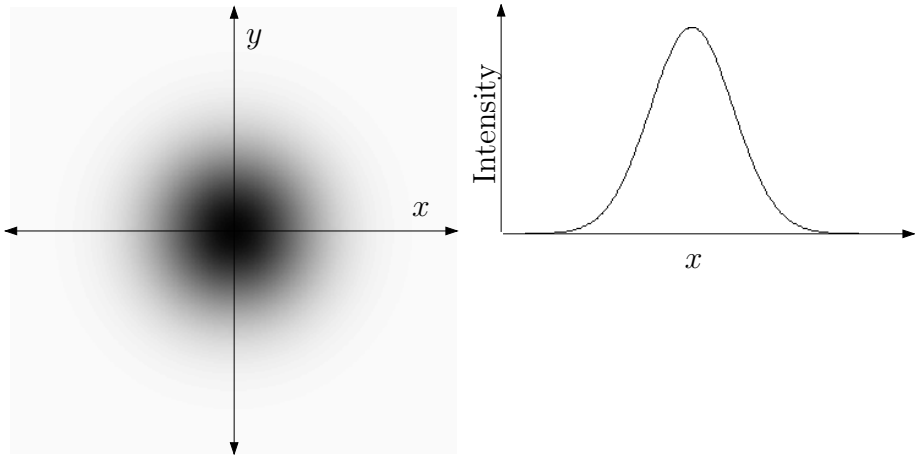

Figure A.1: The intensity distribution of a gaussian beam. The image on the left is a two dimensional density plot of the intensity distribution. The right-hand image is a one dimensional intensity profile of the beam taken along the x axis.

Here, ϵ is a measure of the polarization. In the case of linear polarization, as in the experiment, $\epsilon = 1$, therefore we can ignore the last term in the potential. The saturation intensity is given by

$$I_{sat} = \frac{2\pi^2 \hbar c \gamma}{3\lambda^3}\,. \tag{A.28}$$

$I_{sat} = 3.58\,\mathrm{mW/cm^2}$ for ^{87}Rb. $I_{\mathrm{o}}(z)$ is the peak intensity of the beam given by Eq. A.25.

In addition to knowing the trap depth U_{o}, the trap frequencies associated with the beam are important. If we do a Taylor series expansion of the potential function about the minimum of the trap, we find

$$U(x) = U_c + \left.\frac{\partial U}{\partial x}\right|_{x_{min}} (x - x_{min}) + \frac{1}{2!}\left.\frac{\partial^2 U}{\partial x^2}\right|_{x_{min}} (x - x_{min})^2 + \ldots \tag{A.29}$$

Typical Gaussian Trap Values		
Value	$\lambda_L = 532$nm	$\lambda_L = 1064$nm
$U_{\rm o}$	$20.0\,E_{rec}$	$46.5\,E_{rec}$
ω_{rad}	NA	$2\pi \times 900\,\mathrm{Hz}$
ω_{axial}	NA	$2\pi \times 10\,\mathrm{Hz}$

Table A.1: Typical values for a gaussian beam trap. The values were calculated for a beam with a waist of $10\,\mu$m in both directions at the focus and a power of 10 mW. Due to the fact that blue detuned beams create a repulsive potential, alone they do not make traps and are not included in this table.

Since we are looking at the minimum, the linear term vanishes. By equating the quadratic term to the potential of a harmonic oscillator, $U_{SHO} = \frac{1}{2}m\omega^2x^2$, a trap frequency can be calculated. At the focus of a gaussian beam, in the direction perpendicular to the optical axis, the radial trap frequency is

$$\omega_{rad} = \sqrt{\frac{4U_{\rm o}}{mW_{\rm o}^2}}. \tag{A.30}$$

Since the waist grows away from the focus, the intensity decreases and the potential changes correspondingly. So in addition to a radial trap, the atoms also experience an axial trap. In an analogous manner to the radial trap frequency, the axial trap frequency along the optical axis is

$$\omega_{axial} = \sqrt{\frac{2U_{\rm o}}{mz_{\rm o}^2}}. \tag{A.31}$$

Table A.1 gives trap values for typical beam parameters. Using the above equations, it is trivial to scale these values for any particular beam parameters.

A.3.2 Sheet Traps

More exotic traps can be created by altering the ratio of the two beam waists with respect to each other. By elongating the waist in one direction, it is possible to form sheets. As with other dipole traps, sheet traps come in two flavors depending on the direction of the detuning from resonance.

A.3.2.1 Red Sheets

Detuning red of resonance creates an attractive sheet trap. These traps are identical to a regular gaussian trap except for the extreme aspect ratios available. The trap depths and trap frequencies are calculated in the same way, except that the waist $W(z)$ is now replaced by the geometric mean of the two waists, $\sqrt{W_x(z)W_y(z)}$, when calculating the potential depth.

A.3.2.2 Blue Sheets

Blue detuned sheets can create more interesting trap geometries. Since blue detuned traps are repulsive in nature, sheets of light can be used to create confining boundaries. The work done throughout this dissertation relied on two main configurations for the blue detuned sheet traps. One uses a single sheet and gravity to create a trap for the atoms. Another variety utilizes two sheets and confines atoms between the two repulsive barriers.

Gravity-Optical Traps Gravity-optical traps are simple yet effective traps for neutral atoms. In this configuration, a single blue detuned sheet is used

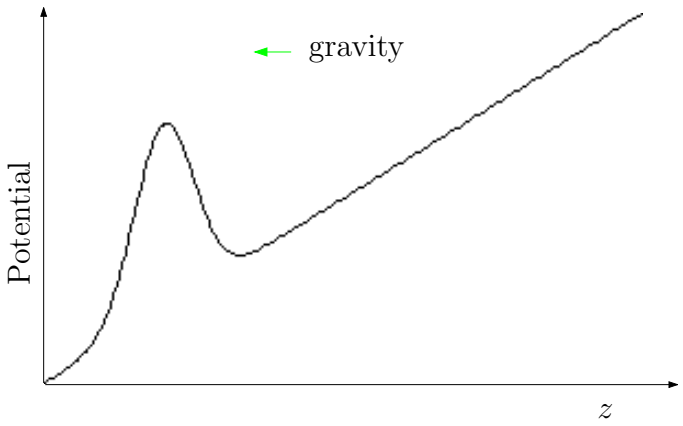

Figure A.2: One dimensional potential profile for a gravity-optical sheet trap. The gaussian bump on the left of the image is the potential of the blue detuned sheet while gravitation potential energy gives rise to the linear slope. The direction of gravity is denoted by the green arrow.

to trap the atoms. Gravity provides the additional potential required to keep the atoms localized. Fig. A.2 shows a one dimensional profile of the potential created by a sheet and gravity.

The analytical form of the potential of a gravity-optical trap is given by

$$U(x) = U_{\mathrm{o}} e^{-\frac{2x^2}{W_x^2}} + mgx\,. \tag{A.32}$$

Such a potential does not lend itself well to analytical solutions for the well depth and trap frequency. Therefore it is necessary to resort to numerical methods to calculate these quantities. Table A.2 gives calculated values for a gravity-optical sheet trap using typical values for beam size and intensity.

Typical Gravity-Optical Trap Values		
Parameters	Well Depth	ω
$W_x = 2\,\mu$m,$W_y = 100\,\mu$m	$999\,E_{rec}$	$2\pi \times 996\,$Hz
$W_x = 5\,\mu$m,$W_y = 100\,\mu$m	$395\,E_{rec}$	$2\pi \times 586\,$Hz
$W_x = 5\,\mu$m,$W_y = 200\,\mu$m	$195\,E_{rec}$	$2\pi \times 567\,$Hz
$W_x = 10\,\mu$m,$W_y = 100\,\mu$m	$190\,E_{rec}$	$2\pi \times 386\,$Hz

Table A.2: Typical values for a gravity-optical trap. The trap values were numerically calculated with a beam power of 1 W.

Compressed Sheets Trap The other trap configuration for blue detuned sheets is two sheets enclosing a sample of atoms. Fig. A.3 illustrates such a geometry. By adjusting the intensity of the beams as well as the distance between the two sheets, different trap depths and frequencies are possible, as will be shown.

The potential formed by two blue sheets is given by

$$U(x,y) = U_o e^{-\frac{2y^2}{W_y^2}} (e^{-\frac{2(x+d/2)^2}{W_x^2}} + e^{-\frac{2(x-d/2)^2}{W_x^2}}) , \tag{A.33}$$

where W_x and W_y are the waists of the beams in each of the respective directions and d is the distance between the sheets. When d is much larger than the waist in that direction, the two sheets act as "hard walls" and the system behaves in a manner similar to a billiard (see Chapter 3). This situation is useful for trying to control the dynamics of the particle within the trap.

As the distance between the sheets is reduced, the beams start to overlap. At that point, the width of the beams is comparable to the distance between the beams, in which case the trap starts to become harmonic. By

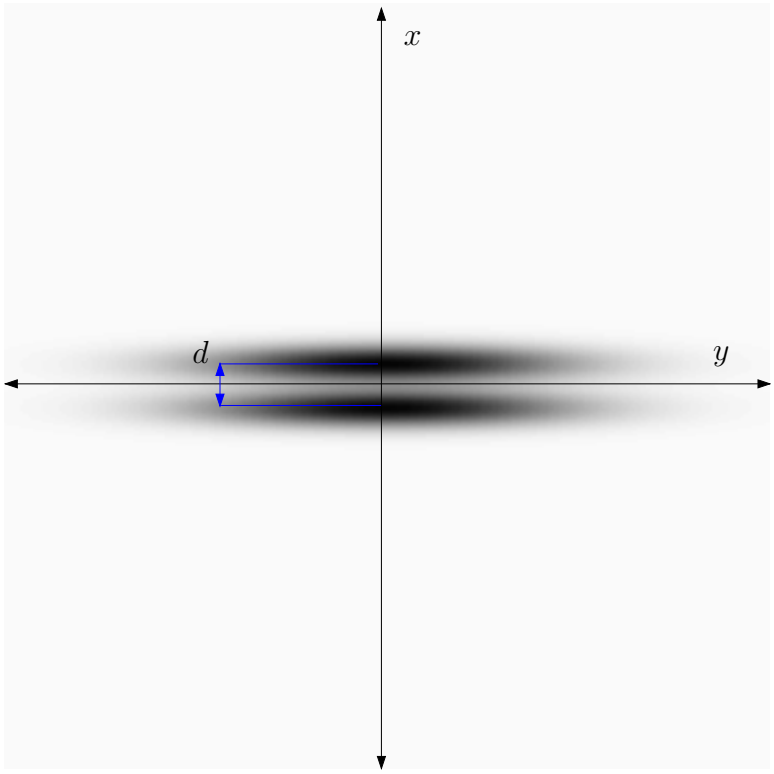

Figure A.3: A two dimensional plot of the intensity distribution of two compressed sheets. The distance between the center of each sheet is d.

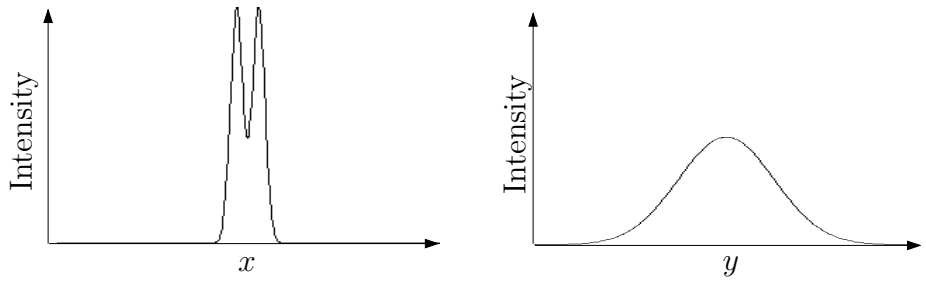

Figure A.4: One dimensional intensity profile plots of two compressed sheets. The image on the left shows the potential well created by the compressed sheets taken along the x axis at $y = 0$ in Fig. A.3. The image on the right show the intensity profile of the trap along the y axis at the potential minimum of the trap located at $x = 0$ in Fig. A.3.

performing a Taylor series analysis of the trapping potential, the trap frequency of two blue detuned sheets is

$$\omega = \sqrt{\frac{8U_o}{mW_x^2}}\sqrt{e^{-\frac{d^2}{2W_x^2}}(\frac{d^2}{W_x^2} - 1)}\ . \tag{A.34}$$

The maximum trap frequency possible in this configuration is

$$\omega_{max} = \frac{2}{e^{3/4}}\sqrt{\frac{4U_o}{mw_x^2}} \sim 0.94\sqrt{\frac{4U_o}{mw_x^2}} \tag{A.35}$$

which occurs at a sheet separation of $d = \sqrt{3}W$.

At this point it is important to notice the fact that in the compressed sheets trap, there is an offset created by the overlap of the two sheets. This offset decreases in value as one moves away from the center of the trap giving rise to an anti-trapping potential orthogonal to the trapping potential. The anti-trapping potential can be characterized by a frequency of

$$\omega_{axial} = \sqrt{\frac{8U_o}{mw_y^2}e^{-\frac{d^2}{2w_x^2}}}. \tag{A.36}$$

Typical Compressed Sheets Trap Values	
Well Depth	$223\,E_{rec}$
ω_{max}	$2\pi \times 5\,\mathrm{kHz}$
ω_{axial}	$2\pi \times 177\,\mathrm{Hz}$

Table A.3: Typical compressed sheets trap values. The trap values were calculated for sheets with waists of $W_x = 5\,\mu$m and $W_y = 100\,\mu$m and a power of 1W in each beam.

At the optimum separation distance of $d = \sqrt{3}W$, this takes a value of

$$\omega_{axial,max} = \sqrt{\frac{8U_o}{e^{3/2}mw_y^2}}. \tag{A.37}$$

Typical trap values are given in Table A.3.

A.3.3 Standing Wave Optical Traps

Another common means of making an optical trap for atoms is to create an optical lattice. Optical lattices are created by superimposing two counter-propagating laser beams of the same frequency. Because of the laser's coherence properties, they will interfere with each other creating the typical standing wave pattern shown in Fig. A.5.

To generalize this situation a bit more, imagine two laser beams with identical wavelength λ_L, beam size, and power intersecting each other at an angle θ between the optical axes of the two beams. In such a situation, an interference pattern is formed perpendicular to the bisector of the angle between the beams. The interference pattern produces an intensity modulation of the form

$$I(x) = I_\mathrm{o} \sin^2(k_L x) \tag{A.38}$$

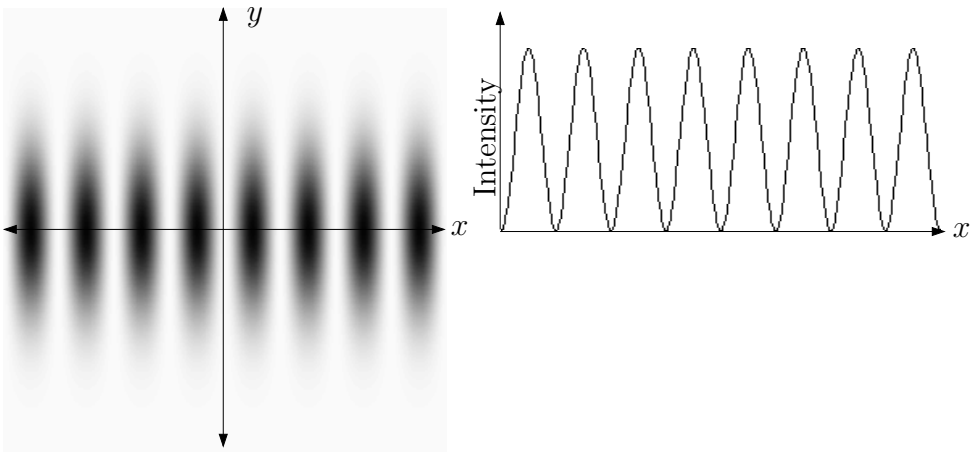

Figure A.5: The intensity distribution of a standing wave trap. The image on the left is a two dimensional intensity plot of an optical lattice. The righthand image is a one dimensional intensity profile taken from the center of the two dimensional plot.

where the effective wavenumber is given by

$$k_L = \frac{2\pi \sin(\theta/2)}{\lambda_L} \,. \tag{A.39}$$

As can be seen, the intensity varies sinusoidally from zero to a peak intensity of $I_\mathrm{o} = 8P/\pi W^2$ which is four times that of an individual beam with a periodicity given by

$$d = \frac{\lambda_L}{2\sin(\theta/2)} \,. \tag{A.40}$$

From this intensity pattern, a potential lattice is created. The potential has the form

$$U(x) = U_\mathrm{o} \sin^2(k_L x) \tag{A.41}$$

Typical Standing Wave Trap Values		
Value	$\lambda = 532$nm	$\lambda = 1064$nm
$U_{\rm o}$	$321\,E_{rec}$	$744\,E_{rec}$
ω_{axial}	$2\pi \times 198\,$kHz	$2\pi \times 150\,$kHz
ω_{radial}	NA	$2\pi \times 722\,$Hz

Table A.4: Typical values for a standing wave trap. The values were calculated for a two identical counter propagating gaussian beams with waists $W_{x,y} = 50\,\mu$m. Each beam has a power of 1 W.

where, from Eq. A.27,

$$U_{\rm o} = \frac{\hbar\gamma^2 I_{\rm o}(z)}{24 I_{sat}} \left(\frac{1}{\delta_{1/2}} + \frac{2}{\delta_{3/2}} \right). \tag{A.42}$$

As before, it is important to know the trap frequencies available by using an optical lattice. Since it is possible to get spatial variations of the intensity pattern over a smaller distance (it is possible to get periodicities as small as $\lambda_L/2$), it is easier to achieve high trap frequencies. By using the same method as before, one can find that the trap frequency in the well of an optical lattice is

$$\omega_{axial} = \sqrt{\frac{2U_{\rm o}k_L^2}{m}}\,. \tag{A.43}$$

The trapping frequency in the radial direction is the same as that of a gaussian beam. Clearly, by having the two beams directly counter-propagating, and thereby having the largest wavenumber, one can get a very large trap frequency. Table A.4 lists trap values in an optical lattice for typical parameters.

A.3.4 TEM01 Mode Traps

The gaussian beam solution to the paraxial equation (Eq. A.19) is not the only solution. In fact, the gaussian beam is a subset of a larger set of solutions to the paraxial equation called the Hermite-Gaussian beam solutions. They have the same paraboloidal wavefronts as the gaussian beam, but they have an additional modulation to the intensity distribution.

The complex amplitude of the Hermite-Gaussian beam takes the form [29, 65]

$$A_{l,m}(x,y,z) = A_{l,m}\left(\frac{W_o}{W(z)}\right) G_l\left[\frac{\sqrt{2}x}{W(z)}\right] G_m\left[\frac{\sqrt{2}x}{W(y)}\right] e^{ikz+ik\frac{\rho^2}{2R(z)}-i(l+m+1)\zeta(z)} \tag{A.44}$$

where

$$G_l(u) = H_l(u)e^{-\frac{u^2}{2}}, \tag{A.45}$$

is the Hermite-Gaussian function of order l and $H_l(u)$ is the Hermite polynomial of order l. It is possible to find Hermite polynomials using the recursive relation

$$H_{l+1}(u) = 2uH_l(u) - 2lH_{l-1}(u) \tag{A.46}$$

and

$$H_0(u) = 1 \tag{A.47}$$

$$H_1(u) = 2u\,. \tag{A.48}$$

By taking the square of the complex amplitude, one finds the intensity

distribution for the beam. This leads to

$$I_{l,m}(x,y,z) = |A_{l,m}|^2 \left(\frac{W_o}{W(z)}\right)^2 G_l^2\left[\frac{\sqrt{2}x}{W(z)}\right] G_m^2\left[\frac{\sqrt{2}x}{W(y)}\right]. \tag{A.49}$$

If we look at the zeroth order Hermite-Gaussian beam, the gaussian beam solution stands out at the lowest order member of the Hermite-Gaussian family of solutions.

Of particular interest for our experiment is not the zeroth order solution, but rather the first order solution. By letting $l = 0$ and $m = 1$, the intensity pattern will be given by

$$I_{0,1}(x,y,z) = \frac{P}{\pi W_x(z) W_y(z)} \frac{8x^2}{W_x^2(z)} e^{-\frac{2x^2}{W_x^2(z)}} e^{-\frac{2y^2}{W_y^2(z)}}. \tag{A.50}$$

This mode is also known as a TEM_{01} mode. Fig. A.6 shows plots of the intensity distribution for a TEM_{01} mode. It should be noted that the TEM_{01} mode has a dark line down the center of the beam. This is important in that it does not suffer from the anti-trapping potential that plagues the compressed sheets trap.

The potential created by the TEM_{01} beam takes the form

$$U(x,y,z) = 4U_{\mathrm{o}}(z) \frac{x^2}{W_x^2(z)} e^{-\frac{2x^2}{W_x^2(z)}} e^{-\frac{2y^2}{W_y^2(z)}}, \tag{A.51}$$

where U_{o} is the potential depth of a gaussian beam having the same power and waist as given above. The potential has a value of zero at the center of the beam and increases to peaks located a distance $W_x/\sqrt{2}$ away. This gives the trap a well depth of

$$U_{max} = \frac{2}{e} U_{\mathrm{o}}. \tag{A.52}$$

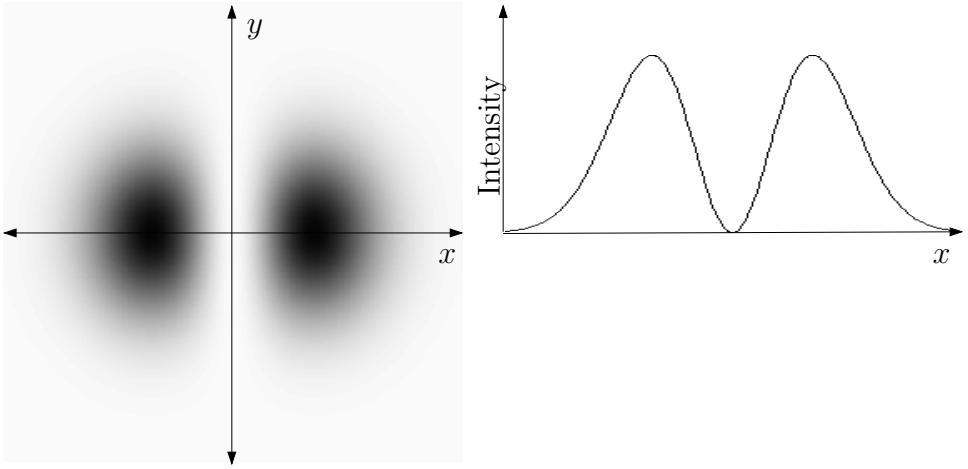

Figure A.6: The intensity distribution of a TEM_{01} mode beam. The image on the left is a two dimensional intensity plot of a TEM_{01} mode beam. The righthand image is a one dimensional intensity profile taken along the x axis of the two dimensional plot.

Along the same lines, the trap frequencies associated with a TEM_{01} can be calculated. At the focus of a TEM_{01} beam, the trap has a frequency of

$$\omega_x(y) = \sqrt{\frac{8U_o(y)}{W_x^2 m}}\,. \tag{A.53}$$

This value varies along the length of the dark line due to the changing intensity in the y direction. It should be noted that this is a factor of $\sqrt{2}$ better than two sheets compressed together. Typical values for a TEM_{01} mode trap are given in Table A.5.

Typical TEM_{01} Mode Trap Values	
U_{max}	$1470\,E_{rec}$
ω_x	$2\pi \times 41.9\,\mathrm{kHz}$

Table A.5: Typical values for a TEM_{01} mode trap. The calculation assumed a beam with a power of $2W$, waists $W_x = 100\,\mu\mathrm{m}$ and $W_y = 2\,\mu\mathrm{m}$, and $\lambda_L = 532\,\mathrm{nm}$.

A.4 Spontaneous Emission

Care must be taken when using optical dipole traps. In addition to the potential the light creates, there is also the chance of the atom absorbing a photon and making a transition to the excited state. It will then decay back down to the ground state by spontaneously emitting a photon. To conserve momentum, the atom receives a kick when it both absorbs and emits the photon. The photon is spontaneously emitted in all directions leading to a net change in momentum of zero, but the atom does undergo a random walk in momentum space which leads to a heating of the entire sample. Therefore, it is important to reduce spontaneous emission as it can become a substantial source of heating.

Earlier in Eq. A.8 it was shown that the electric field induces a dipole moment in the atom. This can also be written as [104]

$$p = \alpha E\,, \tag{A.54}$$

where α is the atomic polarizability. Therefore

$$\alpha = \frac{q^2}{m}\frac{1}{\omega_{\mathrm{o}}^2 - \omega^2 - i\omega\gamma}\,. \tag{A.55}$$

It can be shown that the absorbed power becomes [101]

$$P_{abs} = \langle \dot{p} \cdot E \rangle = \frac{\omega}{\epsilon_o c} \mathrm{Im}(\alpha) \mathrm{I} \, . \tag{A.56}$$

This leads to a scattering rate of

$$R_{scat} = \frac{P_{abs}}{\hbar\omega} = \frac{1}{\hbar\epsilon_o c} \mathrm{Im}(\alpha) \mathrm{I} \, . \tag{A.57}$$

By substituting Eq. A.55 into Eq. A.57, the scattering rate becomes

$$R_{scat} = \frac{\omega\gamma q^2}{m\hbar\epsilon_o c} \frac{I}{(\omega_o^2 - \omega^2)^2 + \omega^2\gamma^2} \, . \tag{A.58}$$

In the limit that the detuning is small compared to the atomic transition frequency, this reduces to

$$R_{scat} = \frac{\pi q^2 I}{2\omega_o m\hbar\epsilon_o c} \frac{\gamma/2\pi}{(\omega_o - \omega)^2 - (\gamma/2)^2} \, , \tag{A.59}$$

which is a Lorentzian profile centered at ω_o with a full width at half maximum of $\gamma/2$. The important thing to note is that the scattering rate falls off as the inverse of the detuning squared.

A more rigorous calculation that takes into account the quantum mechanical nature of the atom can be performed and is found to be [43]

$$R_{scat} = \frac{\gamma}{2} \frac{s_o}{1 + s_o + (\frac{2\Delta}{\gamma})^2} \, , \tag{A.60}$$

where

$$s_o = 2\frac{\Omega^2}{\gamma^2} = \frac{I}{I_{sat}} \, . \tag{A.61}$$

I_{sat} is the saturation intensity given in Eq. A.28. Again, this shows that the scattering rate depends inversely on the detuning squared. Therefore, with sufficient detuning, it is possible to create substantial dipole potentials while having a negligible number of spontaneous emission events.

Appendix B

Bose-Einstein Condensates

B.1 Overview

A Bose-Einstein condensate is a system of bosons at a density and temperature such that the phase space density of the system is of order one or greater. This produces a macroscopic system that shows quantum behavior. This was achieved in dilute gases of alkali metals for the first time in 1995 [9–11]. This procedure has now become rather common place and is routinely performed in our lab (see Chap. 2 and Chap. 5 for a description of how condensates are made), therefore some basic theory on condensates is useful. Many nice review articles have been written on the subject [107, 108] as well as several books [109, 110]. Therefore, I will only go into detail on the relevant information for understanding the experiment. This appendix gives some of the basic theoretical aspects of condensates in one, two, and three dimensions with emphasis on experimentally useful quantities.

B.2 Three Dimensional Bose-Einstein Condensates

To begin, let us assume that we have a dense cloud of cold atoms. For an ideal gas of bosons in a three dimensional harmonic trap, the cloud exhibits

a phase transition when the following condition is met

$$\rho\lambda_{dB}^3 \geq \zeta(3/2) \approx 2.612\ldots\ , \tag{B.1}$$

where $\lambda_{dB} = h/\sqrt{2\pi m k_B T}$ is the de Broglie wavelength and $\zeta(3/2)$ the Riemann zeta function [111]. This condition corresponds to the atoms being cold enough that their de Broglie wavelengths are comparable to the inter-atom spacing. Therefore the wavefunctions collapse onto one another and a significant proportion of the population can be described by a single wavefunction. Algebraic manipulation of Eq. B.1 leads to a formula for the temperature at which condensation starts to occur, also known as the critical temperature, T_c. For a harmonically trapped gas this is

$$T_c = \frac{\hbar\bar{\omega}}{k_B}\left(\frac{N}{\zeta(3/2)}\right)^{1/3}\ . \tag{B.2}$$

Here $\bar{\omega}$ is the geometric mean of the trap frequencies. In our experiment $\bar{\omega} \approx 2\pi \times 90\,\mathrm{Hz}$, so with 2 million atoms, $T_c \approx 500\mathrm{nK}$.

As the temperature is lowered, more atoms accumulate in the ground state increasing the number of atoms within the condensate. By integrating the number of atoms in the ground state using the Bose distribution, one can show that the condensate fraction increases as [110]

$$N_o = N\left[1 - \left(\frac{T}{T_c}\right)^3\right]\ . \tag{B.3}$$

Therefore, by cooling down far enough it is possible to reach a regime where the condensate is almost pure, i.e. the thermal background fraction is very small.

The condensate is a many-body system where the particles within the condensate interact with each other through a contact interaction described by $U_o\delta(\mathbf{r}-\mathbf{r}')$ where $U_o = 4\pi\hbar^2 a_{scat}/m$. a_{scat} is the scattering length of the atoms which is approximately 5.3 nm for ^{87}Rb. A common approximation to make is the Hartree-Fock ansatz in which the many-body system is a product of single particle states. Using this mean field approach to analyze the system, the Gross-Pitaevskii equation (GP equation),

$$\left(-\frac{\hbar^2}{2m}\nabla^2 + V(\mathbf{r}) + g_{3D}|\psi(\mathbf{r})|^2\right)\psi(\mathbf{r}) = \mu_{3D}\psi(\mathbf{r})\,, \tag{B.4}$$

can be derived to describe the evolution of the wavefunction $\psi(\mathbf{r})$ [109, 110]. The constant $g_{3D} = U_o$ is used to conform with standard notation. Here, μ_{3D} is the chemical potential of the condensate and the wavefunction is normalized such that the integral of $|\psi(\mathbf{r})|^2$ over space is equal to the number of atoms, N, in the condensate. This is valid for dilute gases such as in the experiment. With this equation, it is possible to analyze the condensate in terms of experimentally useful quantities.

B.2.1 Thomas-Fermi Approximation

Exact solutions to the Gross-Pitaevskii equation are rather hard to come by due to the nonlinear term in the Hamiltonian. Fortunately, some of the basic characteristics of a condensate can easily be calculated using the Thomas-Fermi approximation. The approximation is valid for condensates with large atom number and/or high mean field. The Thomas-Fermi approximation consists of assuming that the kinetic energy is negligible compared to

the mean field energy and the potential energy and removing that term from the GP equation. In which case, the result is

$$\left(V(\mathbf{r}) + g3D|\psi(\mathbf{r})|^2\right)\psi(\mathbf{r}) = \mu_{3D}\psi(\mathbf{r}) \tag{B.5}$$

leading to

$$n(\mathbf{r}) = |\psi(\mathbf{r})|^2 = \frac{\mu_{3D} - V(\mathbf{r})}{g_{3D}} \tag{B.6}$$

where $n(\mathbf{r})$ is the density. We can define the boundary of the cloud as the point where the chemical potential is equal to the potential energy of the trap. For a three dimensional harmonic trapping potential, the boundaries become

$$R_i^2 = \frac{2\mu}{m\omega_i^2} \tag{B.7}$$

in each of the trapping directions. The density distribution of the condensate is a paraboloid with radii in each direction given by Eq. B.7.

A useful quantity is the chemical potential, which can be found in terms of easily measured quantities such as the atom number and the trap frequencies. The total number of atoms in the condensate is equal to the integrated density in Eq. B.6. Using relation B.7 to remove the cloud radii, the chemical potential becomes

$$\mu_{3D} = \frac{15^{2/5}}{2}\left(\frac{Na_{scat}}{\bar{a}}\right)^{2/5}\hbar\bar{\omega}\,, \tag{B.8}$$

where $\bar{\omega}$ is the geometric mean of the trapping frequencies and $\bar{a} = \sqrt{\hbar/m\bar{\omega}}$ is the geometric mean of the harmonic oscillator lengths. For our experiment, with an almost pure condensate in the QUIC trap, we have roughly 10^6 atoms

giving a chemical potential $\mu_{3D} \approx 2.52 \times 10^{-30}\mathrm{J} \simeq 183\mathrm{nK} \cdot k_B$. The cloud has a spatial extent of $\mathrm{R}_{rad} = 5\,\mu\mathrm{m}$ and $R_{ax} = 50\,\mu\mathrm{m}$.

Another important quantity to know is the three body recombination rate. This will determine the lifetime of the condensate. At the high densities associated with condensates, there arises the possibility of three atoms colliding at the same time. When this happens, two of the atoms can form a molecule with the third carrying away the excess energy. The molecules leave the condensate while the highly energetic atom stays in the trap, heating the condensate.

A realistic calculation of the lifetime due to three body losses can be made. The probability for three bodies to collide scales as the density squared. The losses can be modelled by the rate equation

$$\frac{\mathrm{dN}}{\mathrm{dt}} = -k_3 N \langle n^2 \rangle \,, \tag{B.9}$$

where k_3 is the three body recombination rate constant which for ^{87}Rb is $1.81^{-29}\mathrm{cm}^6/\mathrm{s}$ [112]. Here, $\langle n^i \rangle = 1/N \int n^{i+1}\,\mathrm{dV}$ is the weighted average density. From this rate equation, the lifetime of the condensate is given as

$$\tau_3 = \frac{1}{k_3 \langle n^2 \rangle} \,. \tag{B.10}$$

In the case of a cloud trapped in a harmonic potential, the average squared density can be calculated, yielding [112]

$$\langle n^2 \rangle = \frac{15^{4/5}}{168\pi^2} \left(\frac{m\bar{\omega}}{\hbar\sqrt{a_{scat}}} \right)^{12/5} N^{4/5} \,. \tag{B.11}$$

For the condensates made in the QUIC trap, $\langle n^2 \rangle \approx 1.76 \times 10^{28}\,\mathrm{cm}^{-6}$ giving rise to a time constant $\tau_3 \approx 3.1\,\mathrm{s}$.

B.3 Two-Dimensional Condensates

It is possible to study condensates in lower dimensions. This is accomplished by altering the trap geometry such that the trapping frequencies in either one or two of the directions is much greater than that of the remaining directions. In such a configuration, the condensate will show behavior that is either two-dimensional or one-dimensional in nature [95].

In order to create a two-dimensional condensate, it is necessary to "freeze out" the dynamics in one of the dimensions. This can be accomplished by increasing the trapping frequency, ω_t, in one direction so that $\hbar\omega_t \geq \mu_{3\mathrm{D}}$. With the energy level spacings in the tight confining direction much greater than the chemical potential, the condensate is only allowed to undergo zero point oscillations in that direction, effectively reducing the dimensionality of the system. It should be noted that an equivalent formulation of the condition for two-dimensionality is that the healing length of the condensate, $\xi = 1/\sqrt{4\pi n a_{scat}}$, is greater than the radius of the condensate in the tight confining direction.

Since the chemical potential of the condensate depends on the number of atoms within the condensate, the two-dimensionality criteria puts a restriction on the number of atoms that can be in a two-dimensional condensate within a given trapping potential. Starting with

$$\hbar\omega_t \geq \mu_{3\mathrm{D}}\,, \tag{B.12}$$

a little algebra yields

$$N_{2\mathrm{D}} \leq \sqrt{\frac{32\hbar}{225ma^2}}\sqrt{\frac{\omega_t^3}{\omega_\perp^4}}\,, \tag{B.13}$$

where $\omega_\perp = \sqrt{\omega_x\omega_y}$ is the geometric mean of the trapping frequencies in the two weakly confining directions [95]. It is clear that in order to have as many atoms as possible in a two-dimensional condensate, it is important to have the highest tight trapping frequency achievable and the weakest possible confinement in the other two directions.

The three dimensional GP equation has to be reformulated for a two-dimensional system in order to model the behavior of this new, lower dimensional system. Lowering the dimension of the GP equation is a straight forward process [113]. The assumption is made that the wavefunction is of the form

$$\psi(x,y,z) = \phi(x,y)\left(\frac{m\omega_z}{\pi\hbar}\right)^{1/4} e^{-\frac{m\omega_z}{2\hbar}z^2}\,, \tag{B.14}$$

where $\phi(x,y)$ is the two-dimensional condensate wavefunction. This solution is placed into Eq. B.4 and the z dimension is integrated out. The result,

$$\left(-\frac{\hbar^2}{2m}\nabla_{x,y}^2 + V(x,y) + g_{2D}|\phi(x,y)|^2\right)\phi(x,y) = \mu_{2D}\phi(x,y)\,, \tag{B.15}$$

is the two-dimensional form of the GP equation where $g_{2D} = (\frac{m\omega_z}{2\pi\hbar})^{1/2}g_{3D}$ is the two-dimensional coupling factor and μ_{2D} is the two-dimensional chemical potential.

As before, it is possible to simplify the two-dimensional GP equation by making the Thomas-Fermi approximation. In an analogous manner to the

three dimensional case, the chemical potential for a two-dimensional condensate can be derived with the result

$$\mu_{2D} = (8\pi)^{1/4} \left(\frac{3}{8}\right)^{1/2} \left(\frac{N a_{scat}}{a_z}\right)^{1/2} \hbar\bar{\omega}_{2D} \,. \tag{B.16}$$

Here, a_z is the harmonic oscillator length in the tight confining direction and $\bar{\omega}_{2D}$ is the geometric mean of the trapping frequencies in the two weak directions. For a two-dimensional condensate containing $\approx 5\times10^4$ atoms trapped in a 20 kHz TEM_{01} mode trap with weak trap frequencies of 10 Hz, the chemical potential is $\mu_{2D} \approx 5.16 \times 10^{-31}\,\mathrm{J} = 37.5\,\mathrm{nK}\cdot\mathrm{k_B}$.

Three body losses still remain a concern. The rate equation remains the same, the only difference is the average squared density. Recalculation of this quantity leads to

$$\langle n^2 \rangle = \frac{9N}{32\sqrt{3}\pi} \frac{1}{a_{scat}} \frac{1}{a_z} \frac{1}{\bar{a}_\perp^4} \,. \tag{B.17}$$

where $\bar{a}_\perp$ is the geometric mean of the harmonic oscillator lengths in the two weak directions. For the two-dimensional condensate mentioned previously, $\langle n^2 \rangle \approx 5.1 \times 10^{28}\,\mathrm{cm}^{-6}$ leading to a lifetime of $\tau_3 \approx 1\,\mathrm{s}$.

B.4 One-Dimensional Condensates

Not surprisingly, it is possible to reduce the dimension of the condensate further by increasing one of the weak trapping frequencies to a large enough value. If the two tight confining trap frequencies are great enough such that the chemical potential is less than the energy level spacings of the harmonic trap

in both directions, the condensate will be forced into zero point oscillations in those directions. A mathematical formulation of this condition is

$$\hbar\omega_y, \hbar\omega_z \geq \mu_{3D}, \tag{B.18}$$

where y and z are taken as the tight confining directions. This criteria on the dimensionality of the condensate leads to the restriction on the number of atoms that may be in a one-dimensional condensate residing in a particular trap [95]

$$N_{1D} \leq \sqrt{\frac{32\hbar}{225ma^2}}\sqrt{\frac{\omega_\perp}{\omega_x^2}}\,. \tag{B.19}$$

Here, $\omega_\perp$ is the geometric mean of the tight confining trap frequencies and ω_x is the weak trap frequency.

The two-dimensional GP equation must be reformulated for a one-dimensional condensate. This is done in the same way that the two-dimensional GP equation was formulated. Since the wavefunction is reduced to zero point oscillations in two dimensions, the assumption is made that the wavefunction has the form

$$\phi(x,y) = \varphi(x)\left(\frac{m\omega_y}{\pi\hbar}\right)^{1/4} e^{-\frac{m\omega_y}{2\hbar}y^2}\,, \tag{B.20}$$

where $\varphi(x)$ is the one-dimensional many-body wavefunction. This form is substituted into the two-dimensional GP equation and the y dimension is integrated out. This yields the following one-dimensional GP equation

$$\left(-\frac{\hbar^2}{2m}\frac{\partial^2}{\partial x^2} + V(x) + g_{1D}|\varphi(x)|^2\right)\varphi(x) = \mu_{1D}\varphi(x)\,, \tag{B.21}$$

where $g_{1D} = g_{2D}(\frac{m\omega_y}{2\pi\hbar})^{1/2} = g_{3D}\frac{m\omega_\perp}{2\pi\hbar}$ is the one-dimensional coupling constant and μ_{1D} is the one-dimensional chemical potential

This one-dimensional GP equation can be simplified with the Thomas-Fermi approximation. By doing this, the chemical potential can be calculated, yielding

$$\mu_{1D} = \left(\frac{9}{32}m\omega_x^2 g_{1D}^2 N^2\right)^{1/3} . \tag{B.22}$$

For a one-dimensional condensate contained in a harmonic trap with frequencies of $2\pi \times 30\,\mathrm{kHz}$, $2\pi \times 30\,\mathrm{kHz}$, and $2\pi \times 3\,\mathrm{Hz}$, the chemical potential is $\mu_{1D} \approx 2.76 \times 10^{-31}\,\mathrm{J} = 20\,\mathrm{nK} \cdot \mathrm{k_B}$.

Following a similar procedure as before, the three body recombination lifetime can be calculated. For a one-dimensional condensate in a harmonic trap, the average squared density is

$$\langle n^2 \rangle = \frac{3}{35\pi^2}\sqrt[3]{\frac{3}{2}}\frac{1}{a_\perp^4}\left(\frac{a_\perp^2}{a_{scat}a_x^4}\right)^{2/3} N^{4/3}\,, \tag{B.23}$$

where $a_\perp$ is the geometric mean of the harmonic oscillator lengths in the tight confining directions and a_x is the harmonic oscillator length in the weak direction. For the aforementioned one-dimensional condensate, $\langle n^2 \rangle \approx 5.56 \times 10^{27}\,\mathrm{cm}^{-6}$, which yields a lifetime of $\tau \approx 10\,\mathrm{s}$.

Bibliography

[1] Nobel Prize Committee. Nobel Prize in physics anouncement, 1997.

[2] Nobel Prize Committee. Nobel Prize in physics anouncement, 2001.

[3] E. Raab, M. Prentiss, A. Cable, S. Chu, and D. Pritchard. Trapping of neutral-Sodium atoms with radiation pressure. *Phys. Rev Lett.*, 59:2631, 1987.

[4] J. R. Gardner, R. A. Cline, J. D. Miller, D. J. Heinzen, H. M. J. M. Boesten, and B. J. Verhaar. Collisions of doubly spin-polarized, ultracold Rubidium 85 atoms. *Phys. Rev. Lett.*, 74:3764, 1995.

[5] J. J. McClelland, R. E. Scholten, E. C. Palm, and R. J. Celotta. Laser focussed atomic deposition. *Science*, 262:877, 1993.

[6] M. Kasevich and S. Chu. Atomic interferometry using stimulated Raman transitions. *Phys. Rev. Lett.*, 67:181, 1991.

[7] A. Clairon, C. Salomon, S. Guellati, and W. D. Phillips. Ramsey resonance in a Zacharias fountain. *Europhys. Lett.*, 16:165, 1991.

[8] M. A. Kasevich, E. Riis, S. Chu, and R. G. Devoe. RF spectroscopy in an atomic fountain. *Phys. Rev. Lett.*, 63:612, 1989.

[9] K. B. Davis, M.-O. Mewes, M. R. Andrews, N. J. van Druten, D. S. Durfee, D. M. Kurn, and W. Ketterle. Bose-Einstein condensation in a gas of Sodium atoms. *Phys. Rev. Lett.*, 75:3969, 1995.

[10] M. H. Anderson, J. R. Ensher, M. R. Matthews, C. E Wieman, and E. A. Cornell. Observation of Bose-Einstein condensation in a dilute atomic vapor. *Science*, 269:198, 1995.

[11] C. C. Bradley, C. A. Sackett, and R. G. Hulet. Evidence of Bose-Einstein condensation in an atomic gas with attractive interactions. *Phys. Rev. Lett.*, 75:1687, 1995.

[12] F. L. Moore, J. C. Robinson, C. Bharucha, P. E. Williams, and M. G. Raizen. Observation of dynamical localization in atomic momentum transfer: A new testing ground for quantum chaos. *Phys. Rev. Lett.*, 73:2974, 1994.

[13] J. C. Robinson, C. Bharucha, F. L. Moore, R. Jahnke, G. A. Georgakis, Q. Niu, M. G. Raizen, and B. Sundaram. Study of quantum dynamics in the transition from classical stability to chaos. *Phys. Rev. Lett.*, 74:3963, 1995.

[14] M. G. Raizen, J. Koga, B. Sundaram, Y. Kishimoto, H. Takuma, and T. Tajima. Stochastic cooling of atoms using lasers. *Phys. Rev. A*, 58:4757, 1998.

[15] Nobel Prize Committee. Nobel Prize in physics anouncement, 1984.

[16] M. A. Nielsen and I. L. Chuang. *Quantum Computation and Quantum Information*. Cambridge University Press, 2000.

[17] R. B. Diener, B. Wu, M. G. Raizen, and Q. Niu. Quantum tweezer for atoms. *Phys. Rev. Lett.*, 89, 2002.

[18] D. A. Steck. *Quantum Chaos, Transport, and Decoherence in Atom Optics*. PhD thesis, The University of Texas at Austin, 2001.

[19] D. Steck. Rubidium 87 D line data. This document can be found online at `http://george.ph.utexas.edu/~dsteck/alkalidata/index.html`.

[20] D. Steck. Cesium D2 line data. This document can be found online at `http://george.ph.utexas.edu/~dsteck/alkalidata/index.html`.

[21] B. G. Klappauf. *Experimental Studies of Quantum Chaos with Trapped Cesium*. PhD thesis, The University of Texas at Austin, 1998.

[22] W. H. Oskay. *Atom Optics Experiments in Quantum Chaos*. PhD thesis, The University of Texas at Austin, 2001.

[23] B. Gutierrez-Medina. *Quantum Transport and Atomic Motion Control Using Light*. PhD thesis, The University of Texas at Austin, 2004.

[24] W. Wohlleben, F. Chevy, K. Madison, and J. Dalibard. An atom faucet. *Eur. Phys. J. D*, 15:237, 2001.

[25] M. C. Fischer. *Atomic Motion in Optical Potentials*. PhD thesis, The Univeristy of Texas at Austin, 2001.

[26] A. Chambers, R. K. Fitch, and B. S. Halliday. *Basic Vacuum Technology*. Institute of Physics Publishing, 1998.

[27] T. Esslinger, I. Bloch, and T. W. Hansch. Bose-Einstein condensation in a quadrupole-Ioffe-configuration trap. *Phys. Rev. A*, 58:R2664, 1998.

[28] T. Esslinger. Private communication.

[29] A. E. Siegman. *Lasers*. University Science Books, 1986.

[30] K. B. MacAdam, A. Steinbach, and C. Wieman. A narrow-band tunable diode laser system with grating feedback, and a saturated absorption spectrometer for Cs and Rb. *Am. J. Phys.*, 60:1098, 1992.

[31] C. E. Wieman and L. Hollberg. Using diode lasers for atomic physics. *Rev. Sci. Instrum.*, 62:1, 1991.

[32] W. Demtroder. *Laser Spectroscopy*. Springer, 1998.

[33] P. G. Pappas, M. M. Burns, D. D. Hinshelwood, M. S. Feld, and D. E. Murnick. Saturation spectroscopy with laser optical pumping in atomic Barium. *Phys. Rev. A*, 21:1995, 1980.

[34] F. Schreck. *Mixtures of Ultracold Gases: Fermi Sea and Bose-Einstein Condensate of Lithium Isotopes*. PhD thesis, École Normale Supérieure, 2002.

[35] T. P. Meyrath. Inexpensive mechanical shutter and driver for optics experiments. This documnet can be found online at `http://george.ph.utexas.edu/~meyrath/papers/`.

[36] T. P. Meyrath. An analog current controller design for laser diodes. This documnet can be found online at `http://george.ph.utexas.edu/~meyrath/papers/`.

[37] D. Pritchard. Cooling neutral atoms in a magnetic trap for precision spectroscopy. *Phys. Rev. Lett.*, 51:1336, 1983.

[38] W. D. McCormick. Private communication.

[39] T. P. Meyrath and F. Schreck. A laboratory control system for cold atom experiments. This document can be found online at `http://george.ph.utexas.edu/~control`.

[40] J. Dalibard and C. Cohen-Tannoudji. Laser cooling below the doppler limit by polarization gradients - simple theoretical models. *J. Opt. Soc. Am. B*, 6:2023, 1989.

[41] P. J. Ungar, D. S. Weiss, S. Chu, and E. Riis. Optical molasses and multilevel atoms - theory. *J. Opt. Soc. Am. B*, 6:2058, 1989.

[42] H. F. Hess. Evaporaive cooling of magnetically trapped and compressed spin-polarized Hydrogen. *Phys. Rev. B*, 34:3476, 1986.

[43] H. J. Metcalf and P. van der Straten. *Laser Cooling and Trapping.* Springer, 1999.

[44] W. Ketterle and N. J. van Druten. Evaporative cooling of trapped atoms. *Ad. At. Mol. Opt. Phys.*, 37:181, 1996.

[45] O. J. Luiten, M. W. Reynolds, and J. T. M. Walraven. Kinetic theory of the evaporative cooling of a trapped gas. *Phys. Rev. A*, 53:381, 1996.

[46] R. Resnick, D. Halliday, and K. S. Krane. *Physics*, volume 2. John Wiley & Sons, Inc., 4 edition, 1992.

[47] Y. Castin and R. Dum. Bose-Einstein condensates in time dependent traps. *Phys. Rev. Lett.*, 77:5315, 1996.

[48] U. Ernst, J. Schuster, F. Schreck, A. Marte, A. Kuhn, and G. Rempe. Free expansion of a Bose-Einstein condensate from an Ioffe-Pritchard magnetic trap. *Appl. Phys. B*, 67:719, 1998.

[49] M. C. Gutzwiller. *Chaos in Classical and Quantum Mechanics.* Springer-Verlag, 1990.

[50] L. A. Bunimovich. *Funct. Anal. Appl.*, 8:254, 1974.

[51] H. E. Lehtihet and B. N. Miller. Numerical study of a billiard in a gravitational field. *Physica D*, 21:93, 1986.

[52] D. Egolf. Equilibrium regained: From nonequilibrium chaos to statistical mechanics. *Science*, 287:101, 2000.

[53] G. Zaslavsky. From Hamiltonian chaos to Maxwell's demon. *Chaos*, 5:4, 1995.

[54] R. A. Jalabert, H. U. Baranger, and A. D. Stone. Conductance fluctuations in the ballistic regime: A probe of quantum chaos? *Phys. Rev. Lett.*, 65:2442, 1990.

[55] C. M. Marcus, A. J. Rimberg, R. M. Westervelt, F. P. Hopkins, and A. C. Gossard. Conductance fluctuations and chaotic scattering in ballistic microstructures. *Phys. Rev. Lett.*, 69:506, 1992.

[56] H.-J. Stockmann and J. Stein. Quantum chaos in billiards studied by microwave absorption. *Phys. Rev. Lett.*, 64:2215, 1990.

[57] E. Doron, U. Smilansky, and A. Frenkel. Experimental demonstration of chaotic scattering of microwaves. *Phys. Rev. Lett.*, 65:3072, 1990.

[58] S. Sridhar. Experimental observation of scarred eigenfunctions of chaotic microwave cavities. *Phys. Rev. Lett.*, 67:785, 1991.

[59] V. Milner, J. L. Hanssen, W. C. Campbell, and M. G. Raizen. Optical billiards for atoms. *Phys. Rev. Lett.*, 86, 2001.

[60] N. Fiedman, A. Kaplan, D. Carasso, and N. Davidson. Observation of chaotic and regular dynamics in atom-optic billiards. *Phys. Rev. Lett.*, 86:1518, 2001.

[61] P. H. Richter, H.-J. Scholz, and A. Wittek. A breathing chaos. *Nonlinearity*, 3:45, 1990.

[62] B. N. Miller and K. Ravishankar. Stochastic modeling of a billiard in a gravitational field: Power law behavior of Lyanpunov exponents. *J. Stat. Phys.*, 53:1299, 1988.

[63] T. Szeredi and D. A. Goodings. Classical and quantum chaos of the wedge billiard. i. classical mechanics. *Phys. Rev. E*, 48:3518, 1993.

[64] N. Friedman, L. Khaykovich, R. Ozeri, and N. Davidson. Compression of cold atoms to very high densities in a rotating-beam blue-detuned optical trap. *Phys. Rev. A*, 61:031403, 2000.

[65] B. E. A. Saleh and M. C. Teich. *Fundamentals of Photonics*. John Wiley and Sons, Inc., 1991.

[66] N. Friedman, A. Kaplan, and N. Davidson. Acousto-optic scanning system with very fast nonlinear scans. *Opt. Lett.*, 25:1762, 2000.

[67] B. G. Klappauf, W. H. Oskay, D. A. Steck, and M. G. Raizen. Quantum chaos with Cesium atoms: Pushing the boundaries. *Physica D*, 131:78, 1999.

[68] A. Kastberg, W. D. Phillips, S. L. Rolston, R. J. C. Spreeuw, and P. S. Jessen. Adiabatic cooling of Cesium to 700nK in an optical lattice. *Phys. Rev. Lett.*, 74:1542, 1995.

[69] V. Vuletic, C. Chin, A. J. Kerman, and S. Chu. Degenerate raman sideband cooling of trapped Cesium atoms at very high atomic densities. *Phys. Rev. Lett.*, 81:5768, 1998.

[70] S. L. Winoto, M. T. DePue, N. E. Bramall, and D. S. Weiss. Laser cooling at high density in far-detuned optical lattices. *Phys. Rev. A*, 58:R19, 1999.

[71] S. van der Meer. Stochastic cooling and the accumulation of antiprotons. *Rev. Mod. Phys.*, 57:689, 1985.

[72] G. Zhang, J. Shen, J. Dai, and H. Zhang. Cooling charged particles in a Paul trap by feedback control. *Phys. Rev. A*, 60:704, 1999.

[73] T. C. Weinacht, J. Ahn, and P. H. Bucksbaum. Controlling the shape of the quantum wavefunction. *Nature*, 397:233, 1999.

[74] J. Ye, D. W. Vernooy, and H. J. Kimble. Trapping of single atoms in cavity QED. *Phys. Rev. Lett*, 83:4987, 1999.

[75] N. V. Morrow, S. K. Dutta, and G. Raithel. Feedback control of atomic motion in an optical lattice. *Phys. Rev. Lett*, 88:093003, 2002.

[76] J. Guo, P. R. Berman, B. Dubetsky, and G. Grynberg. Recoil-induced resonances in nonlinear spectroscopy. *Phys. Rev. A*, 46:1426, 1992.

[77] J. Guo and P. R. Berman. Recoil-induced resonances in pump-probe spectroscopy including effects of level degeneracy. *Phys. Rev. A*, 47:1428, 1993.

[78] P. D. Lett, R. N. Watts, C. E. Tanner, S. L. Rolston, W. D. Phillips, and C. I. Westbrook. Optical molasses. *J. Opt. Soc. Am. B*, 5:2084, 1989.

[79] M. C. Fischer, A. M. Dudarev, B. Gutierrez-Medina, and M. G. Raizen. FM spectroscopy in recoil-induced resonances. *J. Opt. B. Quantum Semiclass. Opt.*, 3:279, 2001.

[80] J. Y. Courtois, G. Grynberg, B. Lounis, and P. Verkerk. Recoil-induced resonances in cesium: An atomic analog to the free-electron laser. *Phys. Rev. Lett.*, 72:3017, 1994.

[81] D. R. Meacher, D. Boiron, H. Metcalf, C. Salomon, and G. Grynberg. Method for velocimetry of cold atoms. *Phys. Rev. A*, 50:R1992, 1994.

[82] S. Guibal, C. Trich, L. Guidoni, P. Verkerk, and G. Grynberg. Recoil-induced resonances of Cesium atoms in the transient domain. *Opt. Comm.*, 131:61, 1996.

[83] M. Kozuma, Y. Imai, K. Nakagawa, and M. Ohtsu. Observation of a transient response of recoil-induced resonance: A method for the measurement of atomic motion in an optical standing wave. *Phys. Rev. A*, 52:R3421, 1995.

[84] C. F. Bharucha, K. W. Madison, P. R. Morrow, S. R. Wilkinson, B. Sundaram, and M. G. Raizen. Observation of atomic tunneling from an accelerating optical potential. *Phys. Rev. A*, 55:R857, 1997.

[85] Z. Hu and H. J. Kimble. Observation of a single atom in a magneto-optical trap. *Opt. Lett.*, 19:1888, 1994.

[86] F. Ruschewitz, D. Bettermann, J. L. Peng, and W. Ertmer. Statistical investigations on single trapped neutral atoms. *Europhys. Lett.*, 34:651, 1996.

[87] D. Haubrich, H. Scadwinkel, F. Strauch, B. Ueberholz, R. Wynands, and D. Meschede. Observation of individual neutral atoms in magnetic and magneto-optical traps. *Europhys. Lett.*, 34:663, 1996.

[88] S. Kuhr, W. Alt, D. Schrader, M. Muller, V. Gomer, and D. Meschede. Deterministic delivery of a single atom. *Science*, 293:278, 2001.

[89] N. Schlosser, G. Reymond, I. Prosenko, and P. Grangier. Sub-Poissonian loading of single atoms in a microscopic dipole trap. *Nature*, 411:1024, 2001.

[90] M. Greiner, O. Mandel, T. Esslinger, T. W. Haensch, and I. Bloch. Quantum phase transition from a superfluid to a Mott insulator in a gas of ultracold atoms. *Nature*, 415:39, 2002.

[91] D. Jaksch, C. Bruder, J. I. Cirac, C. W. Gardiner, and P. Zoller. Cold bosonic atoms in optical lattices. *Phys. Rev. Lett.*, 81:3108, 1998.

[92] R. B. Diener. *Quantum Dynamics of Trapped Ultracold Atoms.* PhD thesis, The University of Texas at Austin, 2003.

[93] A. Dudarev. Tweezer progress. This is a series of documents that can be found online at `http://chaos.ph.utexas.edu/~dudarev/tweezer`.

[94] C. Zener. Non-adiabatic crossing of energy levels. *Proc. R. Soc. London, Ser. A*, 137:696, 1932.

[95] A. Gorlitz, J. M. Vogels, A. E. Leanhardt, C. Raman, T. L. Gustavson, J. R. Abo-Shaeer, A. P. Chikkatur, S. Gupta, S. Inouye, T. Rosenband, and W. Ketterle. Realization of Bose-Einstein condensates in lower dimensions. *Phys. Rev. Lett.*, 87:130402, 2001.

[96] J. S. Townsend. *A Modern Approach to Quantum Mechanics*. University Science Books, 2000.

[97] W. Alt. An objective lens for efficient fluorescence detection of single atoms. *Optik*, 113:142, 2002.

[98] J. Mompart, K. Eckert, W. Ertmer, G. Birkl, and M. Lewenstein. Quantum computing with spatially delocalized qubits. *Phys. Rev. Lett.*, 90:147901, 2003.

[99] A. M. Dudarev, R. B. Diener, B. Wu, M. G. Raizen, and Q. Niu. Entanglement generation and multiparticle interferometry with neutral atoms. *Phys. Rev. Lett.*, 91:010402, 2003.

[100] A. Marte, T. Volz, J. Schuster, S. Drr, G. Rempe, E. G. M. van Kempen, and B. J. Verhaar. Feshbach resonances in Rubidium 87: Precision measurement and analysis. *Phys. Rev. Lett.*, 89:283202, 2002.

[101] R. Grimm, M. Weidemuller, and Y. Ovchinnikov. Optical dipole traps for neutral atoms. *Adv. At. Mol. Opt. Phys.*, 42:95, 2000.

[102] N. Friedman, A. Kaplan, and N. Davidson. Dark optical traps for cold atoms. *Adv. At. Mol. Opt. Phys.*, 48:99, 2002.

[103] J. B. Marion and S. T. Thornton. *Classical Dynamics of Particles and Systems.* Saunders College Publishing, 1995.

[104] D. J. Griffiths. *Introduction to Electrodynamics.* Prentice Hall, 1989.

[105] J. D. Jackson. *Classical Electrodynamics.* John Wiley & Sons, Inc., 1999.

[106] K. L. Corwin, S. J. M. Kuppens, D. Cho, and C. E. Wieman. Spin-polarized atoms in a circulary polarized optical dipole trap. *Phys. Rev. Lett*, 83:1311, 1999.

[107] F. Dalfovo, S. Giorgini, L. Pitaevskii, and S. Stringari. Theory of Bose-Einstein condensation in trapped gases. *Rev. Mod. Phys.*, 71:463, 1999.

[108] A. J. Leggett. Bose-Einstein condensation in the alkali gases: Some fundamental concepts. *Rev. Mod. Phys.*, 73:301, 2001.

[109] L. Pitaevskii and S. Stringari. *Bose-Einstein Condensation.* Clarendon Press, 2003.

[110] C. J. Pethick and H. Smith. *Bose-Einstein Condensation in Dilute Gases.* Cambridge University Press, 2002.

[111] L. E. Reichl. *A Modern Course in Statistical Physics*. John Wiley and Sons, Inc., 1998.

[112] D. Guery-Odelin. *Dynamique Collionnelle des Gaz d'Alcalins Lourds: du Refroidissement Evaporatif a la Condensation de Bose-Einstein*. PhD thesis, École Normale Supérieure, 1998.

[113] M. D. Lee, S. A. Morgan, M. J. Davis, and K. Burnett. Energy-dependent scattering and the Gross-Pitaevskii equation in two-dimensional Bose-Einstein condensates. *Phys. Rev. A*, 65:043617, 2002.

Vita

James Louis Hanssen was born on December 4, 1975 in the tiny hamlet of Port Arthur, Texas to Dean L. Hanssen and Norma J. Hanssen. He graduated from Port Neches-Groves High School in Port Neches, Texas in May 1994. He receive the Bachelor of Arts degree in Physics and Mathematics in 1998 from Rice University in Houston, Texas. In the fall of that year he enrolled in the graduate physics program at the University of Texas at Austin. In December of 1999 he joined the research group of Mark Raizen where he has performed experiments with ultra-cold cesium atoms and rubidium condensates.

Permanent address: 11915 Stonehollow Apt. 538
Austin, Texas 78758

This dissertation was typeset with LaTeX[†] by the author.

[†]LaTeX is a document preparation system developed by Leslie Lamport as a special version of Donald Knuth's TeX Program.